Università degli Studi di Napoli Federico II

Dottorato di Ricerca in Fisica

Ciclo XXIX

Coordinatore: Prof. Salvatore Capozziello

Beyond Standard Model searches in jets plus missing transverse energy final states with the ATLAS experiment at the LHC

Settore Scientifico Disciplinare FIS/01

Dottorando
Francesco Cirotto

Tutori
Prof.ssa Mariagrazia Alviggi
Dott. Gianpaolo Carlino
Dott. Francesco Alessandro Conventi

Anni 2014/2017

Contents

Introduction

In the current modern Physics description all particle interactions can be interpreted as expression of four fundamental interactions: electromagnetic, weak, strong and gravitational. The Standard Model of particle physics is the theoretical model which describes three of these interactions, excluding only gravitation.
The last decades of experiments have proved with a remarkable level of precision all Standard Model predictions. The most recent success is the discovery of Higgs Boson, a particle responsible to give mass to all elementary particles through the Higgs-Brout-Englert mechanism. The announcement was given in 2012, at CERN, where Higgs events were produced in proton-proton collisions at the Large Hadron Collider (LHC).
Whilst Higgs boson discovery emphasizes the robustness of Standard Model, this successful theoretical framework can not be considered as a complete theory. Aside gravitational interaction, which is not part of the model, there are several theoretical problems still unsolved. One of the main concern, the *hierarchy problem*, namely the large discrepancy between electroweak and gravity interaction, can be figured out by introducing new theoretical models opening to Beyond Standard Model (BSM) Physics. In this new physics scenarios several models predict the existence of new particles and interactions.
Supersymmetry (SUSY) is usually one of the most accepted BSM theory: a supersymmetric particle is assigned to each Standard Model elementary particle.
Models with extra dimensions are also considered for probing new physics.
Indications for new physics can be also derived from many astrophysical and cosmological observations, which indicate that the visible matter constitutes only a small fraction of the whole Universe. Dark Matter and Dark Energy are currently appealing solutions to explain these experimental evidences, providing weakly interacting massive particles (WIMPs) as possible candidates.
The theoretical models introduced lead to many possible topologies with neutral particles candidates that could be produced during LHC collisions,

leading to final states characterized from signatures with missing momentum. One way to observe them is when they are produced in association with a visible SM particle. In this context the final state with jet and missing momentum, the monojet channel, is the most promising channel, expected to achieve the most sensitive results among these dedicated searches. Although the monojet channel is the most compelling channel, a dedicated search with bottom quarks and missing momentum can give both complementary results and test new theoretical scenarios in which new particles couple to down generation quarks.

This thesis is organized as follows.

In Chapter 1, an overview of Standard Model particles and interactions is presented, together with Higgs mechanism description.

In Chapter 2, after motivating the necessity of a Standard Model extension the most valued Beyond Standard Model theories is provided, in particular SUSY, Dark Matter and extra dimensions.

The experimental LHC facilities and the main features of ATLAS detectors are described in Chapter 3, while the identification and reconstruction of the physics objects used in the analysis are detailed in Chapter 4.

Chapter 5 is dedicated to an extensive description of the analysis with bottom quarks and missing momentum, reporting selection criteria and background estimations as well as results on the models considered obtained with the full available dataset collected from 2015 collisions at the LHC.

Finally in Chapter 6 a brief overview of DM searches will be presented, with a particular emphasis to the comparison of LHC results with non-collider experiments.

Chapter 1

The Standard Model of Particle Physics

The Standard Model (SM) [1, 2, 3] is a quantum field theory who describes three of the four known fundamental interactions: strong interaction, electromagnetic interaction and weak interaction. In this chapter an overview of SM theoretical framework will be provided.

1.1 The Standard Model: a quantum field theory

Quantum field theory (QFT) is a modern physics theory who describes quantum mechanical models of particle physics. It incorporates quantum mechanics, special relativity and the concept of field.
QFT introduced the *second quantization*, a formalism in which fields are treated as field operators (as function of space-time coordinates) that create and destroy particles. These operators obey to equations of motion derived from a lagrangian L through a variational principle. Usually L is written as integral of a lagrangian density $\mathcal{L}$ simply referred as lagrangian, involving fields $\phi_j(x)$ and its derivatives $\frac{\partial \phi_j(x)}{\partial x_\mu} \equiv \partial_\mu \phi_j(x)$:

$$\mathcal{L}(t, \mathbf{x}) = \mathcal{L}\left(\phi_j(x), \partial_\mu \phi_j(x)\right). \tag{1.1}$$

The equations of motion of fields are obtained by applying Eulero-Lagrange equations

$$\frac{\partial \mathcal{L}}{\partial \phi_j} - \frac{\partial}{\partial x^\mu}\left(\frac{\partial \mathcal{L}}{\partial\left(\frac{\partial \phi_j}{\partial x_\mu}\right)}\right) = 0 \qquad (j = 1, 2, ...) \tag{1.2}$$

belonging to a variational principle. Field interactions are introduced by imposing that free lagrangian $\mathcal{L}_0$ satisfies a local gauge symmetry. In this way one obtains the interaction term $\mathcal{L}'$

$$\mathcal{L} = \mathcal{L}_0 + \mathcal{L}'.$$

To each lagrangian a set of Feynman rules is associated.

SM particles belongs to two categories [4]:

- **particles constituting matter**, that is quarks and leptons, fermions with spin 1/2 (to each one corresponds an antiparticle). These particles are classified on the basis of their interactions and divided in *generations* each containing a pair of quarks and a pair of leptons. Particles differ each other for their masses and their quantum numbers. The three generations are reported in table 1.1 for leptons and table 1.2 for quarks;
- **interaction mediator particles**, they are bosons, also know as *vector boson* o *gauge bosons* (table 1.3) since they are introduced on the basis of a symmetry principle, the *gauge symmetry*.

Generation	Lepton	Charge $[Q/e]$	Mass [MeV]
First	e	-1	0.511
	ν_e	0	$< 0.225 \times 10^{-3}$
Second	μ	-1	105.7
	ν_μ	0	< 0.19
Third	τ	-1	1777
	ν_τ	0	< 18.2

Table 1.1: The three generations of leptons with the corresponding masses.

The SM theoretical framework relies on a symmetry principle: the theory is invariant under a particular group of transformations, the gauge transformations. Gauge invariance guarantees the mathematical coherence and the theory predictivity, that is the theory renormalization. The symmetry group of SM is

$$SU(3)_C \otimes SU(2)_L \otimes U(1)_Y,$$

where:

Generation	Quark	Charge $[Q/e]$	Mass [GeV]
First	u	$+\frac{2}{3}$	$< 2.3 \times 10^{-3}$
	d	$-\frac{1}{3}$	$< 4.8 \times 10^{-3}$
Second	c	$+\frac{2}{3}$	1.28
	s	$-\frac{1}{3}$	95×10^{-3}
Third	t	$+\frac{2}{3}$	173.5
	b	$-\frac{1}{3}$	4.18

Table 1.2: The three generations of quarks with the corresponding masses.

Interaction	Boson	Charge $[Q/e]$	Mass [GeV]
Electromagnetic	γ	0	0
Weak	$W^{\pm}$	± 1	80.4
	Z	0	91.2
Strong	g	0	0

Table 1.3: Gauge bosons for the three fundamental interactions of the Standrd Model.

- $SU(3)_C$ is the non-abelian colour symmetry group, which describes strong interactions between quarks, via an octet of massless gauge bosons, the gluons, obeying to the quantum chromodynamics (QCD) rules.
- $SU(2)_L \otimes U(1)_Y$ is the weak isospin symmetry group that describes the electroweak (EW) interaction obtained from the product of $SU(2)_L$ symmetry group (weak interaction) and $U(1)_Y$ symmetry group (electromagnetic interaction) and described in the Glashow, Weinberg and Salam model. Electroweak interaction is mediated via four gauge bosons, three of them massive ($W^{\pm}$, Z) and one massless, the photon (γ).

The Standard Model lagrangian can be divided into two parts: QCD term, describing strong interactions, and EW term, describing electromagnetic and weak interactions:

$$\mathcal{L}_{SM} = \mathcal{L}_{QCD} + \mathcal{L}_{EW}.$$

1.2 Symmetries and conservation laws

Symmetries and conservation laws play an important role in the exploration and comprehension of physical phenomena. A *symmetry* of a physical system

is a transformation under which the system remains unchanged. In that case the theory is said to be invariant under the transformation. Symmetries can be classified as *global* or *local*.
The former refers to a feature common to the most of the gauge theories, which describe lagrangians that are globally invariant under a coordinate transformation. Requiring a global invariance leads to a conserved physical property of the sistem.

In local transformations, one obtains a different value for each space-time point. A gauge invariance request leads *naturally* to the introduction of new fields which act as force carriers. It can be proved that local gauge invariance holds for a theory of interacting fields. For the development of gauge theories their request applied to a free lagrangian introduces interactions.

In the Standard Model case, strong interaction are symmetric under $SU(3)_C$ gauge group, and the symmetry is said to be *exact*. The symmetry describing weak interactions are not exact (in that case one refers as *symmetry breaking*), thus leading to massive mediator particles. The mechanism of symmetry breaking, which gives mass to particles and introduces a new scalar particles, the Higgs boson, will be described in paragraph 1.6.

1.3 Quantum electrodynamics

Quantum electrodynamics (QED) is the quantum theory describing electromagnetic interactions between charged particles, including in its framework special relativity. Mathematically QED is an abelian gauge theory, with the symmetry group being $U(1)$. The lagrangian for a spin 1/2 field with mass m is:

$$\mathcal{L} = i\bar{\psi}\gamma^\mu\partial_\mu\psi - m\bar{\psi}\psi, \tag{1.3}$$

where:

$$\bar{\psi} = \psi^\dagger\psi^0,$$

and γ^μ are Dirac matrices 4×4, satisfying anticommutation relation $\{\gamma^\mu, \gamma^\nu\} = \gamma^\mu\gamma^\nu + \gamma^\nu\gamma^\mu = 2g^{\mu\nu}$, with $g^{\mu\nu}$ being the metric tensor. The request of local gauge invariance leads to the following transformation for the fields:

$$\begin{aligned} \psi &\rightarrow \psi' = e^{iq\theta(x)}\psi(x) \\ \bar{\psi} &\rightarrow \bar{\psi}' = e^{-iq\theta(x)}\bar{\psi}'(x) \end{aligned} \tag{1.4}$$

and, by introducing the *covariant derivative*

$$\mathcal{D}_\mu \equiv \partial_\mu + iqA_\mu(x) \tag{1.5}$$

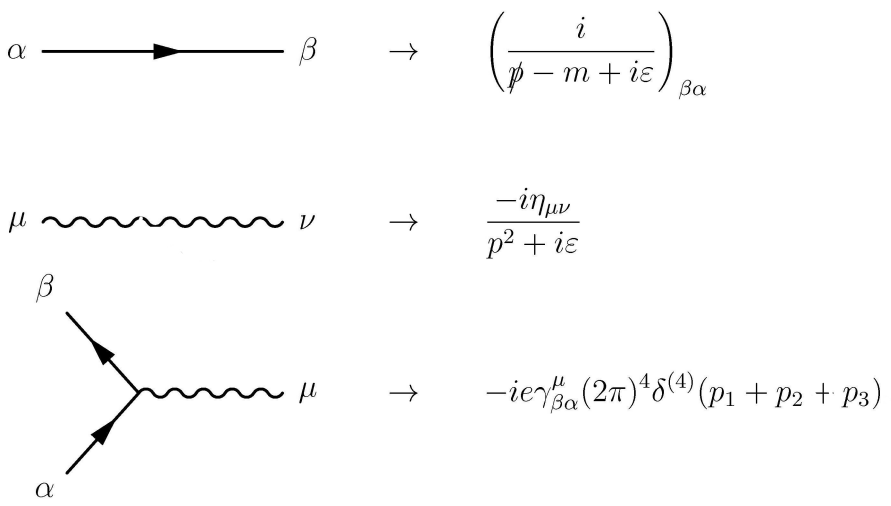

Figure 1.1: QED Feynman rules.

the vectorial field $A_\mu(x)$ becomes:

$$A_\mu(x) \to A_\mu(x) - \partial_\mu\theta(x). \tag{1.6}$$

The Lagrangian

$$\mathcal{L} = i\bar{\psi}\gamma^\mu\mathcal{D}_\mu\psi - m\bar{\psi}\psi \tag{1.7}$$

is now invariant under local gauge transformation. It should be noted that local gauge invariance request naturally leads the theory to introduce a gauge field A_μ which is associated to the photon. The complete QED lagrangian includes the kinetic term describing free photons propagation and that is invariant under local gauge transformation:

$$\begin{aligned}\mathcal{L} &= i\bar{\psi}\gamma^\mu\mathcal{D}_\mu\psi - m\bar{\psi}\psi - \frac{1}{4}F^{\mu\nu}F_{\mu\nu} \\ &= i\bar{\psi}\gamma^\mu\partial_\mu\psi - m\bar{\psi}\psi - j^\mu A_\mu - \frac{1}{4}F^{\mu\nu}F_{\mu\nu},\end{aligned} \tag{1.8}$$

where $j^\mu A_\mu$ corresponds to the interaction term between Dirac particle and electromagnetic filed. The Feynman rules obtained from such description of QED are shown in figure 1.1.

1.4 Quantum chromodynamics

Quantum chromodynamics (QCD) is the theory for strong interactions between quarks and gluons constituting hadrons. Similarly to QED, it relies

on a gauge invariance principle, in this case a non abelian colour $SU(3)_C$ group. The non-abelian property allows to auto-interacting terms in QCD lagrangian, that carry a charge (*colour charge*). In QCD description quarks are represented as colour triplets, for each flavour f correspond three spinors fields $\psi_j^f(x)$ with colour index $j = 1, 2, 3$. QCD free lagrangian is:

$$\mathcal{L} = \sum_j \bar{\psi}_j (i\gamma^\mu \partial_\mu - m_j)\psi_j. \tag{1.9}$$

The request of invariance under local gauge transformation for the $SU(3)_C$ group leads to

$$\psi_j^f \;\rightarrow\; \psi_j^{'f} = e^{ig_s \vec{\lambda}\cdot\vec{\theta}(x)}\psi_j^f(x), \tag{1.10}$$

where λ_i are the 8 Gell-Mann matrices and $g_s = (4\pi\alpha_s)^{\frac{1}{2}}$ is the strong coupling constant. The invariant lagrangian is obtained by introducing gluon fields (8) and defining the covariant derivative as

$$\mathcal{D}_\mu = \partial_\mu + ig\frac{\lambda_a}{2}G_\mu^a \tag{1.11}$$

the lagrangian 1.9 is hence invariant for local gauge transformations. The kinetic term for each gluon is $-\frac{1}{4}G^a_{\mu\nu}G_a^{\mu\nu}$, where $G^a_{\mu\nu} = \partial_\mu A^a_\nu - \partial_\nu A^a_\mu - g_s f_{abc} A^b_\mu A^c_\nu$ the complete QCD lagrangian is:

$$\mathcal{L} = \sum_f \bar{\psi}_{f,a}(i\gamma^\mu\partial_\mu - m)\psi_{f,a} - g_s\bar{\psi}_{f,a}\gamma^\mu G^a_\mu(x)\frac{\lambda_a}{2}\psi_{f,a} - \frac{1}{4}G^a_{\mu\nu}(x)G_a^{\mu\nu}(x) \tag{1.12}$$

with $f = 1, 2, 3$ and $a = 1, 2, ...8$. The terms in the lagrangian 1.12 result in gluon auto-interactions, thus allowing new vertexes not present in QED (as shown in figure 1.2). The main consequences are asymptotic freedom and colour confinement.

1.5 Electroweak interaction

The theory of unification of electromagnetic and weak interactions has been developed in the 60s by Sheldon Glashow, Abdus Salam e Steven Weinberg, who were awarded with the Physics Nobel Prize in 1979. Mathematically it is described by $SU(2)_L \otimes U(1)_Y$ symmetry group, where L refers to left-handed fields and Y to weak hypercharge.
Electroweak interaction holds for all Standard Model fermions. A fermion spinor field can be described in terms of its left-handed and right-handed components by using a projection operator:

$$\psi_{L,R} = \frac{1}{2}\left(1 \mp \gamma^5\right)\psi$$

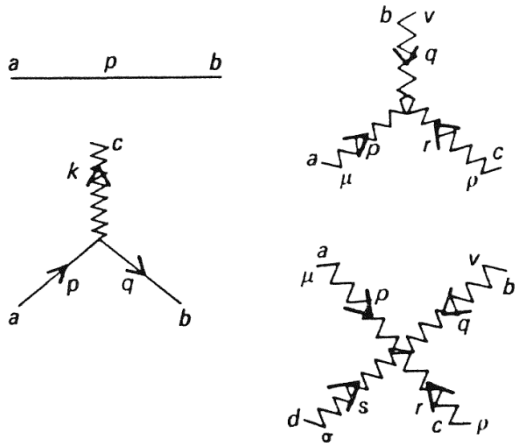

Figure 1.2: QCD vertices.

Experimental evidences show that weak interaction violates parity symmetry. In particular weak interaction affects only left-handed component of fermions for charged current processes, described as doublets of the isospin weak symmetry. In neutral current processes also the right-handed component is involved, described as singlet.

A conserved charge is associated to $U(1)_Y$ group, the weak hypercharge. The hypercharge Y and the weak isospin I satisfy Gell-Mann-Nishima relation, which relates them to the electric charge, according the formula:

$$Q = I_3 + \frac{Y}{2},$$

I_3 is the the third component of weak isospin. Table 1.4 reports quantum numbers for each fermion. Gauge invariance under $SU(2)_L \otimes U(1)_Y$ group leads to:

$$\begin{aligned} \psi_L &\rightarrow \psi'_L = e^{i\alpha^a(x)\cdot T_a + i\beta(x)Y}\psi_L \\ \psi_R &\rightarrow \psi'_R = e^{i\beta(x)Y}\psi_R \end{aligned} \tag{1.13}$$

where $\alpha^a(x)$ e $\beta(x)$ are local phases T_a and Y are respectively $SU(2)_L$ and $U(1)$ group generators. The gauge invariance is preserved after the introduction of four fields, and defining covariant derivative as:

$$\mathcal{D}_\mu = \partial_\mu + i\frac{g}{2}W^a_\mu T_a + i\frac{g'}{2}B_\mu Y \tag{1.14}$$

with g an g' coupling constants of the two interactions. The final lagrangian,

	Generations			Quantum numbers			
	1	2	3	I	I_3	Y	Q[e]
Leptons	$\begin{pmatrix}\nu_e\\e^-\end{pmatrix}_L$	$\begin{pmatrix}\nu_\mu\\\mu^-\end{pmatrix}_L$	$\begin{pmatrix}\nu_\tau\\\tau^-\end{pmatrix}_L$	1/2 1/2	1/2 −1/2	−1 −1	0 −1
	e_R^-	μ_R^-	τ_R^-	0	0	-2	-1
Quarks	$\begin{pmatrix}u\\d\end{pmatrix}_L$	$\begin{pmatrix}c\\s\end{pmatrix}_L$	$\begin{pmatrix}t\\b\end{pmatrix}_L$	1/2 1/2	1/2 −1/2	1/3 1/3	2/3 −1/3
	u_R	c_R	t_R	0	0	4/3	2/3
	d_R	s_R	b_R	0	0	-2/3	1/3

Table 1.4: Overview on fermion quantum numbers in the Stanrd Model. Right-handed netrinos do not interact and are not considered.

invariant for $SU(2)_L \otimes U(1)_Y$ is then:

$$\mathcal{L}_\mu = \sum_j i\bar{\psi}_L^j \gamma^\mu \mathcal{D}_\mu \psi_L^j + \sum_k i\bar{\psi}_R^k \gamma^\mu \mathcal{D}_\mu \psi_R^k - \frac{1}{4} W_{\mu\nu}^a W_a^{\mu\nu} - \frac{1}{4} B_{\mu\nu} B^{\mu\nu} \quad (1.15)$$

where indices i and k sum over singlets and doublets reported in table 1.4 and

$$W_{\mu\nu}^a = \partial_\mu W_\nu^a - \partial_\nu W_\mu^a - g' \epsilon_{abc} W_\mu^b W_\nu^c \quad (1.16)$$

$$B_{\mu\nu} = \partial_\mu B_\nu - \partial_\nu B_\mu. \quad (1.17)$$

1.6 Spontaneous symmetry breaking

Although both electroweak and QCD interactions are based on gauge principles, their lagrangians don't include mass terms, in contradiction with what experimental evidences suggest. The mass terms to be added must not violate gauge invariance. The *Higgs mechanism* [5, 6, 7] has been introduced to solve this problem. The masses of the particles are obtained through a *spontaneous symmetry breaking* mechanism: an initial symmetrical state turns out in an asymmetrical state. The idea preserves the gauge invariance of the lagrangian, but not its fundamental state. The symmetry breaking of the ground state is due to a scalar field, the *Higgs field*.
The Higgs field ϕ consists of a weak isospin doublet of complex scalar fields with hypercharge $Y = 1$:

$$\phi = \begin{pmatrix} \phi^+ \\ \phi^0 \end{pmatrix} = \frac{1}{\sqrt{2}} \begin{pmatrix} \phi_1 + i\phi_2 \\ \phi_3 + i\phi_4 \end{pmatrix} \tag{1.18}$$

The lagrangian of the Higgs sector contains the following potential terms,

$$V(\phi) = \mu^2 \phi^\dagger \phi + \lambda(\phi^\dagger \phi)^2 = \mu^2 \phi^2 + \lambda \phi^4, \tag{1.19}$$

thus resulting in:

$$\mathcal{L}_H = (\mathcal{D}_\mu \phi)^\dagger (\mathcal{D}^\mu \phi) - V(\phi) \tag{1.20}$$

where $\mathcal{D}_\mu$ has been defined in equation 1.14.
The choice of $\lambda > 0$, necessary for the vacuum stability, and $\mu^2 < 0$, leads to the potential shown in Figure 1.3. The potential has an infinite number of minimum energy states satisfying the condition:

$$\phi_0^2 = -\frac{\mu^2}{2\lambda} \equiv v^2 \tag{1.21}$$

where v is set to 246 GeV. The symmetry invariance is ensured by the following solution:

$$\phi_1 = \phi_2 = \phi_4 = 0, \qquad \phi_3^2 = -\frac{\mu^2}{2\lambda} = v^2. \tag{1.22}$$

A perturbative expansion around the vacuum state of ϕ

$$\phi_0 = \begin{pmatrix} 0 \\ v \end{pmatrix} \tag{1.23}$$

as:

$$\phi = \begin{pmatrix} 0 \\ \frac{1}{\sqrt{2}}(v + H(x)) \end{pmatrix} \tag{1.24}$$

leads to the symmetry breaking, and the mass terms are obtained by substituting ϕ value in the lagrangian.

Gauge boson masses

After the request of global gauge invariance one obtains the following lagrangian:

$$\mathcal{L} = (\mathcal{D}_\mu \phi)^\dagger (\mathcal{D}^\mu \phi) - V(\phi) - \frac{1}{4} W^a_{\mu\nu} W_a^{\mu\nu} - \frac{1}{4} B_{\mu\nu} B^{\mu\nu}. \tag{1.25}$$

From the kinetic term (which includes quadratics terms) the physical fields $W^\pm$ are defined as:

$$W_\mu^\pm = \frac{1}{\sqrt{2}}(W_\mu^1 \mp \mathrm{i} W_\mu^2) \tag{1.26}$$

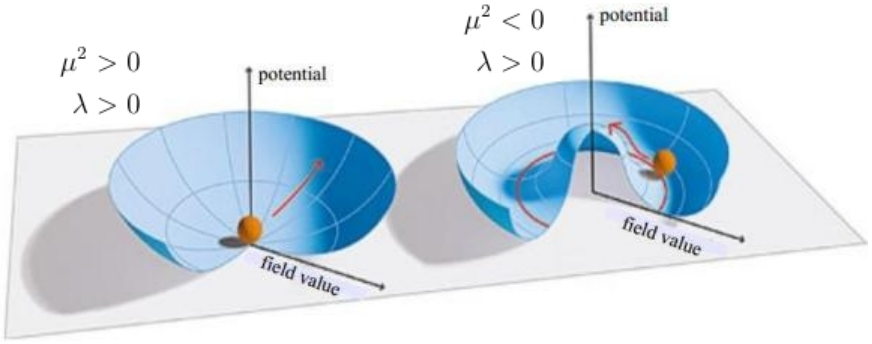

Figure 1.3: Higgs potential $V(\phi)$. Non-trivial case stands for $\lambda > 0$ and $\mu^2 < 0$.

while Z field and photon fields are orthogonal:

$$Z_\mu = \frac{g' W_\mu^3 - g B_\mu}{\sqrt{g'^2 + g^2}} \tag{1.27}$$

$$A_\mu = \frac{g' W_\mu^3 + g B_\mu}{\sqrt{g'^2 + g^2}}. \tag{1.28}$$

By introducing the mixing angle θ_w

$$\cos\theta_\mathrm{w} = \frac{g'}{\sqrt{g'^2 + g^2}}, \ \sin\theta_\mathrm{w} = \frac{g}{\sqrt{g'^2 + g^2}} \tag{1.29}$$

Z and A fields become:

$$Z_\mu = -B_\mu \sin\theta_\mathrm{w} + W_\mu^3 \cos\theta_\mathrm{W} \tag{1.30}$$

$$A_\mu = B_\mu \cos\theta_\mathrm{w} + W_\mu^3 \sin\theta_\mathrm{W}. \tag{1.31}$$

The masses of the bosons are represented by the coefficients of quadratic terms from the lagrangian 1.25:

$$M_W = \frac{gv}{2} \tag{1.32}$$

$$M_Z = \frac{v}{2}\sqrt{g'^2 + g^2} \tag{1.33}$$

while photon is massless. The relation between boson masses and mixing angle is:

$$\frac{M_W}{M_Z} = \cos\theta_\mathrm{W}. \tag{1.34}$$

Fermion masses

Fermion mass terms can be added by considering the interaction between scalar field ϕ and fermions. The Yukawa terms of the lagrangian are:

$$\mathcal{L}_{\text{Yukawa}} = -G_\ell^{ij}\bar{L}_L^i\phi\ell_R^j - G_d^{ij}\bar{Q}_L^i\phi d_R^j - G_u^{ij}\bar{Q}_L^i\phi_C u_R^j + \text{h.c.} \tag{1.35}$$

where $\bar{L}_L^i$ an $\bar{Q}_L^i$ are isospin doublets for leptons and quarks, and ℓ_R^j, d_R^j, u_R^j are singlets for letpons and up and down quark states. In the last term $\phi_C = i\sigma_2\phi^*$. The matrices G_ℓ^{ij}, G_d^{ij} e G_u^{ij} define the coupling constants and the quark generation mixing, whose weak interaction eigenstates are linear combination of mass eigenstates. Fermion masses are obtained by applying spontaneous symmetry breaking and substituting ϕ value as in equation 1.24. As example, electron mass term is reported:

$$\begin{aligned}\mathcal{L}_e &= -\frac{G_e}{\sqrt{2}}v\left(\bar{e}_L e_R + \bar{e}_R e_L\right) - \frac{G_e}{\sqrt{2}}\left(\bar{e}_L e_R + \bar{e}_R e_L\right)H \\ &= -m_e\bar{e}e - \frac{m_e}{v}\bar{e}eH,\end{aligned} \tag{1.36}$$

where $m_e = \frac{G_e v}{\sqrt{2}}$ is the electron mass. The coupling constant G_e is arbitrary and electron mass is not predicted. The lagrangian contains an interaction terms that couples Higgs field to the electron, proportional to electron mass. The procedure is the same for remaining fermion masses, with the exception of neutrinos that are considered massless.
In particular for quarks, the non-diagonal couplings corresponding to non-diagonal terms in Yukawa matrices persist after symmetry breaking and are solved through four unitary transformations allowing transition from interaction eigenstates to mass eigenstates. These transformations affect currents: in charge current interactions charge and parity symmetry is violated.

Chapter 2

Beyond Standard Model theories

The discovery of Higgs Boson, announced in July 2012 [8, 9], completes the SM puzzle of particles. Nevertheless Standard Model is not a finite theory: several problems still don't have an explanation. It is used to refer as Physics *Beyond Standard Model* (BSM) to a class of theories which aim to fill this gap. In this chapter a brief description of the limits of the Standard Model will be given, and some of the most promising BSM theories will be introduced.

2.1 Limits of the Standard Model

Despite its numerous successes SM is not a complete theory. The Standard Model theory shows its incompleteness in several aspects:

- **Mass**, it contains 19 free parameters, the masses of the particles and the coupling constants. Neutrino masses are set to zero in the model.
- **Unification**, the theory does not include gravitation, and a Great Unification Theory (GUT) of strong and electroweak interactions has not been successfully developed yet.
- **Flavour**, the existence of three quark and lepton generations with consistent mass differences.
- **Cosmology**, SM does not provide an explanation of matter/antimatter asymmetry and Dark Matter/Energy contributions.

One of the most discussed theoretical controversy is the *hierarchy problem*, namely the huge discrepancy between weak and gravity interaction. Two

mass scales are known in nature: the first corresponds to the electroweak symmetry breaking at $m_W \sim 100\text{GeV}$ and the second is related to gravitational interaction, Planck mass $m_P \sim 10^{19}$ GeV. The Higgs mass correction in a fermionic loop can be written as:

$$(\delta m_H^2)_f \simeq -\frac{\lambda_f^2}{16\pi^2}\left[-2\Lambda^2 - 6m_f^2 \ln\frac{\Lambda}{m_f} + \cdots\right], \tag{2.1}$$

that shows a quadratic divergence depending on the *cut-off scale* Λ. λ_f and m_f are respectively the Yukawa couplings and the masses of the fermions. If $\Lambda = m_P$, Higgs mass correction becomes several order of magnitudes greater than the SM expectations. To avoid this issue a large cancellation, *fine tuning* would be needed.

2.2 Supersymmetry

A solution to the hierarchy problem has been developed in Supersymmetric (SUSY) theories [10, 11]. The Higgs mass correction in a scalar loop is:

$$(\delta m_H^2)_S \simeq -\frac{g_S}{16\pi^2}\left[2\Lambda^2 - 2m_S^2 \ln\frac{\Lambda}{m_S} + \cdots\right] \tag{2.2}$$

where g_S is the coupling between the Higgs and the scalar with mass m_S. The opposite sign with respect to equation 2.1 depends on the Fermi statistics. It is now evident that quadratic divergence would be cancelled if the two contributions in equations 2.1 and 2.2 have summed up by imposing:

$$\lambda_f^2 = g_S. \tag{2.3}$$

This cancellation would be mass and coupling independent. Hence, a way to eliminate divergences is:

- associate to each SM particle a new particle which is a boson if the SM one is a fermion and vice versa,
- require a symmetry that ensures this cancellation to all perturbativity orders.

These conditions are satisfied in Supersymmetry. A supersymmetric transformation turns out a bosonic state into a fermionic one and vice versa, therefore to each fermion corresponds a boson with identical quantum numbers but with spin differing of 1/2. If SUSY was an exact symmetry each supersymmetric

partner (*sparticle*) should have the same mass of the corresponding SM particle. Since there is no evidence, SUSY could be a broken symmetry. In order to avoid the hierarchy problem and the quadratic divergences a *soft* symmetry breaking must be required, thus leading to the following Lagrangian:

$$\mathcal{L} = \mathcal{L}_{SUSY} + \mathcal{L}_{soft}, \tag{2.4}$$

where $\mathcal{L}_{SUSY}$ preserves symmetry invariance and $\mathcal{L}_{soft}$ is responsible to give higher masses to sparticles, that should be comparable to Higgs mass. Indeed in order to have a small fine tuning the Higgs mass correction resulting from 2.1 and 2.2

$$\delta m_H^2 = \frac{\lambda_f^2}{16\pi^2}|m_S^2 - m_f^2| \tag{2.5}$$

should give:

$$|m_S^2 - m_f^2| \lesssim 1 \text{ TeV}^2. \tag{2.6}$$

Minimal Supersymmetric Standard Model

Minimal Supersymmetric Standard Model is the simplest supersymmetric extension to SM. In this model lepton and quark supersymmetric partners are respectively *sleptons* ($\tilde{l}$) and *squarks* ($\tilde{q}$). The same procedure is applied to gauge bosons thus giving *winos* ($\tilde{W}$), *bino* ($\tilde{B}$) (which provides *zinos* ($\tilde{Z}^0$) and *photinos* ($\tilde{\gamma}$)) and *gluinos* ($\tilde{g}$). For gauge anomaly reasons two Higgs scalar doublets are introduced, leading to five Higgs physics states, and the corresponding supersymmetryc *higgsinos*. All the supermultiplets are listed in Table 2.1. Winos, higgsinos and bino mix with each other resulting in four electrically neutral *neutralinos* and two electrically charged *charginos*.
The most general supersymmetric lagrangian contains terms that violate baryon and lepton number, thus resulting in contrast with experimental evidences. In the MSSM a new symmetry is introduced, the *R-parity* which confers to a spin s particle (standard or supersymmetrycal) the quantum number

$$R = (-1)^{3(B-L)+2s}, \tag{2.7}$$

which is assumed to be conserved in physical processes. R is $+1$ for particles and -1 for sparticles. If R is a conserved quantity each vertex contains an even number of sparticles. As consequence:

- SUSY particles can be only produced in pairs from SM particles.
- The Lightest Supersymmetryc Particle (LSP) must be stable. If it is neutral, it weakly interacts with ordinary matter and constitutes a good candidate for Dark Matter.

SM		MSSM			
		Gauge eigenstates		Mass eigenstates	
Particle	Name	Particle	Name	Particle	Name
$q = u, d, c, s, t, b$	quark	$\tilde{q}_L, \tilde{q}_R$	squark	$\tilde{q}_1, \tilde{q}_2$	squark
$l = e, \mu, \tau$	lepton	$\tilde{l}_L, \tilde{l}_R$	slepton	$\tilde{l}_1, \tilde{l}_2$	slepton
$l = \nu_e, \nu_\mu, \nu_\tau$	lepton	$\tilde{\nu}$	sneutrino	$\tilde{\nu}$	sneutrino
$W^\pm$	W boson	$\tilde{W}^\pm$	wino		
W^3	W^3 field	$\tilde{W}^3$	wino		
B	B field	$\tilde{B}$	bino		
$H^{-(+)}$	Higgs boson	$\tilde{H}^{-(+)}_{1(2)}$	higgsino		
$H^0_{1,2}$	Higgs boson	$\tilde{H}^0_{1,2}$	higgsino		
H^0_3	Higgs boson				
		$\tilde{W}^\pm$, $\tilde{H}^-_1$, $\tilde{H}^+_2$		$\tilde{\chi}^\pm_{1,2}$	chargino
		$\tilde{W}^3$, $\tilde{H}^0_1$,$\tilde{H}^0_2$, $\tilde{B}$		$\tilde{\chi}^0_{1,2,3,4}$	neutralino

Table 2.1: Standard Model fields and corresponding superpartners in the MSSM.

- Each sparticle different from LSP can eventually decay in a state containing an odd number of LSPs.

Compressed Scenarios

MSSM is a model with a huge number of parameters (∼100). It it possible to build simplified models which provides a scenario where the mass difference between LSP and next-to-lightest particle (NLSP) is small. These *compressed* models predict a single decay chain with neutralino as LSP. Interesting compressed scenarios are:

- Stop pair production with $\tilde{t} \to c + \tilde{\chi}_0$;
- Sbottom pair production with $\tilde{b} \to b + \tilde{\chi}_0$;
- Squark pair production with $\tilde{q} \to q + \tilde{\chi}_0$.

The corresponding diagrams are shown in Figure 2.1. Since the mass difference between neutralino and decaying sparticle is small the final state is characterized by low missing transverse momentum thus resulting in a difficult separation between signal and multi-jet background. To avoid this issue, the studies presented require in the signal selection the presence of initial state radiation (ISR).

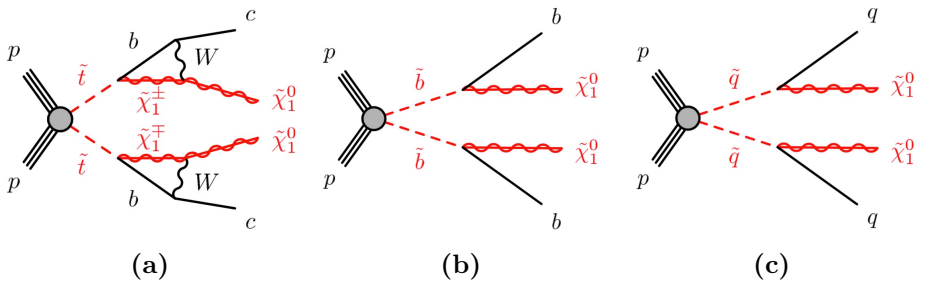

Figure 2.1: Feynman diagrams for SUSY compressed scenarios for stop (a), sbottom (b) and squark (c) decays.

2.3 Extra Spatial Dimension

In 1998 Arkani-Ahmed, Dimopolous and Dvali proposed a theory (ADD) based on extra-dimensions in order to solve the hierarchy problem [12]. In their model the large disparity between weak and Planck scale is united at weak scale. In this alternative framework they postulated the existence of n extra-dimensions (*bulk*) that could lead to potentially measurable effects on the TeV scale. While SM fields are confined in the four-dimensional space, gravity could propagate in these compactified extra dimensions. If we assume that the only fundamental scale in nature is the weak scale, extra spatial dimension of radius $\sim R$ are then introduced to relate Planck scale to the weak one. The gravitational potential of two masses m_1 and m_2 at a distance $r \ll R$ in $(4+n)$ dimension can be written as:

$$V(r) \sim \frac{m_1 m_2}{M_{Pl(4+n)}^{n+2}} \frac{1}{r^{n+1}}, \tag{2.8}$$

where $M_{Pl(4+n)}$ is the gravity scale in the $(4+n)$ dimensions. If the masses are placed at a distance $r \gg R$ one obtains the Newton's classical potential:

$$V(r) \sim \frac{m_1 m_2}{M_{Pl(4+n)}^{n+2} R^n} \frac{1}{r}, \tag{2.9}$$

giving the following relation for M_{Pl}:

$$M_{Pl}^2 \sim M_{Pl(4+n)}^{2+n} R^n. \tag{2.10}$$

Constraining it to the weak scale m_{EW} the expression for the radius becomes:

$$R \sim 10^{\frac{30}{n}-17} cm \times \left(\frac{1TeV}{m_{EW}}\right)^{1+\frac{2}{n}}. \tag{2.11}$$

The $n = 1$ case, resulting in $R \sim 10^{13}$ cm, would imply deviations of classical gravitation over solar system distances, hence is excluded by experimental cosmological evidences. The $n > 1$ cases result in small distances that can not be probed by experiment. In particular, the case where $n = 2$ yields $R \sim 100\mu\text{m} - 1\text{mm}$ is very interesting since LHC has the sensitivity to study it.
Only graviton field can propagate in the bulk. It's a spin-2 particle which mediates gravitational interaction and its projection into the four-dimensional space are massive graviton states called *Kaluza-Klein towers*. At LHC gravitons may escape detection and can be produced in association with an energetic jet. In Figure 2.2 are shown Feynamn diagrams at LO for graviton production in association with a quark or gluon.

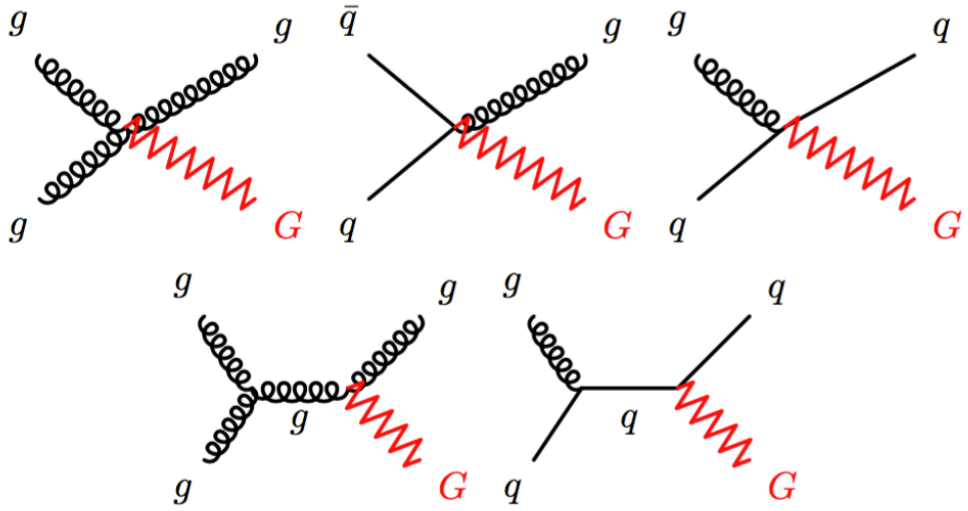

Figure 2.2: LO Feynman diagrams for graviton production with a quark or a gluon.

2.4 Dark Matter

Dark Matter (DM) existence in the Universe is highly motivated by many astrophysical and cosmological observations [13]. Neverthless, its nature and

properties are still unknown as well as no direct observations were reported. The ΛCDM (Cold Dark Matter) model, the standard model of cosmology, is based on:

- Einstein's general relativity equations, which connect the geometry of the Universe with its matter and energy content,
- a metrics describing the space-time geometry,
- equation of state for studying properties of the evolving system.

The request of homogeneity and isotropy of our Universe turns into a particular metrics expression which is applied to Einstein's field equation. A density parameter is introduced in order to evaluate the geometry of the Universe which results to be flat for the *critical density*

$$\rho_c = \frac{3H^2}{8\pi G_N}, \tag{2.12}$$

where G_N is the Newton constant,H is the *Hubble parameter* whose recent estimation yields $H_0 = 67.8 \pm 0.9\text{km s}^{-1}\text{Mpc}^{-1}$ [14]. A standard convention is to use the total density of the Universe Ω which is the ratio of the sum of all densities ρ_i over the critical one. According to this definition the Universe can be *flat* ($\Omega = 1$), *open* ($\Omega < 1$) or *closed*($\Omega > 1$). Most accurate observation [15] estimated baryons and Dark Matter densities to be:

$$\Omega_b h^2 = 0.02226 \pm 0.00023, \qquad \Omega_{DM} h^2 = 0.1186 \pm 0.0020. \tag{2.13}$$

Since ΛCDM model assumes flat Universe an additional contribution is needed to satisfy this condition, leading to the presence of Dark Energy. The corresponding densities for baryonic matter, Dark Matter and Dark Energy are respectively 5%, 26% and 69% revealing that a very small part of the Universe is known.

2.4.1 Experimental evidences

One of the most powerful evidence of DM presence in the Universe comes from the observations of the rotation curves of galaxies, reporting the velocities of stars and gases as function of their distance from the galactic center. The observed curves are in disagreement with Newtonian dynamics, from which orbital velocity can be written as:

$$v = \sqrt{\frac{G_N M(r)}{r}}, \tag{2.14}$$

with

$$M(r) \equiv 4\pi \int \rho(r) r^2 dr \tag{2.15}$$

where $\rho(r)$ is the visible matter density. It is expected that $v \propto 1/\sqrt{r}$, but observations shown a constant behaviour of $v(r)$ which implies the existence of an halo with $M(r) \propto r$ and $\rho \propto r^2$ (Figure 2.3).

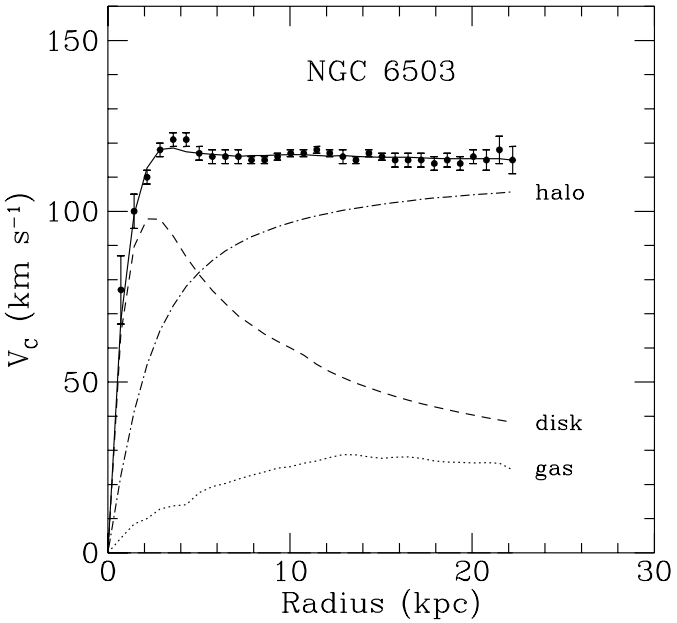

Figure 2.3: Rotation curve of galaxy NGC 6503. The dotted, dashed and dash-dotted lines are respectively the contributions of gas, disk and dark matter [16].

Dark Matter contribution can be estimated through the observation of the gravitational lensing. According to Einstein's theory of general relativity a massive body can deform the space-time curvature leading to different effects to a luminous source: deflection, luminous intensity amplification, doubling. The amount of matter present in a region can be inferred from the study of these phenomena. Observations proved that ordinary matter can not be solely responsible of such effects. See [17] for reviews.

2.4.2 Candidates

A wide class of particles, belonging to SM and to BSM models, has been introduced in order to find adequate DM candidates. Cosmological and astrophysical observations suggest that DM candidates must satisfy several requirements:

- they must be stable or having a long life on cosmological time scale,
- they must interact weakly with electromagnetic radiation,
- their abundance must fulfill the observed relic density.

SM candidates

Neutrinos have been for long considered as DM candidates, since they satisfy all the requests described above. However they are ruled out since they are relativistic particles and observations measured a neutrino density $\Omega_\nu h^2 = 0.0062$ at 95% C.L. [4], which show that neutrinos are not abundant enough to be considered as dominant component of DM.

Sterile neutrinos

These particles have similar characteristics as SM neutrinos, but they interact only gravitationally. In the model proposed by Dodelson and Widrow [18] in 1993, sterile neutrinos are right-handed and couple to left-handed neutrinos thus leading to a production mechanism via neutrino oscillations. Some models provides sterile neutrinos as cold DM, if there is a small lepton asymmetry.

Axions

Axions have been introduced in order to solve the strong CP problem of QCD, that is the fact that although QCD lagrangian has CP-violating terms no evidence has been yet observed. Experimental evidence suggests that axions are very light particles (with a mass $\lesssim 0.01$ eV [13]), which could exist in sufficient numbers to act as cold DM but they weren't in thermal equilibrium in the early Universe. Axion supersymmtric partner, the axino could explain hot DM.

Weakly interacting massive particles

Weakly interacting massive particles (WIMPs) are presented in many theoretical models as the most adequate DM candidates, with masses spacing

from GeV to TeV and weak cross sections.
In SUSY models WIMPs are identified with the LSP, namely neutralinos or gravitinos according to the model. In large extra-dimensions theories Kaluza-Klein towers are possible DM candidates.

2.4.3 WIMP searches: direct and indirect detection

Three typologies of experiments can be used for WIMP searches (a scheme of the approaches is shown in Figure 2.4):

- Direct detection experiments looking for scattering processes between DM and ordinary matter,
- Indirect detection experiments that search for the annihilation products originating from WIMP collisions,
- Collider searches with WIMP production through SM collisions.

In this section direct and indirect searches will be described, while collider searches at LHC will be illustrated in section 2.4.4.

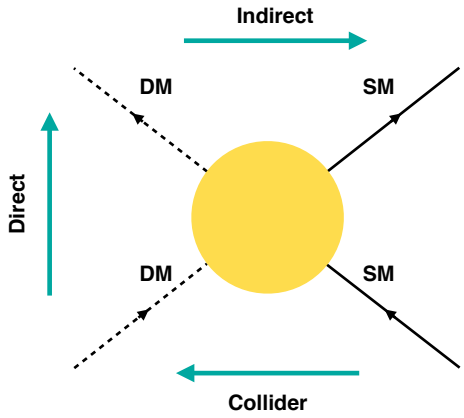

Figure 2.4: Scheme of the possible approaches for DM detection.

Direct detection

If DM fills the Universe, then it should be travelling around the earth and subsequently interacts with ordinary matter. This is the idea of direct

detection experiments: identifying nuclear recoils produced by the collisions between WIMPs and detector's target nuclei. The expected recoil energies for DM masses in the range 10 GeV to 10 TeV are typically 1 to 100 keV. To identify such low-energy and rare interactions a very efficient background suppression strategy must be adopted. Typically these experiments use large volumes of active material in order to collect a significant number of interesting events and are placed deep underground in order to suppress cosmic radiation and strong interactions. The rate of events expected in direct detection experiments can be written as [13]:

$$R \approx \sum_i N_i n_\chi \langle \sigma_{i\chi} \rangle, \tag{2.16}$$

where the index i refers to nuclei species composing the active material in the detector. The number of target nuclei in the detector is the ratio between detector mass M_{det} and the atomic mass of nuclei m_A:

$$N_i = \frac{M_{det}}{m_A}. \tag{2.17}$$

n_χ is the local WIMP density depending on WIMP energy and mass, and $\sigma_{i\chi}$ the WIMPs-nuclei scattering cross section:

$$n_\chi \equiv \frac{E_\chi}{m_\chi}. \tag{2.18}$$

The type of scattering processes are classified by their spin dependency:

- Spin dependent (SD) interactions with pseudo-scalar or axial-vector coupling. In this case cross sections are proportional to $J(J+1)$ rather than the number of nucleon: there's no advantage to use heavy nuclei.
- Spin independent (SI) interactions have scalar or vector coupling, and cross sections strongly depend on the mass of the target nuclei.

A lots of experimental efforts have been done in the last decades to detect DM signals. In these experiments nuclear recoils have been measured with different techniques: scintillation, ionization, photon, which give the great advantage to vary the systematic errors according to the experiment.
In Figure 2.5 and 2.6 are shown the limits obtained for WIMP scattering cross sections normalized to scattering on a single nucleon, for spin independent and spin dependent case, as functions of WIMP mass. It should be pointed out that sensitivity for these searches is strongly dependent on the WIMP mass: at low WIMP mass the sensitivity drops because of the not detectable recoil energy; the sensitivity is also low at high WIMP mass since the WIMP flux decreases as $\propto 1/m_\chi$. The best sensitivity is reached when WIMP mass is comparable to the mass of recoiling nuclei.

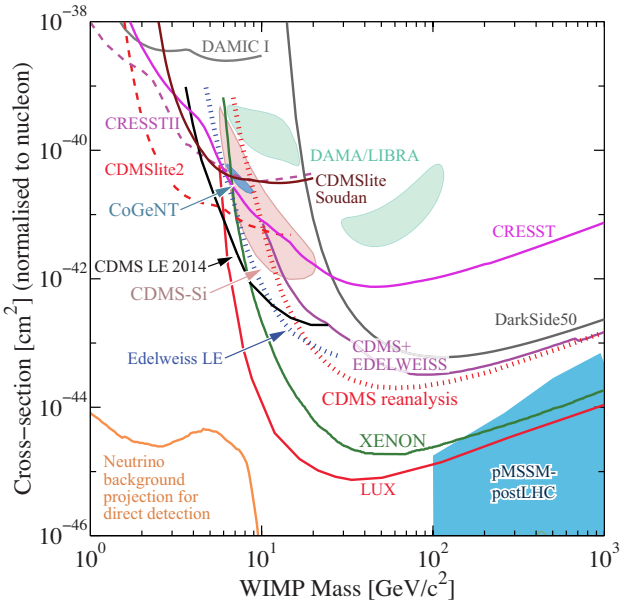

Figure 2.5: WIMP cross sections as function of WIMP mass in the spin-independent coupling scenario [4]. The cross sections are normalized to a single nucleon. The results are reported for different direct detection experiments. Also some supersymmetry results are reported: green and blue area refer to MSSM models.

Indirect detection

Complementary to direct detection, indirect detection approach is the technique to observe radiation produced in DM annihilations. These methods can explore higher masses and different coupling scenarios. Final radiation can be neutrinos, positrons, anti-protons and gamma-rays. Since the flux of this radiation is proportional to the annihilation rate, these searches point to regions where SM density is large.
Since neutrino is weakly interacting, its detection is more challenging with respect to gamma rays. Detectors are placed in the underground to suppress background and typically use Cherenkov techniques to identify neutrino interactions. Super-Kamiokande [19] and IceCube [20] are examples of neutrino telescopes which can measure the flux of muon neutrinos interacting with the Earth. Results can also be translated in terms of WIMP-nucleon cross section for direct detection comparison.
Gamma-rays production from WIMP annihilation mostly originate from the galactic centre, with gamma rays released from jets produced in WIMP annihilation, or directly produced in WIMPs decays such as $\chi\chi \rightarrow \gamma\gamma$ and

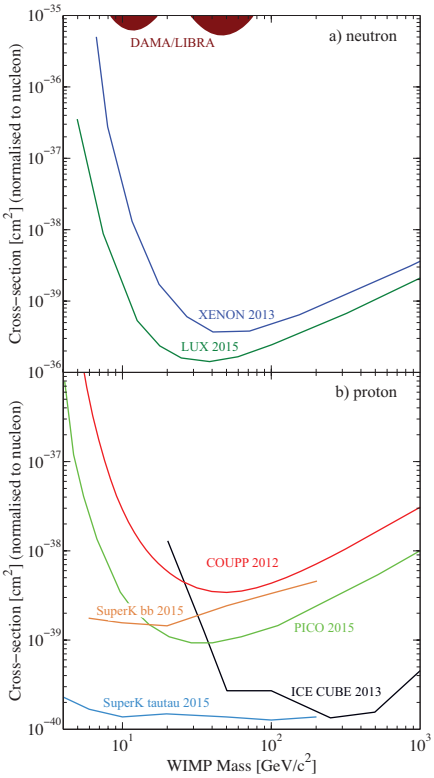

Figure 2.6: WIMP cross sections as function of WIMP mass in the spin-dependent coupling scenario for interactions with neutron (a) and proton (b) [4].

$\chi\chi \rightarrow \gamma Z$. To typical WIMP masses of thousands GeV correspond high energetic gamma-rays, whose detection would constitute a clear indication of DM annihilation. Fermi/LAT experiment reported a 3.2 σ excess in a search around the galactic centre [21].
Antiparticles such as positron and anti-protons produced in WIMP annihilations are subject to galactic magnetic field, they can be detected as excesses with respect to the background generated by known processes. Positron flux measurements come from PAMELA [22] and AMS-02 [23] experiments.

2.4.4 WIMP searches at LHC

If interactions between DM and SM particles exist they could be produced at LHC. Because WIMPs are weakly interacting, they do not deposit energy in the calorimeter, leading, for DM events, to a final signature with an unbalanced momentum in the transverse plane, where the kinematic is closed.

One way to observe them is when they are produced in association with a visible SM particle X (gluon, photon, quark, Z, W or Higgs) thus leading to the so called *mono-X* signature. In this section details about final state with jets and missing energy will be given.
During LHC Run-1 searches Effective Field Theory (EFT) approach was used. In this theoretical framework the interaction between DM and SM particles is described as contact interaction involving quark-antiquark pair, or two gluons and DM pair (Figure 2.7).

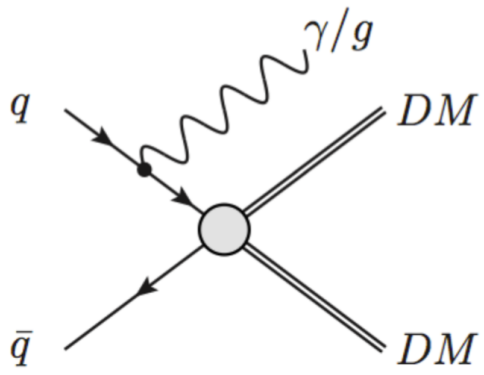

Figure 2.7: Feynman diagram for DM pair production through an EFT operator [24].

The mediator of the interaction (with mass M_{med}) is assumed to be too heavy to be produced, thus leading to a model described by only one parameter, the suppression scale M_*, which give a measurement of the validity of the EFT. EFT is valid when

$$M_* \gtrsim Q_{tr}, \tag{2.19}$$

where Q_{tr} is the momentum transfer.
The lower limit on M_* must satisfy some condition in order to have a valid EFT approach [24]. It is possible to relate it to a more complete description involving SM and DM couplings (g_q and g_χ) and the mediator mass. For example, if we consider the lowest dimensional operator

$$\mathcal{O}_S = \frac{1}{M_*^2}(\bar{\chi}\chi)(\bar{q}q), \tag{2.20}$$

we obtains the matching condition

$$\frac{1}{M_*^2} = \frac{g_\chi g_q}{M_{med}^2}. \tag{2.21}$$

The perturbative regime implies g_q ,$g_\chi < 4\pi$, and assuming $M_{med} > m_\chi$ and $Q_{tr} > 2m_\chi$ one obtains:

$$M_* > \frac{Q_{tr}}{\sqrt{g_q\, g_\chi}} > \frac{Q_{tr}}{4\pi} > \frac{m_\chi}{2\pi} \tag{2.22}$$

which gives the dependence of suppression scale from m_χ .
EFT provides an optimal way to compare results with non-collider DM searches: the limit on the suppression scale can be translated in terms of WIMP-nucleon scattering cross section.
With the large energies employed in LHC searches (especially from Run-2) a more detailed description can be achieved, leading to the *simplified DM models*, which are able to describe the full kinematics of the process. The interaction between SM and DM particles occurs via mediator in s- or t- channel. While more detailed than EFTs, simplified models are not a complete theory (like SUSY), since it does not cover the full parameter space and does not take into account all correlations between observables. On the other hand complete DM models suffer *the inverse problem*, that is the incapability to determine without ambiguities all parameters from a finite amount of data. Simplified models adopted in Run-2 searches follow the prescription of DM Forum [25] and are based on several assumptions:

- WIMPs are long-lived particles that escape LHC detectors: only Dirac fermion WIMP will be used in the models;
- The Lagrangian is built by adding additional terms to the SM one;
- The new interaction should not violate SM symmetries. In particular Minimal Flavour Violation (MFV) [26] is assumed, which implies that the SM flavour structure is preserved and ensures that a spin-0 resonance has a couplings to fermions proportional to the SM Higgs couplings. Baryon and lepton numbers are also conserved quantities.
- The models follow the minimal decay width (Γ) assumptions: only SM and DM decays are allowed.

Given these assumption the minimal set of parameters of simplified models are:

$$\{g_q\,, g_\chi\,, m_\chi\,, M_{med}\,\}. \tag{2.23}$$

DM production cross section is related to the size of the momentum transfer with respect to the mediator mass. From the following relation

$$\frac{1}{Q_{tr}^2 - M_{med}^2 + iM_{med}\,\Gamma} \tag{2.24}$$

three different cases are possible:

- off-shell mediator satisfying $Q^2_{tr} \gg M^2_{med}$ which yields suppressed cross sections depending on the couplings and not on mediator width ($\sigma \propto g_q^2 g_\chi^2$);
- on-shell mediator where $Q^2_{tr} \sim M^2_{med}$ and cross section are enhanced, thus providing the most interesting scenario at LHC searches: in the narrow width approximation $\Gamma \ll M_{med}$ which implies $\sigma \propto g_q^2 g_\chi^2/\Gamma$;
- $Q^2_{tr} \ll M^2_{med}$ case which addresses to EFT limit, with suppressed cross sections.

In the following details on spin-1 and spin-0 mediators will be given.

Vector and Axial-Vector Mediators

An additional U(1) gauge symmetry to the SM lagrangian leads to the introduction of a mediator in the interaction between SM and DM. For the s-channel spin-1 mediator exchange the diagram is illustrated in Figure 2.8.

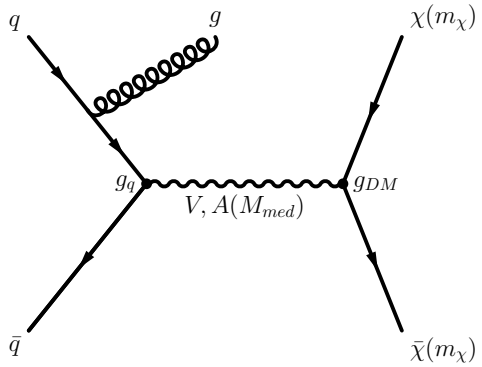

Figure 2.8: DM pair production via spin-1 mediator in association with an initial parton.

The lagrangians for models with vector and axial-vector mediators are

respectively:

$$\mathcal{L}_{\text{vector}} = g_q \sum_{q=u,d,s,c,b,t} Z'_\mu \bar{q}\gamma^\mu q + g_\chi Z'_\mu \bar{\chi}\gamma^\mu \chi \tag{2.25}$$

$$\mathcal{L}_{\text{axial-vector}} = g_q \sum_{q=u,d,s,c,b,t} Z'_\mu \bar{q}\gamma^\mu\gamma^5 q + g_\chi Z'_\mu \bar{\chi}\gamma^\mu\gamma^5 \chi\,. \tag{2.26}$$

where couplings g_q are the same for all the quarks. In the minimal decay width assumption one obtains:

$$\begin{aligned}\Gamma^{\text{V}}_{\text{min}} &= \frac{{g_\chi}^2 M_{med}}{12\pi}\left(1+\frac{2{m_\chi}^2}{{M_{med}}^2}\right)\beta_{DM}\theta(M_{med}-2m_\chi) \\ &+ \sum_q \frac{3{g_q}^2 M_{med}}{12\pi}\left(1+\frac{2m_q^2}{{M_{med}}^2}\right)\beta_q\theta(M_{med}-2m_q),\end{aligned} \tag{2.27}$$

$$\begin{aligned}\Gamma^{\text{A}}_{\text{min}} &= \frac{{g_\chi}^2 M_{med}}{12\pi}\beta^3_{DM}\theta(M_{med}-2m_\chi) \\ &+ \sum_q \frac{3{g_q}^2 M_{med}}{12\pi}\beta^3_q\theta(M_{med}-2m_q)\,.\end{aligned} \tag{2.28}$$

where $\beta_f = \sqrt{1-\frac{4m_f^2}{{M_{med}}^2}}$ is the velocity of a fermion with mass m_f.
The kinematic properties of this model have been studied as function of the parameters. Based on different choices of M_{med} and m_χ it was observed that the shape of kinematic distributions does not depend neither on the couplings nor on the mediator width, both for on-shell and off-shell cases. Figure 2.9 shows missing energy distribution for a fixed M_{med} and m_χ mass choice. For EFT limit, when mediators are extremely heavy, the missing energy distribution $E_{\text{T}}^{\text{miss}}$ is shown in Figure 2.10. Simplified models can reproduce with a good approximation an EFT model (in Figure 2.10 a D5 EFT model with 5 TeV mediator has been compared).

A scan over m_χ, by fixing M_{med} and couplings shows that in the on-shell regime shape distributions do not depend on the DM masses while a finer binning is needed for $M_{med} \sim 2m_\chi$ and off-shell cases (Figure 2.11).

The situation is reverted when scanning on M_{med}, showing (see Figures 2.12 and 2.13) different shape distributions for on-shell case and more similar shapes for off-shell mediators.

No significant shape differences have been found by comparing vector and axial-vector couplings as shown in Figure 2.14. The cross sections are found to be similar only for the on-shell regime.

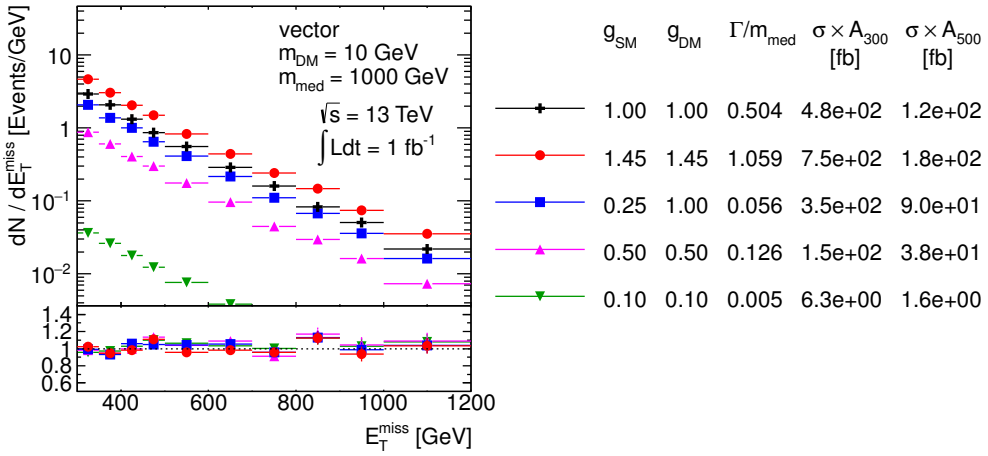

Figure 2.9: $E_{\mathrm{T}}^{\mathrm{miss}}$ distribution when scanning over couplings. Parameters used are listed in the plot. Ratios of the normalized distributions with respect to the first one are shown. A_{300} and A_{500} in the table denote the acceptance of the $E_{\mathrm{T}}^{\mathrm{miss}} > 300$ GeV and $E_{\mathrm{T}}^{\mathrm{miss}} > 500$ GeV cut, respectively [25].

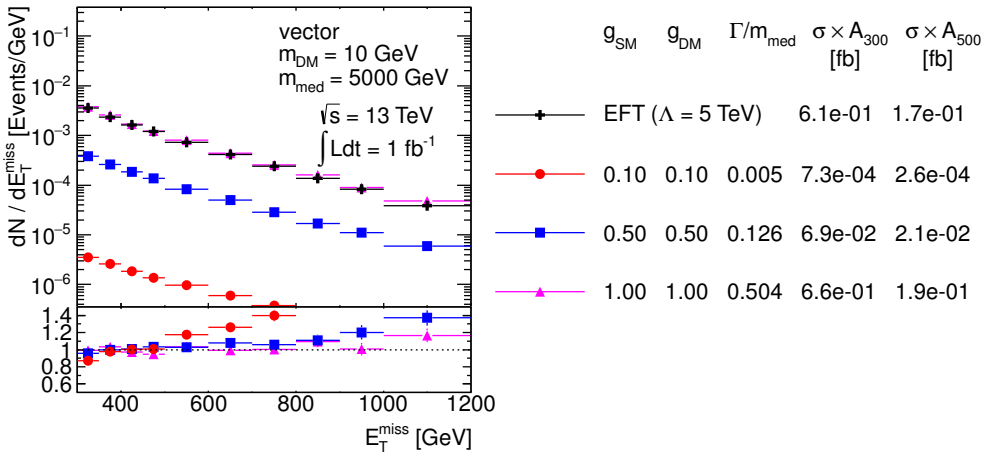

Figure 2.10: $E_{\mathrm{T}}^{\mathrm{miss}}$ comparison for the D5 EFT sample and simplified models with $M_{med} = 5$ TeV for various widths. Ratios of the normalized distributions with respect to the first one are shown. A_{300} and A_{500} in the table denote the acceptance of the $E_{\mathrm{T}}^{\mathrm{miss}} > 300$ GeV and $E_{\mathrm{T}}^{\mathrm{miss}} > 500$ GeV cut, respectively [25].

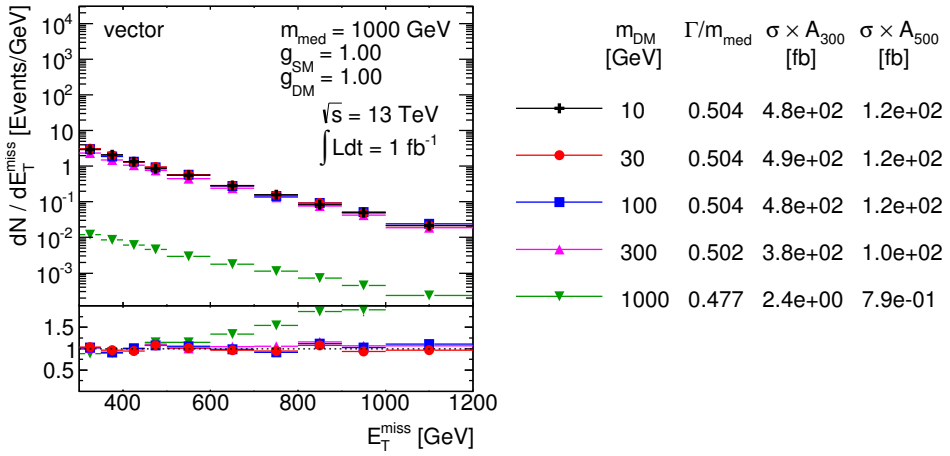

Figure 2.11: $E_{\mathrm{T}}^{\mathrm{miss}}$ distribution when scanning over m_{χ}. Parameters used are listed in the plot. Ratios of the normalized distributions with respect to the first one are shown. A_{300} and A_{500} in the table denote the acceptance of the $E_{\mathrm{T}}^{\mathrm{miss}} > 300$ GeV and $E_{\mathrm{T}}^{\mathrm{miss}} > 500$ GeV cut, respectively [25].

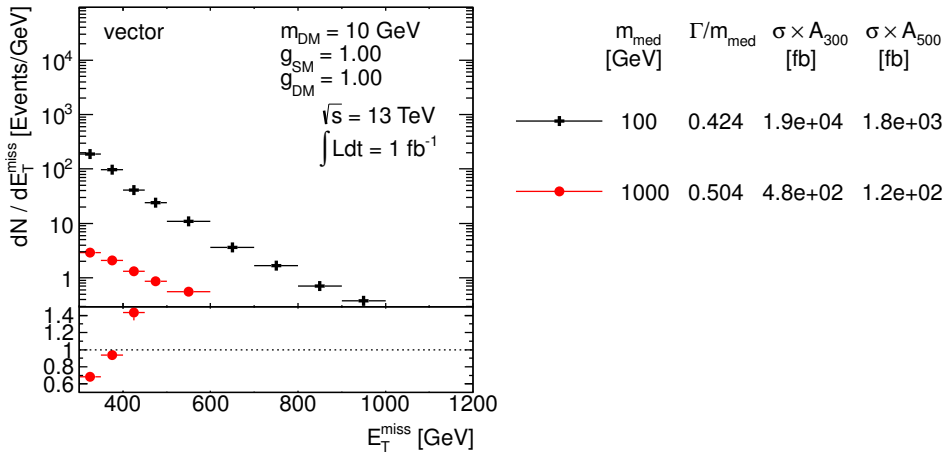

Figure 2.12: $E_{\mathrm{T}}^{\mathrm{miss}}$ distribution when scanning over M_{med}. Parameters used are listed in the plot. Ratios of the normalized distributions with respect to the first one are shown. A_{300} and A_{500} in the table denote the acceptance of the $E_{\mathrm{T}}^{\mathrm{miss}} > 300$ GeV and $E_{\mathrm{T}}^{\mathrm{miss}} > 500$ GeV cut, respectively [25].

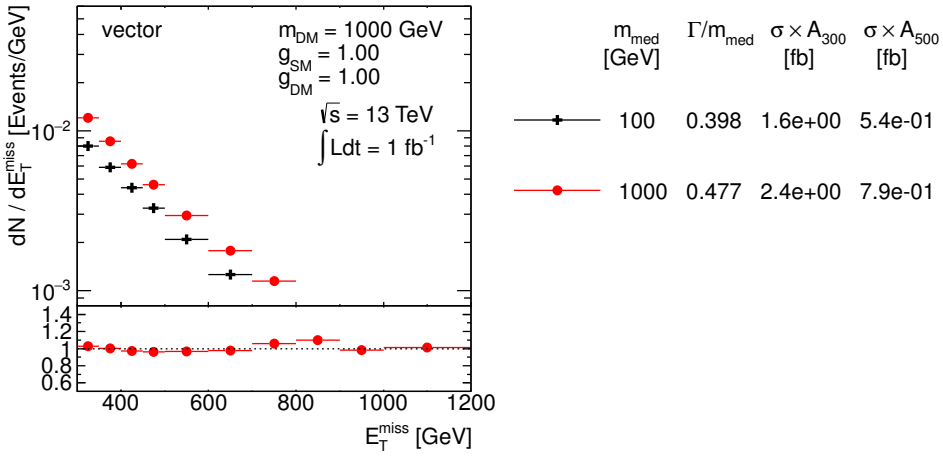

Figure 2.13: $E_{\mathrm{T}}^{\mathrm{miss}}$ distribution when scanning over M_{med}. Parameters used are listed in the plot. Ratios of the normalized distributions with respect to the first one are shown. A_{300} and A_{500} in the table denote the acceptance of the $E_{\mathrm{T}}^{\mathrm{miss}} > 300$ GeV and $E_{\mathrm{T}}^{\mathrm{miss}} > 500$ GeV cut, respectively [25].

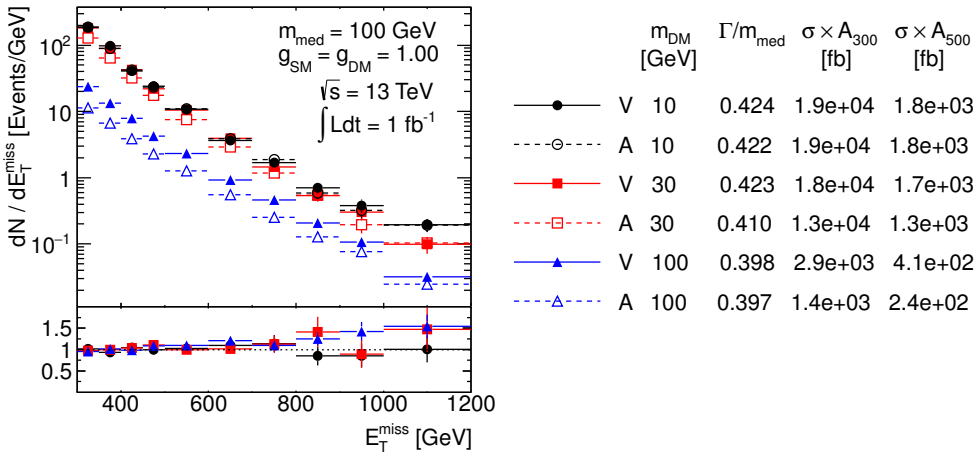

Figure 2.14: Comparison of the pure vector and pure axial-vector couplings. The $E_{\mathrm{T}}^{\mathrm{miss}}$ distribution is shown for the samples generated with $M_{med} = 100$ GeV and different Dark Matter masses. Ratios of the normalized distributions are shown for between the samples with coincident masses. A_{300} and A_{500} in the table denote the acceptance of the $E_{\mathrm{T}}^{\mathrm{miss}} > 300$ GeV and $E_{\mathrm{T}}^{\mathrm{miss}} > 500$ GeV cut, respectively [25].

Scalar and Pseudoscalar Mediators

A spin-0 resonance model would lead to an interaction with the SM Higgs field. In the following a simpler case without mediator-Higgs mixing will be described. These processes are loop suppressed giving the diagrams in Figure 2.15 with the interaction lagrangians:

$$\mathcal{L}_\phi = g_\chi \, \phi \bar{\chi} \, \chi \, + \frac{\phi}{\sqrt{2}} \sum_i \left(g_u y_i^u \bar{u}_i u_i + g_d y_i^d \bar{d}_i d_i + g_\ell y_i^\ell \bar{\ell}_i \ell_i \right) \, , \tag{2.29}$$

$$\mathcal{L}_a = i g_\chi \, a \bar{\chi} \, \gamma_5 \chi \, + \frac{ia}{\sqrt{2}} \sum_i \left(g_u y_i^u \bar{u}_i \gamma_5 u_i + g_d y_i^d \bar{d}_i \gamma_5 d_i + g_\ell y_i^\ell \bar{\ell}_i \gamma_5 \ell_i \right) \, . \tag{2.30}$$

where the couplings g_q are assumed universal for all SM particles and the Yukawa couplings y_i^f are normalized to the Higgs vacuum expectation value as $y_i^f = \sqrt{2} m_i^f / v$. The scan over the parameters resulted in the same conclusions found for spin-1 case, as shown in Figures 2.16-2.20.

Scalar and Pseudoscalar Mediators in association with heavy quarks

Although one would expect that monojet inclusive searches provide the most solid limits for DM searches (since cross sections are highest) when mediators are scalar or pseudoscalar, a dedicated search with tagged jets could probe interesting scenarios. For example it could explore the case when up- and down-type couplings are not universal or if the loop-induced gluon

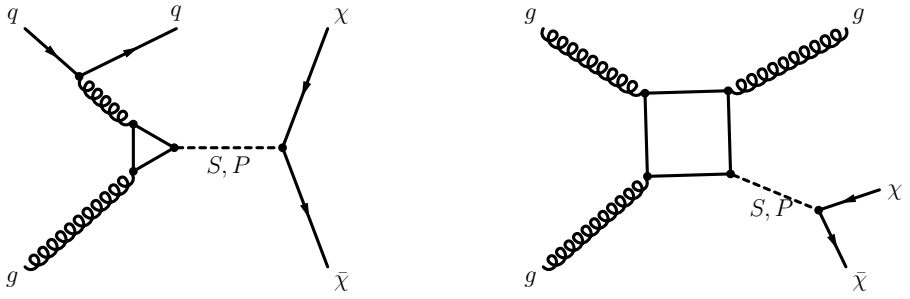

(a) **(b)**

Figure 2.15: One-loop process with exchange of scalar or pseudoscalar mediator in the s-channel.

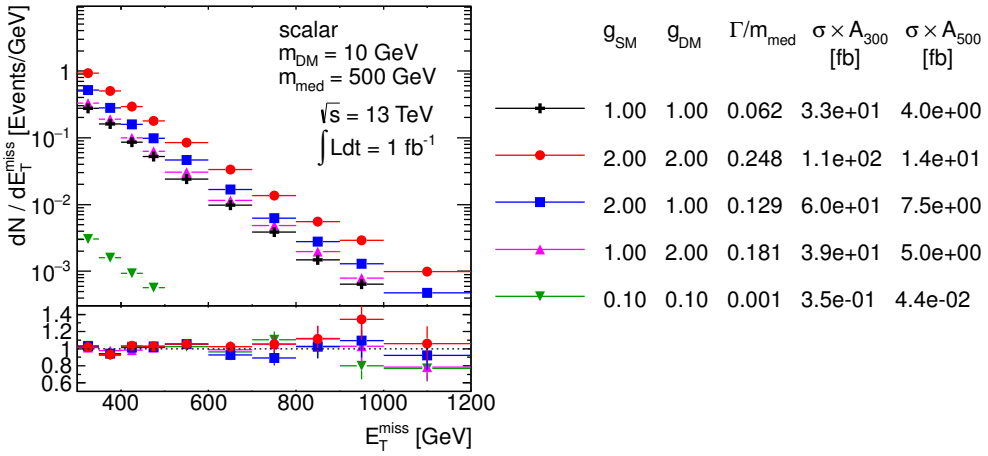

Figure 2.16: $E_{\mathrm{T}}^{\mathrm{miss}}$ distribution when scanning over couplings. Parameters used are listed in the plot. Ratios of the normalized distributions with respect to the first one are shown. A_{300} and A_{500} in the table denote the acceptance of the $E_{\mathrm{T}}^{\mathrm{miss}} > 300$ GeV and $E_{\mathrm{T}}^{\mathrm{miss}} > 500$ GeV cut, respectively [25].

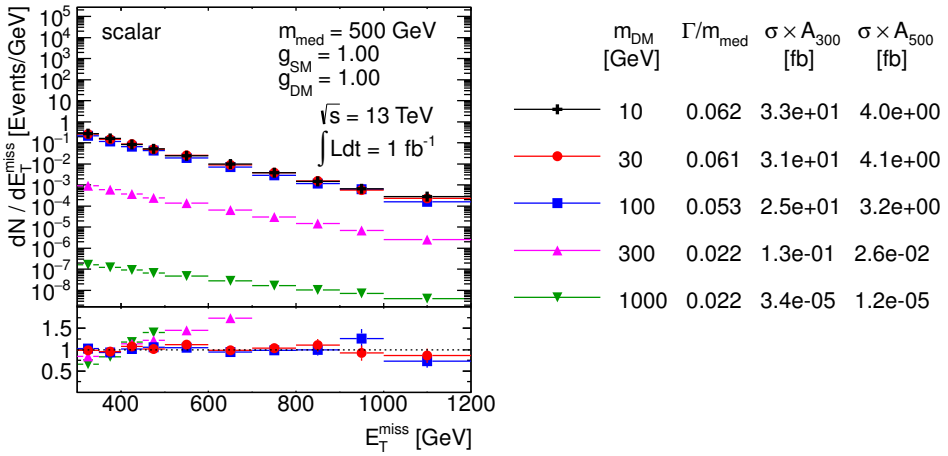

Figure 2.17: $E_{\mathrm{T}}^{\mathrm{miss}}$ distribution when scanning over m_{χ}. Parameters used are listed in the plot. Ratios of the normalized distributions with respect to the first one are shown. A_{300} and A_{500} in the table denote the acceptance of the $E_{\mathrm{T}}^{\mathrm{miss}} > 300$ GeV and $E_{\mathrm{T}}^{\mathrm{miss}} > 500$ GeV cut, respectively [25].

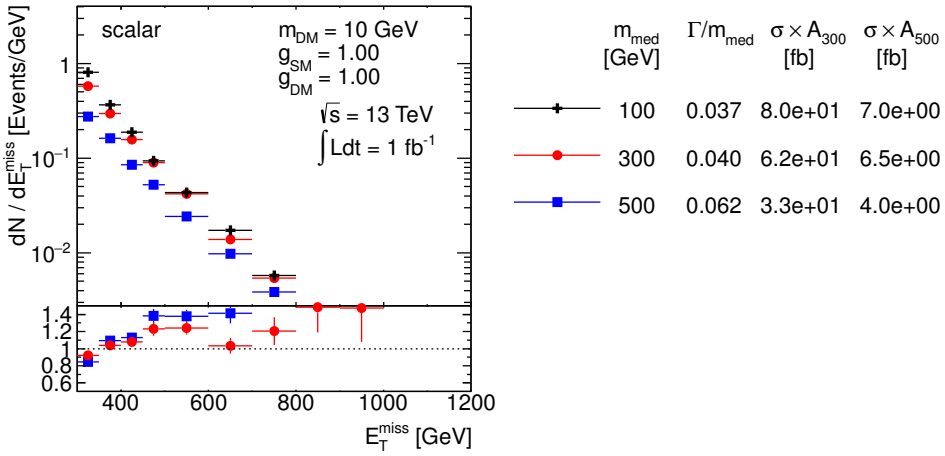

Figure 2.18: $E_{\mathrm{T}}^{\mathrm{miss}}$ distribution when scanning over M_{med}. Parameters used are listed in the plot. Ratios of the normalized distributions with respect to the first one are shown. A_{300} and A_{500} in the table denote the acceptance of the $E_{\mathrm{T}}^{\mathrm{miss}} > 300$ GeV and $E_{\mathrm{T}}^{\mathrm{miss}} > 500$ GeV cut, respectively [25].

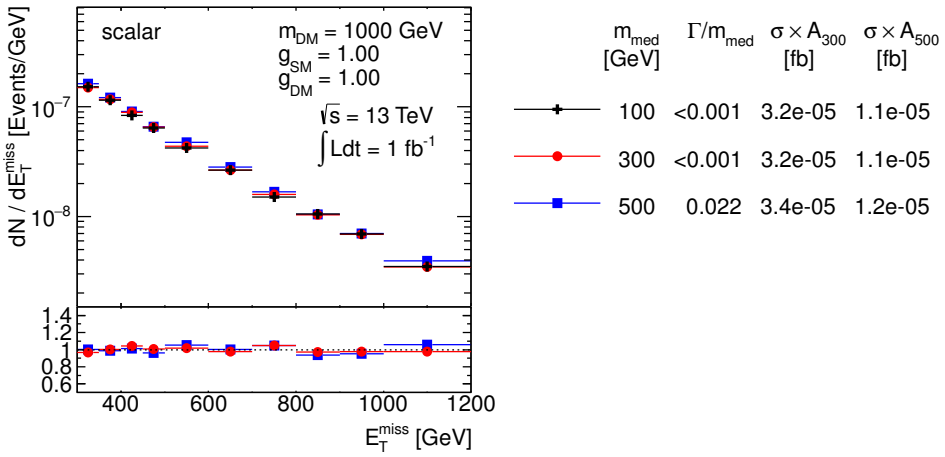

Figure 2.19: $E_{\mathrm{T}}^{\mathrm{miss}}$ distribution when scanning over M_{med}. Parameters used are listed in the plot. Ratios of the normalized distributions with respect to the first one are shown. A_{300} and A_{500} in the table denote the acceptance of the $E_{\mathrm{T}}^{\mathrm{miss}} > 300$ GeV and $E_{\mathrm{T}}^{\mathrm{miss}} > 500$ GeV cut, respectively [25].

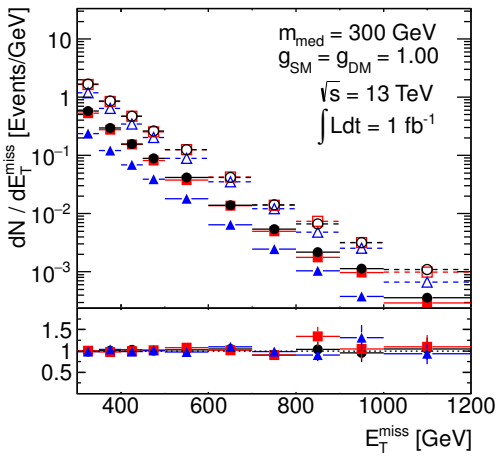

	m_{DM} [GeV]	Γ/m_{med}	$\sigma \times A_{300}$ [fb]	$\sigma \times A_{500}$ [fb]
S	10	0.040	6.2e+01	6.5e+00
P	10	0.040	1.8e+02	1.9e+01
S	30	0.037	5.8e+01	6.0e+00
P	30	0.039	1.8e+02	1.9e+01
S	100	0.017	2.6e+01	2.9e+00
P	100	0.030	1.3e+02	1.5e+01

Figure 2.20: Comparison of the $E_{\mathrm{T}}^{\mathrm{miss}}$ distributions for the scalar and pseudoscalar models for different $M_{med} = 300\,\mathrm{GeV}$ and different Dark Matter masses. Ratios of the normalized distributions with respect to the first one are shown. A_{300} and A_{500} in the table denote the acceptance of the $E_{\mathrm{T}}^{\mathrm{miss}} > 300$ GeV and $E_{\mathrm{T}}^{\mathrm{miss}} > 500$ GeV cut, respectively [25].

coupling does not depend only on top and bottom quarks, then it is possible that other production mechanism are strongly suppressed in the monojet channel. As previously described the MVF assumption for spin-0 mediators privileges coupling with top and bottom quarks leading to the diagrams in Figure 2.21.

For the b-tagged channel a lower sensitivity is expected with respect to top and monojet channels. However it could provide information on down-sector and eventual deviations from universal coupling assumption that can not be observed in top channel since it has the same coupling as the loop-induced monojet channel. Moreover some theoretical models (like 2HDM and pMSSM) predict coupling of spin-0 mediators to down generation quarks, motivating the study of final states with bottom quarks, in order to probe the b-quark coupling.

The kinematical distributions depends on M_{med} and m_χ (Figures 2.22 and 2.23 have same behaviour both for $\bar{t}t$ and $\bar{b}b$ case. The $E_{\mathrm{T}}^{\mathrm{miss}}$ spectrum broadens with larger M_{med}, and also depends on on-shell and off-shell cases, as previously discussed. There's no strong dependence on the couplings and the width except for the case where M_{med} is slightly larger than $2m_\chi$ as shown in Figure 2.24.

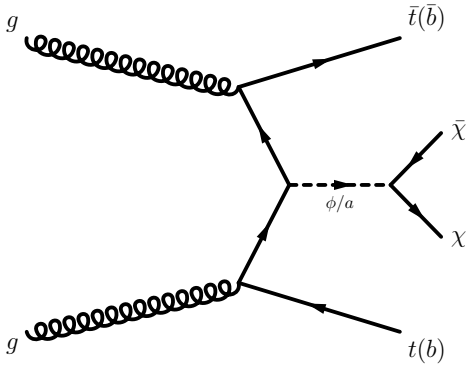

Figure 2.21: DM pair production via spin-0 mediator in association with $\bar{t}t$ or $\bar{b}b$.

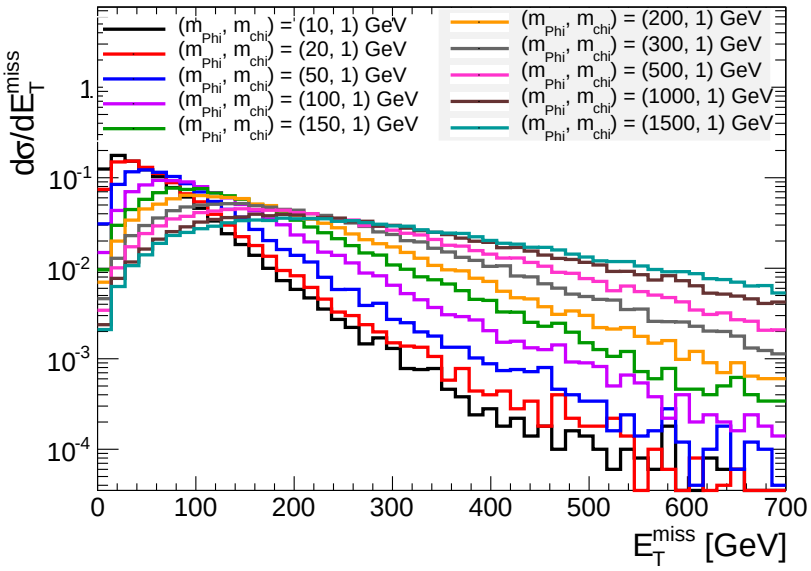

Figure 2.22: $E_{\mathrm{T}}^{\mathrm{miss}}$ distribution in the $\bar{t}t$ case for scalar mediator [25].

b-quark signatures in t-channel

In order to explain the Galactic Center gamma ray excess observed by the Fermi-LAT collaboration [27] a new model involving bottom quark in t-channel has been introduced [28]. The bottom Flavoured Dark Matter (b-FDM) assumption is that DM privileges down-type quark couplings. The model includes a Dirac fermion transforming as a flavour triplet, and its third

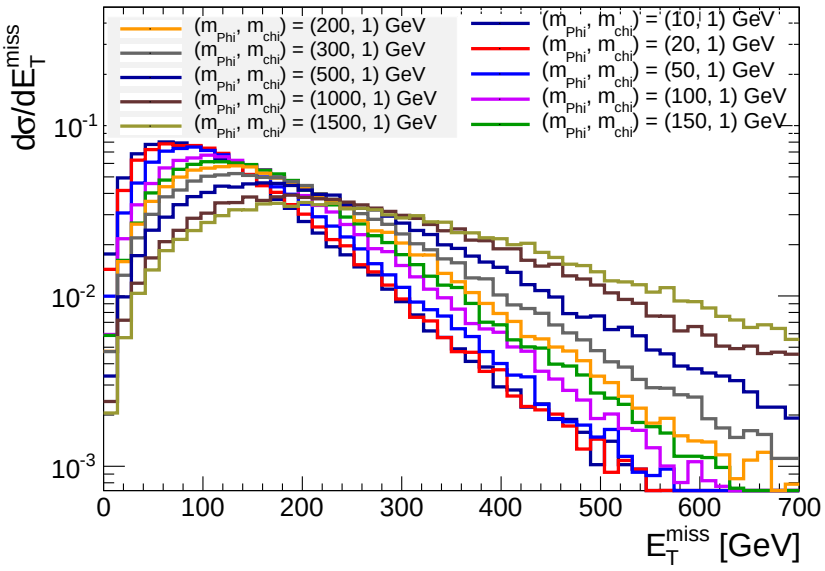

Figure 2.23: $E_{\mathrm{T}}^{\mathrm{miss}}$ distribution in the $\bar{t}t$ case for pseudoscalar mediator [25].

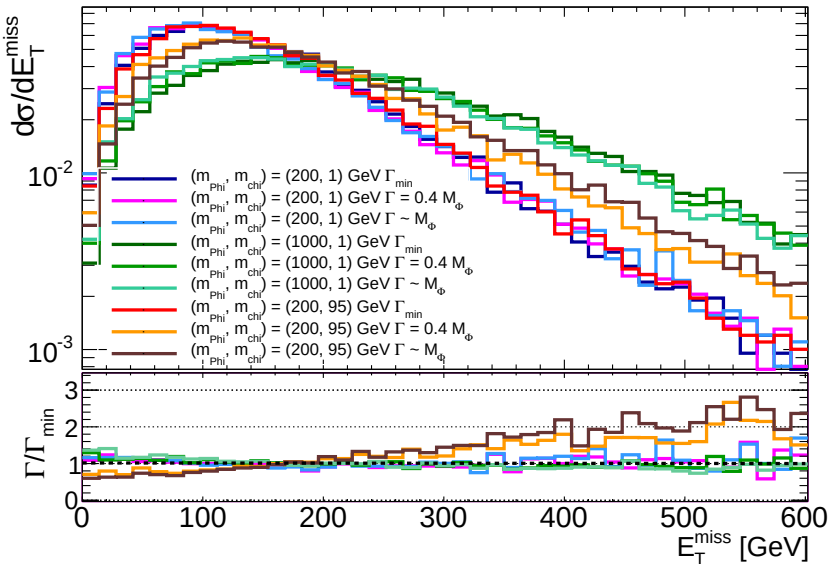

Figure 2.24: $E_{\mathrm{T}}^{\mathrm{miss}}$ distribution in the $\bar{t}t$ case. The width dependence becomes relevant when M_{med} is slightly larger than $2m_{\chi}$ [25].

component χ_b comprises the cosmological DM. The interaction between SM and DM is mediated via a flavour singlet, colour triplet scalar field Φ under MFV assumption. The lagrangian considered is:

$$\mathcal{L} \supset g\Phi^* \bar{\chi}_b b_R + \text{h.c.}. \tag{2.31}$$

The corresponding diagram is shown in Figure 2.25.

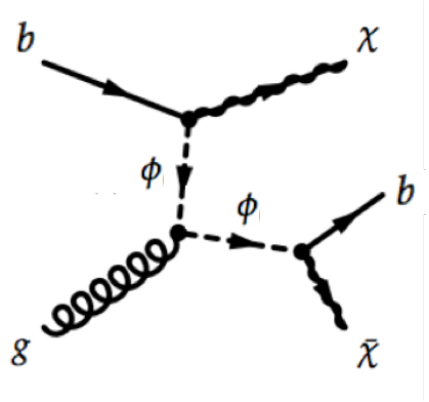

Figure 2.25: b-FDM Feynman diagram.

Chapter 3

The ATLAS experiment at LHC

The *Large Hadron Collider* (LHC) [29] is a proton-proton high energy collider. Particles created in these collisions are detected by four big experiments: ALICE, ATLAS, CMS and LHCb[1]. In this chapter details about LHC and ATLAS experiment will be given.

3.1 Large Hadron Collider

The Large Hadron Collider (LHC) [32] is a proton-proton particle accelerator placed in the same tunnel where LEP accelerator operated in the past. LHC is the largest and most powerful particle accelerator in the world, based at CERN (Conseil Européen pour la Recherche Nucléaire) near Geneva, Switzerland (Figure 3.1). The maximum reachable energy of each proton beam is 7 TeV, with a design luminosity of $L = 10^{34}\ cm^{-2}\ s^{-1}$. LHC can also collide heavy (Pb) ions providing Pb-Pb or proton-Pb collisions, with a nominal luminosity of $L = 10^{27}\ cm^{-2}\ s^{-1}$.
LHC is a two-ring-superconducting accelerator, with a circumference of 26.7 km. The entire LHC experimental area is based on the border between Switzerland and France.

3.1.1 Technical design

The LHC physics programme aims at searches for new physics phenomena. After the successful Higgs boson discovery, the main goals are the

[1]LHC experimental area also hosts two minor experiments: Totem [30] and LHCf [31].

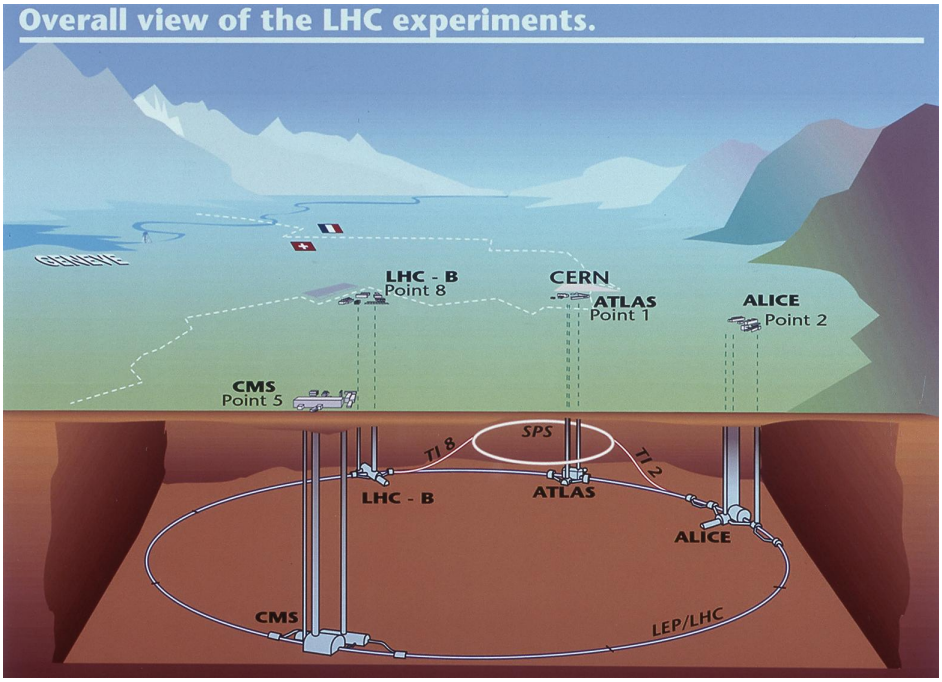

Figure 3.1: Overall view of the LHC experiments.

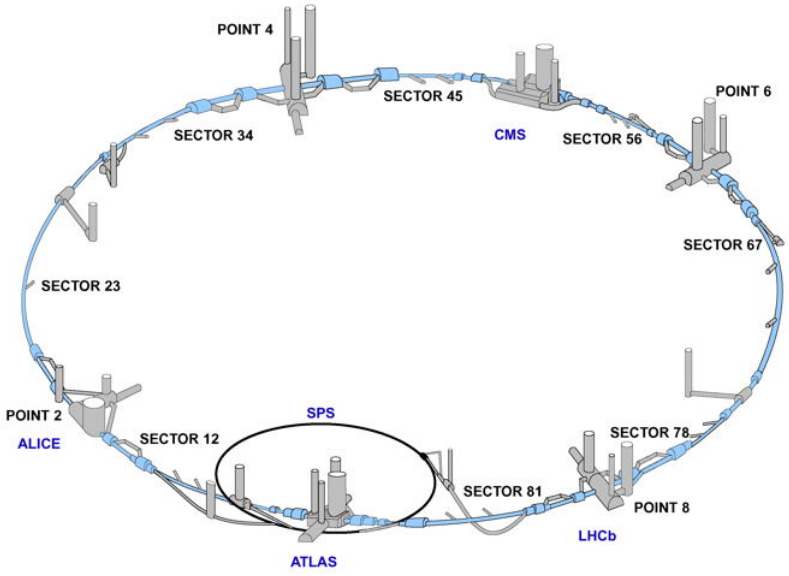

Figure 3.2: Placement of the main experiments at LHC.

measurements of its properties, and searches for Beyond Standard Model Physiscs (SUSY, DM). Exploiting the energy frontier is both a technical and experimental challenge: it requires an excellent design and operation of the accelerator complex, together with a deep understanding of each detector subsystem.

Layout

The LHC provides collisions in four collision points along its circumference where detector experiments are located.
Since LHC accelerates two beams of same sign particles, two separate accelerating cavities and two different magnetic fields are needed: LHC is equipped with 1232 superconducting magnets and 16 radiofrequency cavities which bend and accelerate the proton beams in the two parallel beam lines in the machine. The magnetic field used to bend such energetic proton beams is of 8.3 T and to reach this value the superconducting magnets are cooled down to 1.9 K and a 13 kA current circulates inside them.

Eight experimental halls are built. The LHC has eight arcs and eight straight sections. Each straight section is approximately 528 m long and can serve as an experimental or utility insertion. The two highest luminosity experimental area, where ATLAS and CMS experiments are located, are placed at opposite straight sections: Point 1 and Point 5 (Figure 3.2). ALICE and LHCb are respectively located in Point 2 and Point 8 (Figure 3.2), where the machine has the minimum luminosity. Two more experimental insertions are located at Point 2 and Point 8, which also include the injection systems for Beam 1 and Beam 2, respectively. The injection kick occurs in the vertical plane with the two beams arriving at the LHC from below the LHC reference plane. The beams cross from one magnet bore to the other at four locations. The remaining four straight sections do not have beam crossings. Insertions at Points 3 and 7 each contain two collimation systems. The insertion at Point 4 contains two RF systems: one independent system for each LHC beam. The straight section at Point 6 contains the beam dump insertion, where the two beams are vertically extracted from the machine using a combination of horizontally deflecting fast-pulsed ('kicker') magnets and vertically-deflecting double steel septum magnets.

Accelerating mechanism

To reach the designed energy, the protons are accelerated in several steps. The accelerator chain is a succession of machines with increasingly higher energies as illustrated in Figure 3.3. From proton source to final step we find:

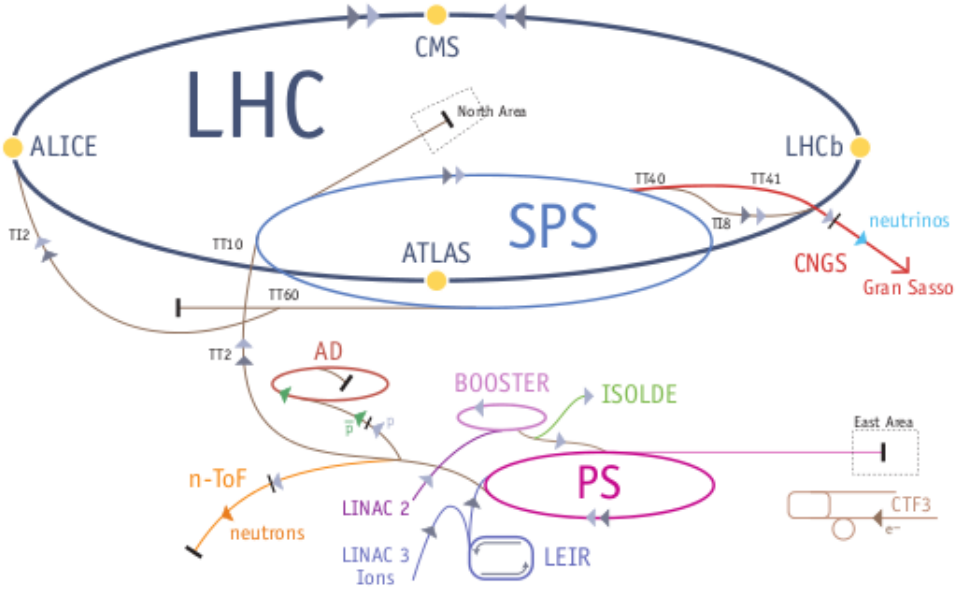

Figure 3.3: Accelerator facilities at LHC.

- LINAC2
- Proton Synchrotron Booster (PSB)
- Proton Synchrotron (PS)
- Super Proton Synchroton (SPS)
- LHC

A proton beam is produced from H_2 gas and then accelerated with a 300 mA beam current. Protons are then injected into the PSB at an energy of 50 eV from the LINAC2. The PSB accelerates the protons up to 1.4 GeV and the proton beams are injected to the PS where they are accelerated to 25 GeV. The protons are then sent to the SPS where they reach an energy of 450 GeV. Finally, the beams are transferred to the LHC where beams are circulated both in clockwise and anticlockwise direction while reaching their final energy. The injected beam will be captured, accelerated and stored using a 400 MHz superconducting cavity system.

Protons are collected in *bunches* of particle. Collisions take place when bunches coming from the two beams interact each other (*bunch crossing*): the design bunch crossing periods is about 25 ns.

Machine luminosity

The event number generated during collisions is

$$N_{ev} = L \cdot \sigma_{ev}, \tag{3.1}$$

where σ_{ev} is the cross section of the event and L is the machine luminosity. The latter depends on its intrinsic features:

$$L = \frac{N_b^2 n_b f_{rev} \gamma_r}{4\pi\epsilon_n \beta^*} F, \tag{3.2}$$

where N_b is the number of protons in each bunch, n_b the number of bunches circulating in the beam, f_{rev} is the revolution frequency, γ_r is the gamma relativistic factor, ϵ_n is the beam emittance[2], β^* is the beta function at the collision point[3], F is the luminosity reduction factor due to the crossing angle at the interaction point (IP). LHC luminosity is not constant on an entire data taking cycle (*run*). The main reason of the luminosity decay during a physics run is the beam loss from collisions. The initial decay time of the bunch intensity, due to this effect, is:

$$\tau_{nuclear} = \frac{N_{tot}(0)}{L\sigma_{tot}k}, \tag{3.3}$$

where $N_{tot}(0)$ is the beam intensity, L the initial luminosity, σ_{tot} the total cross section and k the number of interaction points. Further contributions to beam losses are related to intrabeam scattering (IBS), and the interaction between particles on residual gas, to which a corresponding decay constant is assigned. If we approximate the decay by an exponential process, the luminosity lifetime can be estimated as:

$$\frac{1}{\tau_L} = \frac{1}{\tau_{IBS}} + \frac{1}{\tau_{gas}} + \frac{1}{\tau_{nuclear}}, \tag{3.4}$$

Assuming

$$\begin{aligned} \tau_{IBS} &= 80\ h \\ \tau_{gas} &= 100\ h \\ \tau_{nuclear} &= 29\ h \end{aligned}$$

[2]The emittance ϵ is defined as the product of the width position distribution of bunch particles σ and momentum width, σ'.

[3]β^* function, known as betatron oscillation, is defined as $\frac{\sigma}{\sigma'}$.

One obtains

$$\tau_L = 14.9\ h \tag{3.5}$$

Integrating luminosity over a run one obtains:

$$L_{int} = L_0 \tau_L \left[1 - e^{-T_{run}/\tau_L}\right] \tag{3.6}$$

where T_{run} is the total length of luminosity run. The overall machine efficiency depends on the L_{int} parameters. Assuming the machine operates for 200 days per year, if the 3.5 holds, the optimum run time is 12 hours, for a maximum total integrated luminosity per year of 80 fb^{-1} to 120 fb^{-1}.

3.1.2 LHC experiments

The main four experiments at LHC, hosted in the four collision points are:

- ATLAS (**A** **T**oroidal **L**HC **A**pparatu**S**) [33];
- CMS (**C**ompact **M**uon **S**olenoid) [34];
- LHCb [35];
- ALICE (**A** **L**arge **I**on **C**ollider **E**xperiment) [36];

ATLAS and CMS are multi-purpose detectors, the main goals are Higgs physics, Standard Model precision measurements and search for beyond Standard Model physics.
ALICE focuses on the quark-gluon plasma searches, produced in heavy-ions collisions.
LHCb focuses on the study of CP violation processes occurring in b and c hadron decays.

3.1.3 Run-1 data taking

The first LHC operations started in autumn 2008, but they were interrupted due to a problem to superconducting magnets. The repair required a long technical intervention. In November 2009 operations resumed with pp collisions with a center of mass energy of 900 GeV, followed by $\sqrt{s} = 7$ TeV from March 2010 to the end of 2011. In 2012 the energy reached 8TeV per beam. Figure 3.4 reports the integrated luminosity collected by the ATLAS experiment in 2011, 2012 and in total, while Figure 3.5 shows the number of bunches per data taking year.

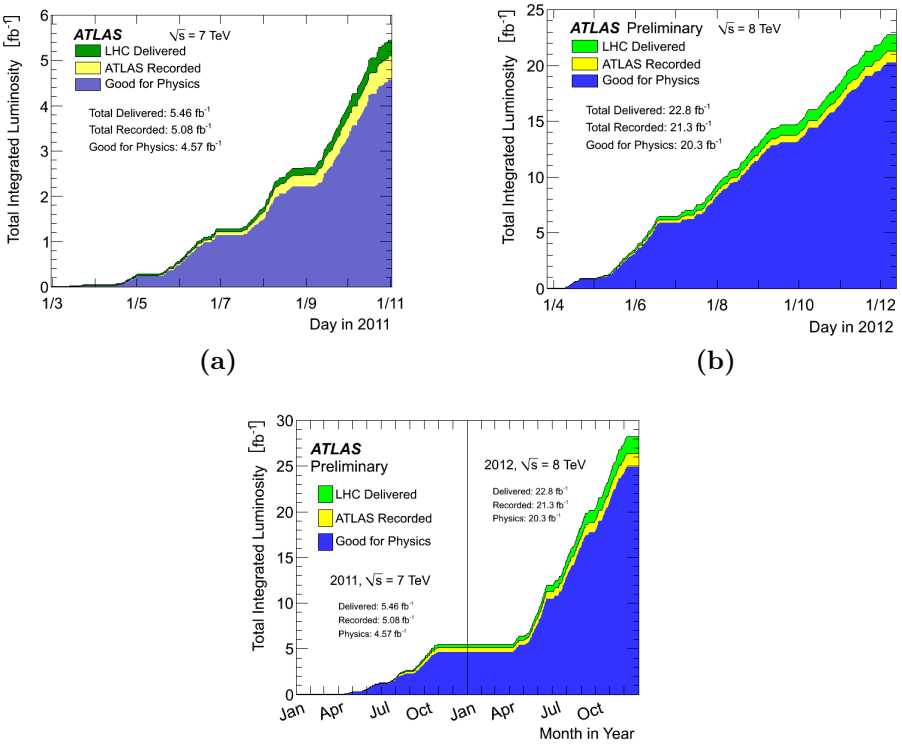

Figure 3.4: Integrated luminosity collected by the ATLAS experiment during LHC Run-1 data taking, in 2011 (a), 2012(b) and total (c) [37].

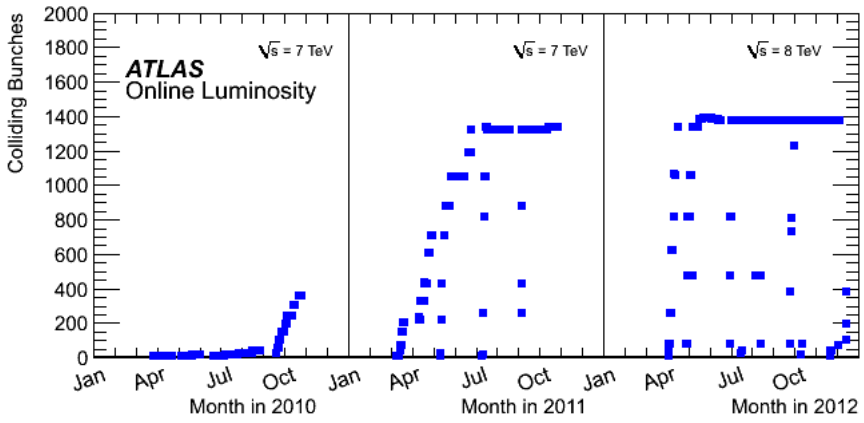

Figure 3.5: Number of bunches during LHC data taking in 2010, 2011 and 2012 [37].

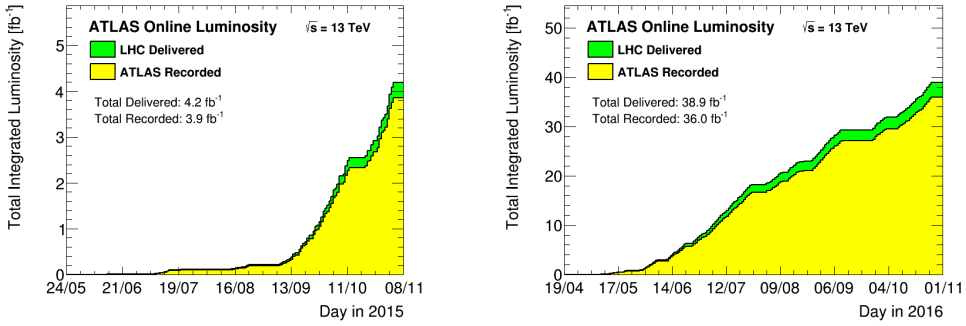

(a) **(b)**

Figure 3.6: Integrated luminosity collected by the ATLAS experiment at the LHC during 2015 (a) and 2016(b) operations [38].

3.1.4 Run-2 data taking

In 2015 the second phase of event production at LHC, called *Run-2* started. During the Run-2 the LHC will reach its design energy collision, 14 TeV, aiming to collect data corresponding to an integrated luminosity of 100 fb^{-1} during $2015 - 2018$. The initial phase of Run-2 performed collision with 50 ns bunch spacing integrating a total luminosity of 1 fb^{-1}; the data collected were dedicated to control the performances of the magnet and of the alignment of the spectrometer. Just after the commissioning phase the beams, characterized by $25\,ns$ bunch-spacing, circulated in the accelerator and produced collisions at $\sqrt{s} = 13\,TeV$ with a peak luminosity of $5,0 \cdot 10^{33} cm^{-2} s^{-1}$. The total integrated luminosity as a function of the days of running during 2015 and 2016 are represented in Figure 3.6. At the end of June, beams were maintained in the accelerator for a record of 37 consecutive hours. But the main indicator of success for the operators is luminosity, the measurement of the number of potential collisions in a given time period. On 29 June, peak luminosity exceeded $10^{34}\,cm^{-2}s^{-1}$. This represents a success for the LHC operators because it corresponds to the ultimate objective defined by those who originally designed the LHC machine.

3.2 The ATLAS experiment

The experimental ATLAS [39] apparatus has the following structure:

- An Inner Detector (ID), placed in a solenoidal superconducting magnet, for charged track identification and reconstruction, and for momentum and direction measurement.

- Electromagnetic and hadronic caloremeter to measure energy deposited by electrons photons and hadrons.
- Muon Spectrometer (MS), for muon identification and reconstruction. An air-cored superconductiong toroidal magnet system provides the magnetic filed to the MS.
- The trigger system, to effectively reduce background before recording events.
- The data acquisition system, to store interesting events.

The wide range of particles to be detected imposes very stringent requirements on the detector:

- Radiation-hard electronics and sensor elements in combination with fast readout of high granularity detector elements to handle the particle flux and reduce the influence of pile-up.
- Large acceptance in pseudorapidity (η) and full azimuthal angle coverage.
- Good momentum resolution and good particle reconstruction in the inner detector to allow primary and secondary vertex reconstruction.
- Very good electromagnetic and hadronic calorimetry to allow electrons, photons, jets and missing transverse energy reconstruction and measurement.
- An optimal muon identification and muon momentum resolution is required.
- Fast and highly efficient trigger on events of interest to achieve an acceptable rate of events to be stored.

The ATLAS detector is shown in Figure 3.7. It is 20 m tall and 45 m long and weights more than 7000 tons. In the following sections details about its sub-detectors will be given.

3.2.1 ATLAS coordinate system

Two different coordinate systems are used in the ATLAS experiment, according to the needs: a cartesian coordinate system for geometry studies, and a spherical coordinate system mostly used in physics analyses. The

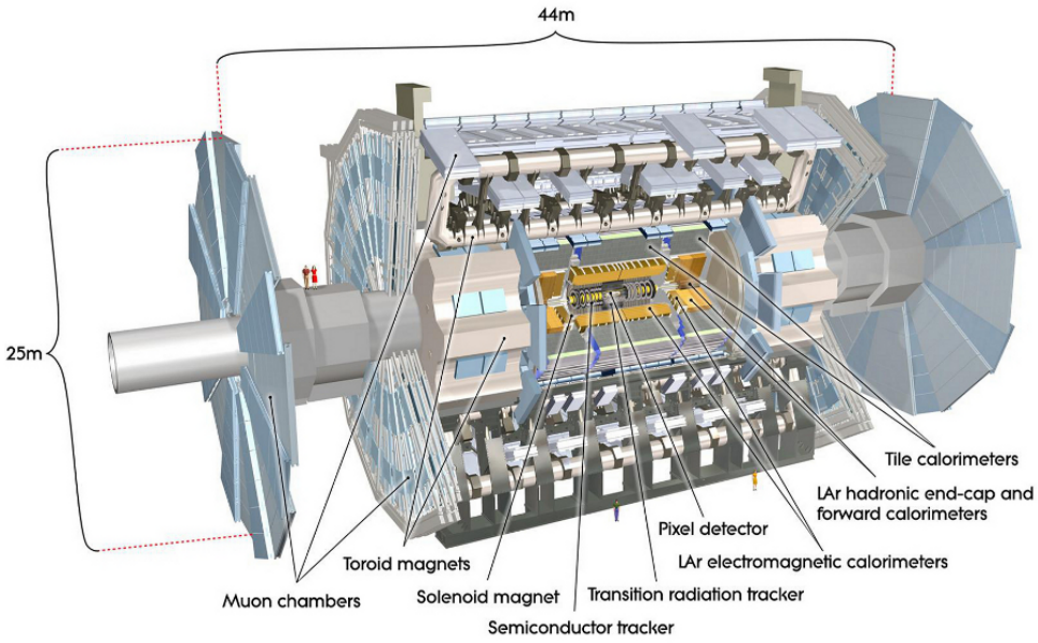

Figure 3.7: ATLAS detector at LHC.

nominal interaction point is the origin, while the beam direction defines the z axis and the $x - y$ plane is transverse to the beam direction. The x axis points to the center of the LHC ring, the y axis goes upwards. The interaction point defines two regions, with $z > 0$ and $z < 0$, called respectively side A and side C. The $z = 0$ plane defines side B (see Figure 3.8).

In spherical coordinate the azimuthal angle $\phi \in [-\pi, \pi]$ is measured in $x - y$ plane and is defined as:

$$\phi = \frac{1}{\tan(x/y)}. \tag{3.7}$$

where ϕ is zero in correspondance of the x axis and grows in clockwise direction in positive z direction. The polar angle θ is the angle from the z axis in the $y - z$ plane.
Pseudorapidity is defined as:

$$\eta = -ln\left[\tan\frac{\theta}{2}\right], \tag{3.8}$$

η (Figure 3.9) is 0 at $\theta = \pi/2$ (*barrel*), growing asymptotically for $\theta \to 0$

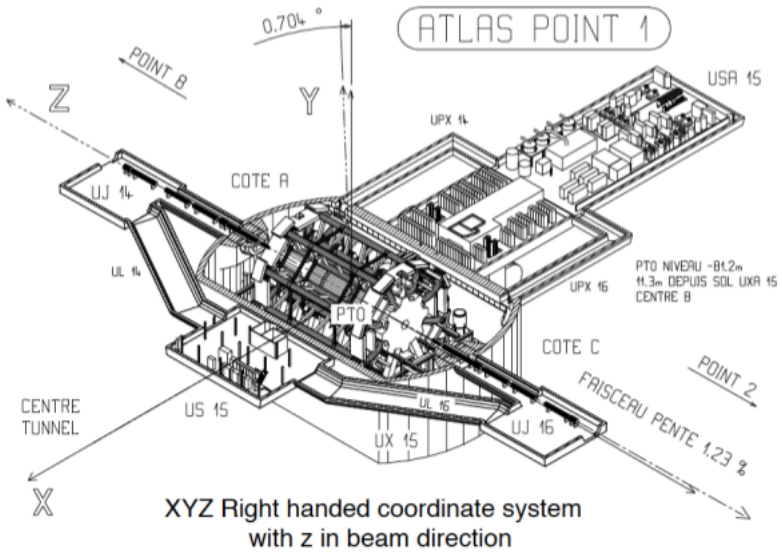

Figure 3.8: ATLAS coordinate system.

(*endcap*). For massive objects (like jets) rapidity is adopted:

$$y = \frac{1}{2} ln \left[\frac{E + p_L}{E - p_L} \right], \tag{3.9}$$

where p_L is the longitudinal momentum component.
The quantity:

$$\Delta R \equiv \sqrt{(\Delta\eta)^2 + (\Delta\phi)^2} \tag{3.10}$$

is used for measuring angular distance between two tracks in the $\eta - \phi$ plane. LHC collisions does not occur via elementary particles, but rather via composite particles (containing quarks and gluons). The energy in the center-of-mass system depends on the momenta of the partons involved in the interaction and is unknown. As a consequence, the kinematics is studied in the transverse plane $x - y$, where energy and momentum are conserved.

3.3 ATLAS experimental apparatus

3.3.1 The Magnet System

ATLAS main feature is an hybrid four superconducting magnet system, 26 m long and with a diameter of 22 m. The Magnet System (Figure 3.10) is

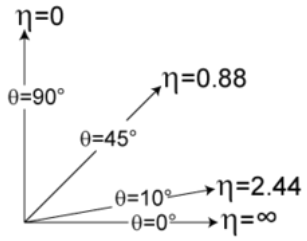

Figure 3.9: Pseudorapidity η as function of θ angle.

composed by:

- a central solenoid (CS), with its symmetry axis along beam direction, placed within the Inner Detector in the barrel region. It provides an uniform magnetic field of approximately 2 T along the z axis, it is 5.3 m long with a diameter of 2.4 m.
- a three superconducting toroid system (one central and one for each endcap). It provides a magnetic field whose peak intensities are 3.9 T in the central region of the detector and 4.1 T in the forward region. The aim of such a toroid is to have a large lever arm to improve the measurement of the muon transverse momentum, and it is built "in air" in order to minimize the muon multiple scattering within the detector.

3.3.2 The Inner Detector

The inner detector (ID) [40, 41] has been designed to allow a good pattern recognition, provide an optimal momentum resolution and primary and secondary vertex reconstruction for charged tracks with transverse momentum above 0.2 GeV. These purposes have been achieved through the use of 2 T solenoid magnet and an high granularity for position measurements. The ID layout consists in three complementary detectors (Figure 3.11). In the central part silicon pixel and silicon Semiconductor Tracker (SCT) detectors are installed.
Each track goes through three layers of pixel detectors and eight silicon strips, while in the outer part the Transition Radiation Tracker (TRT) can provide on average 30 and up to 36 hits per track. The two combined vertexing techniques allow to obtain an high precision both in ϕ and z. The inner detector is able to cover the $|\eta| < 2.5$ region.
The ID is the part of the ATLAS apparatus mostly exposed to radiation, thus a frequent maintenance is necessary to guarantee excellent performances.

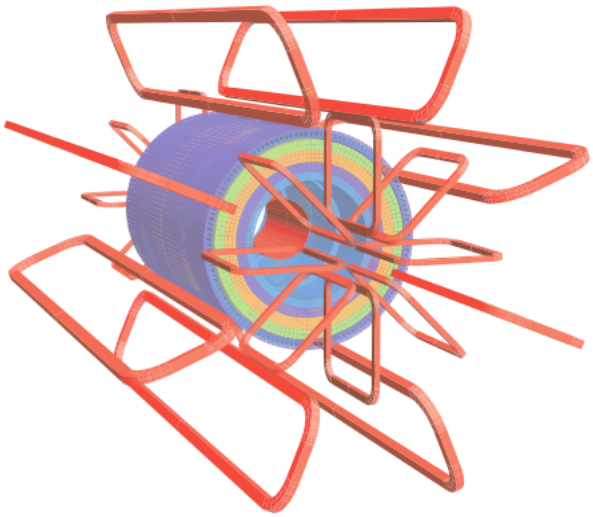

Figure 3.10: ATLAS magnets.

Pixel detectors

The purpose of pixel detectors is high precision measuring, impact parameter and vertex reconstruction. The system consists of three barrels at average radii of ∼4 cm, 10 cm, and 13 cm, and five disks on each side, between radii of 11 and 20 cm, which complete the angular coverage.

Spatial resolution (averaged on pseudorapidity distribution) are:

$$\begin{aligned} \sigma(R-\phi) &\simeq 12\ \mu m && \text{for all the pixels} \\ \sigma(z) &\simeq 66\ \mu m && \text{in the barrel region} \\ \sigma(R) &\simeq 77\ \mu m && \text{for the disks} \end{aligned}$$

Insertable B-Layer

The Insertable B-Layer (IBL) [42] is a fourth pixel layer that was installed during the long shutdown between Run-1 and Run-2. It adds protection against radiation of the pixel detector. The fourth module gives more robustness in tracking measurements improving tracking precision, thus allowing better impact parameter reconstruction for tracks and b-tagging performance. The IBL is placed at a radius of about 3.2 cm between the Pixel Detector and a new beam pipe with smaller radius.

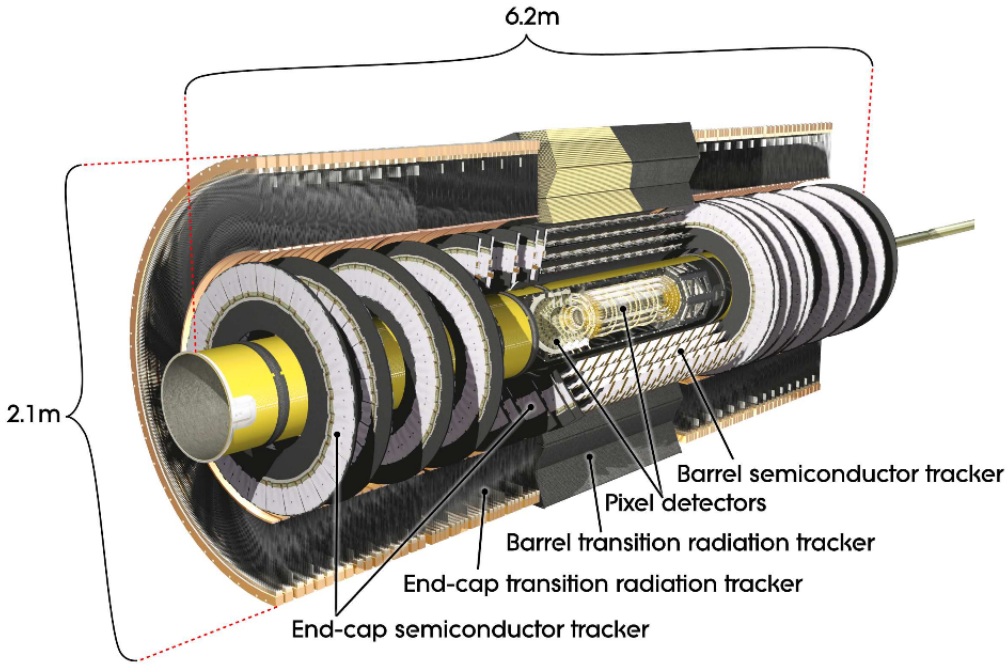

Figure 3.11: ATLAS inner detector.

Semiconductor tracker

The Semiconductor tracker (SCT) is placed in the intermediate radial range, and provides eight precision measurements per track, contributing to the measurements of impact parameter and vertex position, as well as providing good pattern recognition by the use of high granularity. In the barrel eight layers of silicon microstrip detectors are placed, providing with precision $R-\phi$ and z coordinates. The spatial resolution is 16 μm in $R-\phi$ e 580 μm in z. Tracks can be distinguished if separated by more than $\sim$ 200 μm.
Due to the highly radioactive ambient the SCT operate at low temperature regime (typically between -5 and -10 °C). The structures are equipped with systems that remove the heat generated by the electronics and the detector leakage current.

Transition radiation tracker

The Transition radiation tracker (TRT) is based on the use of straw detectors with small diameter (4mm), able to operate at very high rates expected during LHC collisions due to the sense wires within individual gas

volumes. The TRT operate with a non-flammable gas mixture of 70% Xe, 20% CO_2 e 10% CF_4. When charged particles pass through the detector they generate a transition radiation. The large number of straws employed guarantees a resolution of 50 μm at the LHC design luminosity, averaged over all straws and including a systematic error of ~ 30 μm from alignment. TRT arrangement is shown in Figure 3.13.

3.3.3 Calorimeters

ATLAS calorimeters (Figure 3.14) are placed between the inner detector and the muon spectrometer. They adopt a sampling technique where the active material layers alternate with layers of passive material (absorber). Particles interact in the the passive material thus producing an avalanche of particles (shower) detected in the active material and gradually loosing their energies, until a complete absorption in the medium. Different types of calorimeters are used to provide an excellent reconstruction for electromagnetic showers and to limit the hadronic particle flow that can reach the muon spectrometer. The ATLAS calorimeter system [43] is composed as:

- An electromagnetic (EM) calorimeter covering $|\eta| < 3.2$ region;
- An hadronic cylindrical (HC *Tile Barrel*) calorimeter covering $|\eta| < 1.7$ region;
- Two hadronic calorimeters in the endcap zone (HEC), covering $1.5 < |\eta| < 3.2$ region;
- Two forward calorimeters (FCAL), covering $3.2 < |\eta| < 4.9$ region;

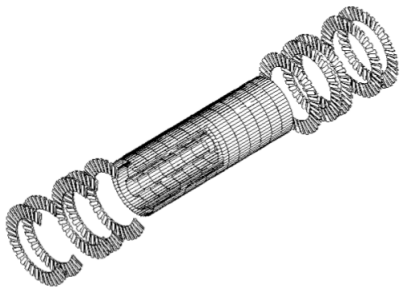

Figure 3.12: 3D view of pixel detectors.

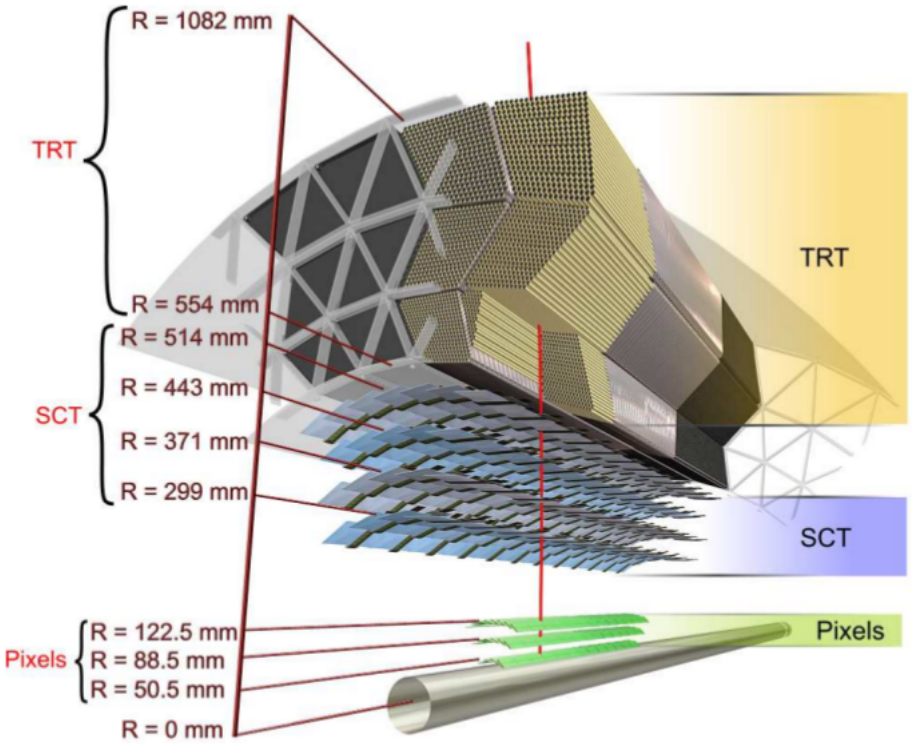

Figure 3.13: Placement of the three subdetectors in the ID.

The EM calorimeter is a lead/liquid-argon (LAr) detector with accordion geometry, it is preceded by a presampler detector, installed immediately behind the cryostat cold wall,and used to correct for the energy lost in the material.

The hadronic barrel calorimeter consists on plastic scintillator plates (tiles) embedded in an iron absorber. It is divided in three sections: a central barrel and two extended barrels. For the end-cap calorimeter LAr detector with parallel-plate geometry, and the forward calorimeter, a dense LAr calorimeter with rod-shaped electrodes in a tungsten matrix.

Electromagnetic calorimeter

The Electromagnetic calorimeter consists of a barrel part ($\eta| < 1.475$) and two end-cap zones ($1.375 < |\eta| < 3.2$). The barrel consists of two identical half-barrels while end-cap calorimeters have internal ($2.5 < |\eta| < 3.2$) and

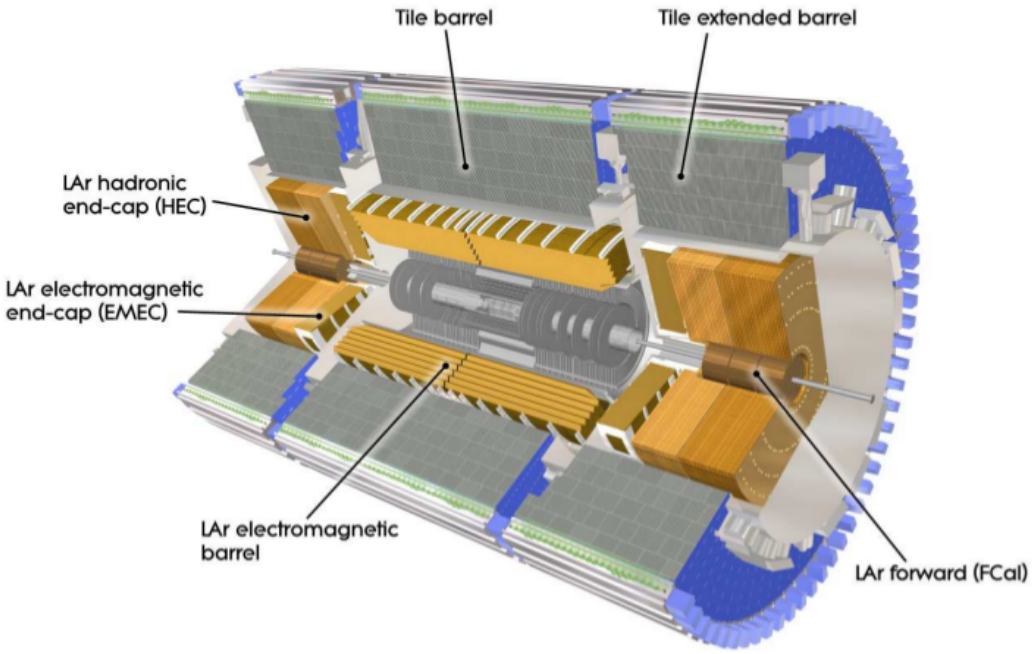

Figure 3.14: ATLAS calorimeter system.

external ($1.375 < |\eta| < 2.5$) wheel. The calorimeter is segmented in cells of variable dimensions as a function of η as well as its thickness.
The barrel calorimeter is divided into three layers, with different cell granularity. In the first layer the segmentation is $\Delta\eta \times \Delta\phi = 0.0031 \times 0.098$ for a 4.3 X_0 thickness, mainly used to distinguish photons from $\pi_0 \to \gamma\gamma$ and electrons from $\pi\pm$, its fine granularity in η of this layer is used to determine the pseudo-rapidity of the particle. The second layer is segmented in $\Delta\eta \times \Delta\phi = 0.025 \times 0.025$ cells providing a radiation length of 16 X_0 allowing to contain the largest energy fraction of the shower. The third later, specifically dedicated to high energy electrons and photons, has a segmentation corresponding to $\Delta\eta \times \Delta\phi = 0.05 \times 0.0245$.
The total readout channels are 190000.

Hadronic calorimeter

ATLAS Hadronic calorimeters cover the $|\eta| < 4.9$ range by adopting different optimized techniques. Thickness, as mentioned before, is one of the main feature of hadronic calorimeters, being able to absorb jets produced by the hadronization of quarks and gluons and reduce the number of particle

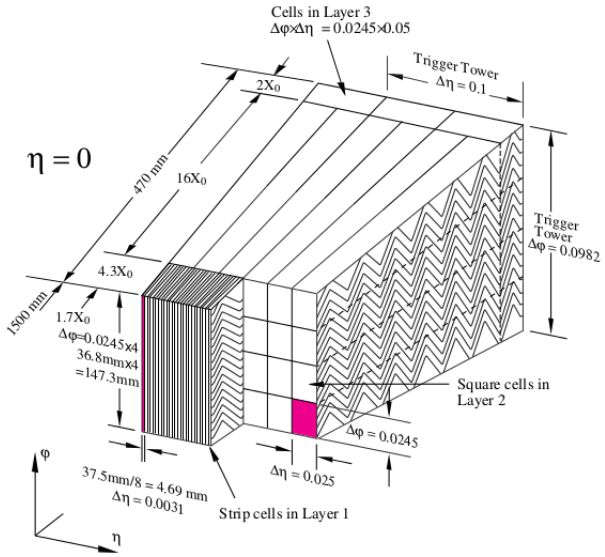

Figure 3.15: Electromagnetic caloremeter structure.

arriving to muon spectrometer.

Tile Calorimeter: it's a sampling calorimeter usign iron as absorber material and tiles of scintillating material as active medium. It is placed in the $|\eta| < 1.7$ region, with a $(\Delta\eta \times \Delta\phi \simeq 0.1 \times 0.1)$ granularity, its thickness offers about 10 interactions lengths λ at $\eta = 0$.

Hadronic end-cap calorimeter (HEC) : this calorimeter is equipped with LAr scintillating material and coppier plates as absorber. It covers a $1.5 < |\eta| < 3.2$ with a granularity of $(\Delta\eta \times \Delta\phi \simeq 0.1 \times 0.1)$.

Forward calorimeter (FCAL): this calorimeter has a complex design, due to the high radiation flux. It has a distance from the interaction point of 4.7 m, covering a pseudorapidity range of $3.1 < |\eta| < 4.9$. It consists of three modules per side: FCAL1, FCAL2, FCAL3 all equipped with LAr as active material. The first module, having copper as absorber, has been designed for electromagnetic calorimeter measurements while FCAL2 and FCAL3 are hadronic calorimeter using tungsten as absorber.

Performances of calorimeters

For the EM calorimeter the energy resolution can be obtained by summing in quadrature (denoted as $\oplus$) the independent terms:

$$\frac{\sigma_E}{E} = \frac{a}{\sqrt{E}} \oplus \frac{b}{E} \oplus c, \tag{3.11}$$

where a is the sampling term (which includes statistical fluctuation), b is the noise term and c a constant term. The expected resolution is :

$$\frac{\sigma_E}{E} = \frac{10\%}{\sqrt{E}} \oplus 10\% \tag{3.12}$$

between 2 GeV and 5 TeV. The angular resolution expected is 40 $mrad/\sqrt{E(GeV)}$.

For hadronic calorimeters:

$$\frac{\sigma_E}{E} = \sqrt{\frac{c_{int}^2 + c_{camp}^2}{E}} \oplus a \tag{3.13}$$

where a is a term that describes the non-gaussian fluctuations of electromagnetic showers, c_{int} represents gaussian fluctuation of the initial energy and c_{camp} refers to statistical and sampling fluctuations. The expected energy resolution are:

$$\begin{aligned} \frac{\sigma_E}{E} &= \frac{50\%}{\sqrt{E(GeV)}} \oplus 3\% \qquad \text{for } |\eta| < 3.0 \\ \frac{\sigma_E}{E} &= \frac{100\%}{\sqrt{E(GeV)}} \oplus 10\% \qquad \text{for } 3.0 < |\eta| < 4.9. \end{aligned} \tag{3.14}$$

3.3.4 Muon spectrometer

The muon spectrometer (MS) [44] constitutes the outer part of the ATLAS apparatus. It has been designed to detect and measure charged particles coming from the central barrel and from end-caps in the $|\eta| < 2.7$ region, allowing muon identification with energy ranging from 3 GeV (lower energy muon are absorbed in the hadronic calorimeter) to 1 TeV. It also provides a trigger system in the $|\eta| < 2.4$ region. MS adopts three different magnet systems (one in the barrel and two in the end-caps). It consists of three parts:

- large superconducting air-core toroid magnets to bend charged tracks along η coordinate;

Detector	η	Number of chambers	Number of channels	Employment
MDT	$\|\eta\| < 2.7$ (internal layer $\|\eta\| < 2.0$)	1088 (1150)	339000 (354000)	High precision tracking
CSC	$2.0 < \|\eta\| < 2.7$	32	31000 (354000)	High precision trcking
RPC	$\|\eta\| < 1.05$	544 (606)	359000 (373000)	Trigger, second coordinate
TGC	$1.05 < \|\eta\| < 2.7$ (2.4 for trigger)	3588	318000	Trigger, second coordinate

Table 3.1: Main parameters of muon spectrometer subdetectors.

- high precision tracking chambers: Monitored Drift Tubes (MDT) in the barrel and Cathode Strip Chambers (CSC) in the end-caps;
- a trigger system composed of Resistive Plate Chamber (RPC) and Thin Gap Chambers (TGC).

The main MS component parameters are listed in Table 3.1. To have better MS performances several considerations have been taken into account:

- resolutions in barrel and end-caps regions are different. For a given p_T, momentum increases as function of η, while bending does not with the same rapidity. This leads to a η depending granularity in end-cap regions.
- Radiation flux in end cap regions are ten times greater than in the barrel, readout electronics should be more permissive to radiations.
- Some magnetic field inhomogeneities in the transition region requires good trigger strategies in order to reject fake events.
- A bunch crossing identification is required in order to have a time resolution better than the LHC bunch spacing.

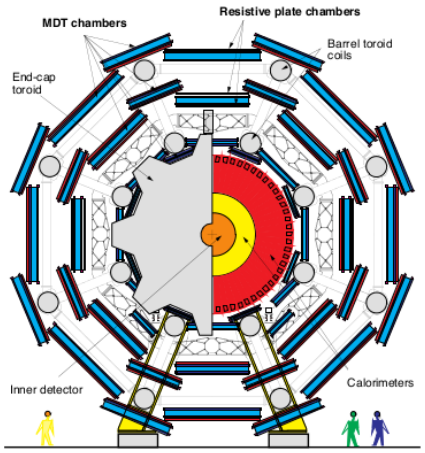

Figure 3.16: Schematic view of the transversal section of the muon spectrometer.

- A trigger with well-defined p_T cut-offs in moderate magnetic fields, requiring a granularity of the order of 1 cm.
- ϕ measurement with a spatial resolution of $5 - 10$ mm for offline reconstruction.

The MS layout is show in Figures 3.16 and 3.17.

Magnets

The toroidal magnetic fields are provided by superconducting air-core coils. The magnetic field resulting is orthogonal to muon trajectory with minimised resolution losses due to multiple scattering. Each toroid has eight concentric coils, symmetric with respect to the beam direction. The finite number of coils leads to a non complete toroidal magnetic configuration, solved by combining contribution from end-cap and barrel magnetic fields.

Precision chambers

The precision chambers used in the MS system are MDT and CSC. MDT chambers provide a precise muon momentum measurement in $|\eta| < 2.0$ range. They are mainly composed by aluminium drift tubes (Figure 3.18) with a diameter of ~ 30 mm. Each drift-tube consists of a central Tungsten-Rhenium wire of 50 μm and is filled with a mixture of Ar/CO_2 (93/7). Muon passing drift-tubes ionize the gas, causing an avalanche of electrons drifting

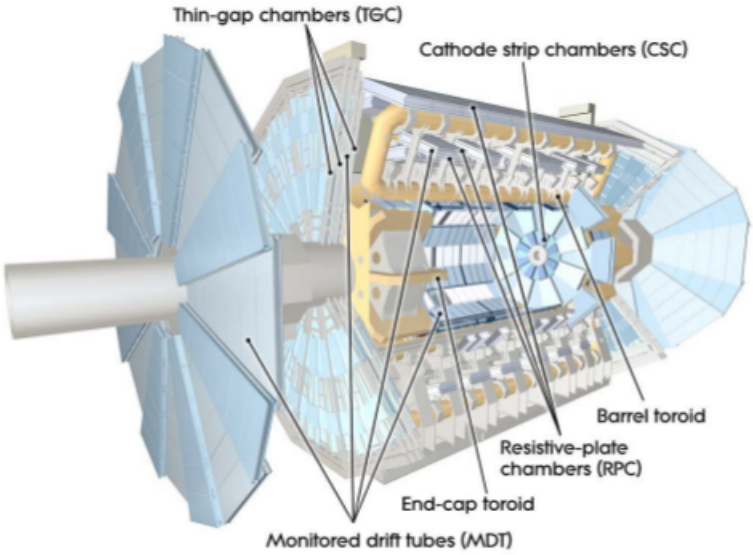

Figure 3.17: Muon spectrometer layout and subdetectors placement.

to the central wire; once hit has been read and the time of arrival has been recorded, the distance of the muon track from the wire can be obtained, providing a single spatial resolution of 80 μm per single wire.
CSC chambers are multi-wire proportional chambers. They replace the MDTs in the η region from 2.0 to 2.7, where the high counting rates expected (> 200 Hz/cm^2) make them not efficient in this area. CSC are designed with a symmetrical cell filled with an argon–carbon dioxide mixture, where the anode-cathode spacing is equal to the anode wire pitch. The track position is obtained by measuring the charge induced on the cathode by the avalanche created on the anode. Electron drift time is less than 25 ns, while spatial resolution achieved is 50 μm. Figure 3.20 shows CSC design.

Trigger chambers

Trigger chambers operating in the MS are RPC and TGC.
RPC chambers are gas detectors composed by two parallel bakelite plates separated by an insulating spacer resulting in a 2mm gap, filled with a non-flammable gas mixture of tetrafluoroethane ($C_2H_2F_4$), isobutane ($(CH_3)_3CH$) and sulfur hexafluoride (SF_6) respectively with a percentage of 96.7%, 3.0% and 0.3% under an electric field of typically 4.5kV/mm. Electron avalanches

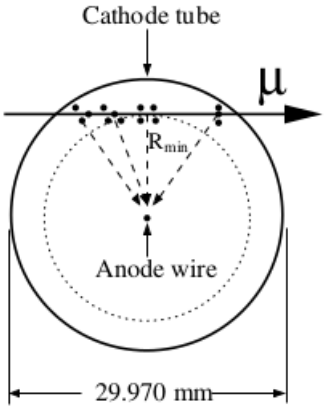

Figure 3.18: MDT section.

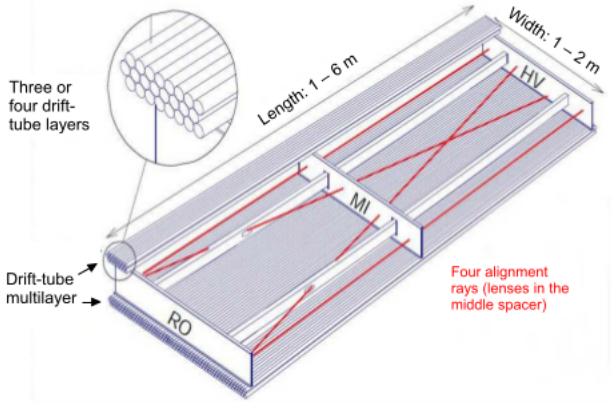

Figure 3.19: MDT mechanical structure.

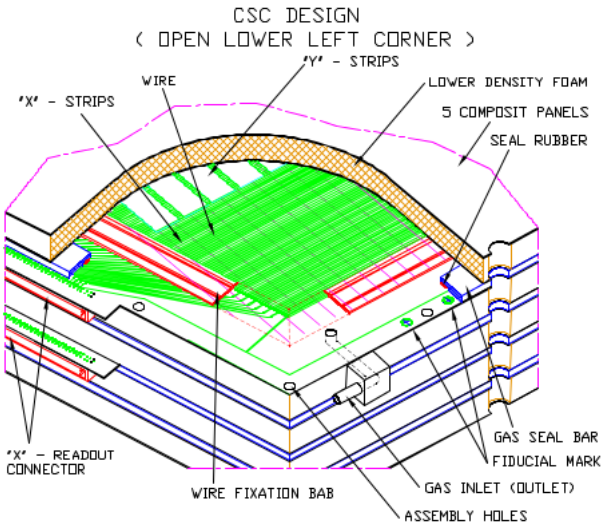

Figure 3.20: CSC structure.

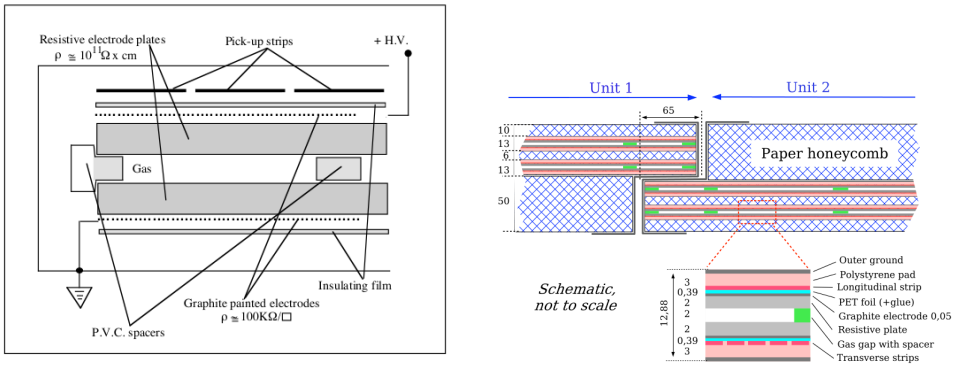

(a) *Schema di funzionamento di una RPC a singola gap.* **(b)** *Sovrapposizione delle camere lungo z.*

Figure 3.21: RPC chamber in the muon spectrometer.

creating after muons ionizes gas produce a signal which is read out via two metal strips placed at both side of the chamber and orthogonal each other, providing a two dimensional coordinate measurement with a spatial resolution of 5-10 mm. The strips are arranged to be parallel (η coordinate) and orthogonal (ϕ coordinate) to the MDT wires.
In the end-cap trigger chambers adopted are TGC, which are multi–wire proportional chambers, but unlike CSC the anode-cathode separation is smaller (1.4 mm), thus resulting in an improved time resolution. They operate in a gas mixture of CO_2 and $n - C_5H_{12}$ (55% and 45% respectively). The anode wires are parallel to the MDT wires, and provide the trigger information together with read-out strips orthogonal to the wires. Time resolution achieved is 5 ns.

3.3.5 External detectors

Three small detectors are placed in the outer part of ATLAS:

- LUCID (**LU**minosity measurement using **C**erenkov **I**ntegrating **D**etector) is a Cherenkov detector placed at a distance of ±17 m from the interaction point. It monitors luminosity and beam condition and measure inelastic pp scattering;
- ZDC (**Z**ero-**D**egree **C**alorimeter) with the purpose of detecting neutrons from heavy ions collisions;
- ALFA (**A**bsolute **L**uminosity **F**or **A**TLAS) placed at ±240 m from the interaction point, it measures the absolute luminosity.

3.4 The ATLAS Trigger System

A very challenging effort for LHC experiments is the online event selection, which requires an efficient trigger system to reduce the high rate of events generated during collisions corresponding to 40 MHz. The current technology allows to record data at about 200 Hz: it is evident that the trigger system needs to be optimized in order to reduce the event rate by a factor of $10^6 - 10^7$ preserving at the same time the interesting events (Figure 3.22).

ATLAS Trigger system [45] has been initially designed with three different

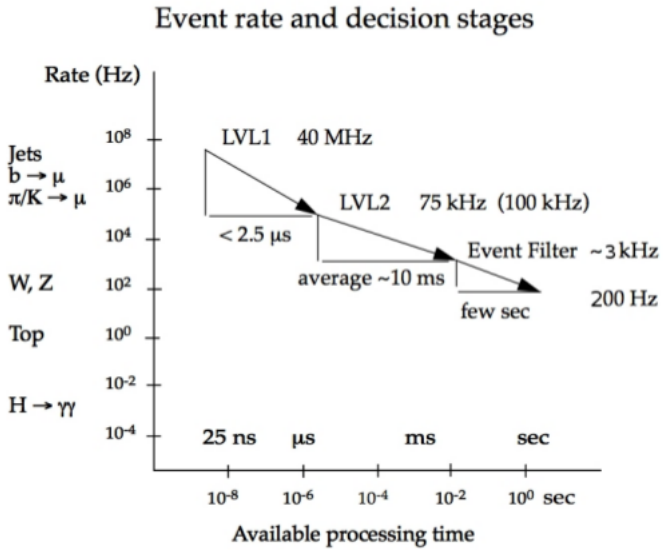

Figure 3.22: Event rate at LHC.

levels of event selection: Level 1 (L1), Level 2 (L2) and Event Filter (EF). In each level a more stringent selection criteria are applied. Figure (3.23) shows ATLAS trigger organization. In Run-2 ATLAS adopted a two-level trigger system [46] consisting in Level 1 Trigger and High Level Trigger (HLT).

A recorded event has to be accepted at least from one of the triggers composing the *trigger menu* and then shared according the trigger that passed. In regime of high luminosity triggers can be *prescaled*: the prescale factor f_{ps} defines the number of the interesting events discarded, i.e. a prescale factor of 5 means that only one of the 5 events will be recorded. Most of the analyses use unprescaled trigger $f_{ps} = 1$ for their selections.

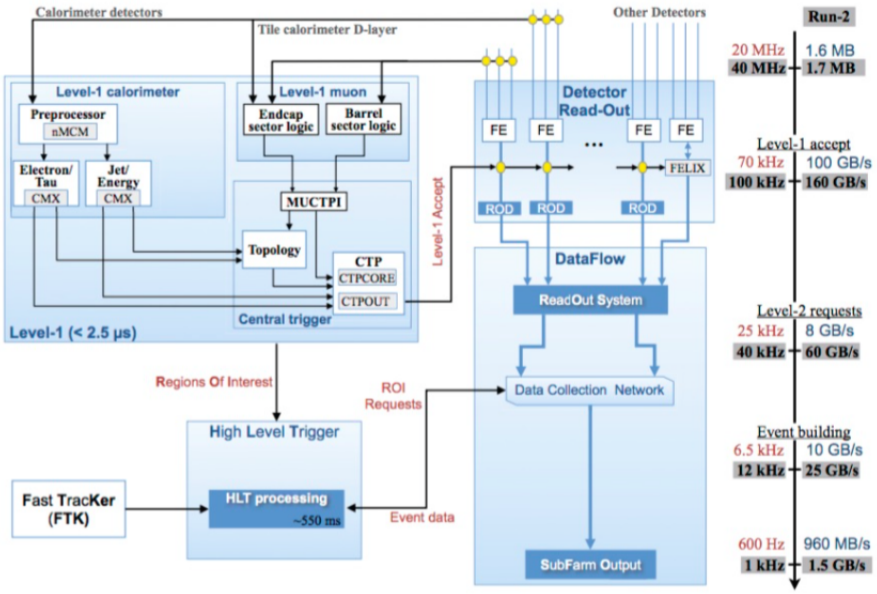

Figure 3.23: ATLAS trigger scheme.

3.4.1 L1 trigger

The first level trigger has been designed to reduce the initial rate of event from 1 GHz to 75 kHz, by selecting events in less than 2.5 μs. A first selection is applied on the basis of information collected by the muon spectrometer and calorimeters.
L1 trigger searches for events with high transverse momentum, electron, photons, jets, hadronic-decaying τ leptons, large missing transverse energy. High momentum muons are identified by using trigger chambers in the end-cap and barrel regions of the spectrometer.
For each event a *Region of Interest* (RoI) is defined, in η and ϕ coordinate. RoI data include information on the event, used by higher level triggers.
L1 calorimeter trigger level (L1Calo) is composed by 7000 trigger towers (TT) (0.1×0.1 in $\Delta\eta \times \Delta\phi$, but granularity increases for greater $|\eta|$) placed in the two calorimeters. The trigger algorithm (Figure 3.24) computes the transverse energy of electromagnetic clusters with a precision of 1 GeV. When a relevant amount of energy is detected in a 2×2 cluster three requirements must be satisfied to consider hte cluster as a seed to be propagated to the next level: a threshold on the transverse energy and electromagnetic and hadronic isolation.

Muon L1 trigger uses RPC in the barrel and TGC in the end-caps. In

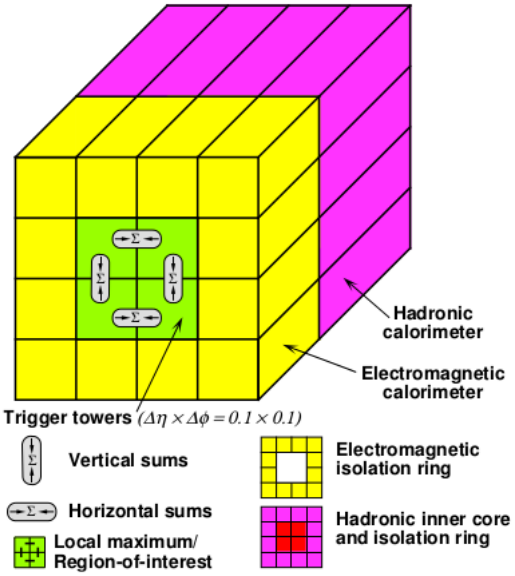

Figure 3.24: Calorimeter trigger scheme algorithm.

both regions three stations perform the tracking measurements. The trigger algorithm starts from the hit on the central station to find a coincidence in the remaining stations. Once the hit is found the RoI is propagated to the next level.

3.4.2 HLT Trigger

In Run-2 Level 2 Trigger and Event Filter have been merged in a single farm, the High Level Trigger [**?**]. This new farm has the advantage of simplicity, since allows a code reduction and an algorithm duplication. During the shutdown, HLT selection have been optimized in order to reduce differences between offline and online selections, minimizing the trigger inefficiencies by a factor two. The final event rate is $\sim$ 1 kHz.

Chapter 4

Physiscs Objects Reconstruction in ATLAS

The events selected by trigger algorithms are recorded for the offline analyses. They are processed by identification and reconstruction algorithms in order to build physics objects, providing a set of physics objects that can be used in physics analyses.

4.1 Muon reconstruction

Muons pass through calorimeters and reach spectrometer with a large fraction of their initial energies. This feature is used to detect and identify them in muon chambers. All information from the sub-detectors are exploited, and different types of muon can be defined according the sub-detectors used in the reconstruction [47]:

- **"Combined" (CB) Muons** whose tracks are separately reconstructed in the spectrometer and in the inner detector and then matched together. Track matching is realized by a combination algorithm that uses χ^2 minimization. Combined measurement improves momentum resolution, allowing rejection of muons coming from kaons and pions decays.
- **"Segment tagged" (ST) Muons** are muons with low p_{T} who reach the firs layer of the spectrometer. Tracking is performed combining inner detector information and the partial information of the spectrometer.
- **"Calorimeter-tagged" (CaloTag) Muons** whose ID tracks are extrapolated to calorimeters and matched with energy deposits. CaloTag muons are mainly used to increase efficiency in the region not covered by the spectrometer ($\eta \sim 0$).

- **"Extrapolated" (ME) Muons** whose reconstruction is performed only in spectrometer. Extrapolated muons are mainly used to extend the acceptance for muon reconstruction in the region not covered by the interaction point, corresponding to $2.5 < |\eta| < 2.7$.

Muon identification is performed through the application of quality criteria to suppress background muons (mainly from pion and kaon decays), and select signal (*prompt*) muons by using discriminating variables. There are four muon identification selections: *Medium*, *Loose*, *Tight* and *High-*p_T.
Medium muons include CB and ME muons with hits requirements in the MDT layers for CB muons and in the MDT/CSC layers for ME. The matching between the inner detector and the muon spectrometer must satisfy a loose criteria in order to suppress the contamination due to hadrons mis-identified as muons.
Loose muons are mainly used to reconstruct Higgs boson candidates, selecting all muon types. In the $|\eta| < 2.5$ region about 97.5% of the Loose muons are combined muons, approximately 1.5% are CT and the remaining 1% are reconstructed as ST muons.
Tight muons selects the purest sample of muons, with only CB muons populating the sample. **High $p_{\mathbf{T}}$ muons** are defined in order to maximise the momentum resolution for muons with $p_{\mathrm{T}} > 100$ GeV. They are CB muons passing the Medium selection and satisfying requirements on the number of hits in the spectrometer layers. These requirements improves p_{T} resolution of 30% for muons above 1.5 TeV.

Reconstruction efficiency

The reconstruction efficiency for muons follow two steps adopting a tag and probe procedure. In the first the efficiency $\epsilon(X|CT)$ of reconstructing muons assuming a reconstructed track in the inner detector is measured, using CaloTag as muon probe. Then, in the second step, the efficiency is corrected by the efficiency $\epsilon(ID|MS)$ of the inner detector track:

$$\epsilon(Type) = \epsilon(Type|ID) \cdot \epsilon(ID) \qquad \text{where Type=Medium, Tight, High } p_{\mathrm{T}} \tag{4.1}$$

Scale factor (SF) measures the level of agreement of the efficiency measured from data ϵ^{Data} and from expected MC simulation ϵ^{MC}:

$$SF = \frac{\epsilon^{Dati}}{\epsilon^{MC}}. \tag{4.2}$$

The tag and probe method uses $Z(\mu\mu) + \text{jets}$ decays. Figure 4.1 shows the muon reconstruction efficiency as function of η for the different muon selection.

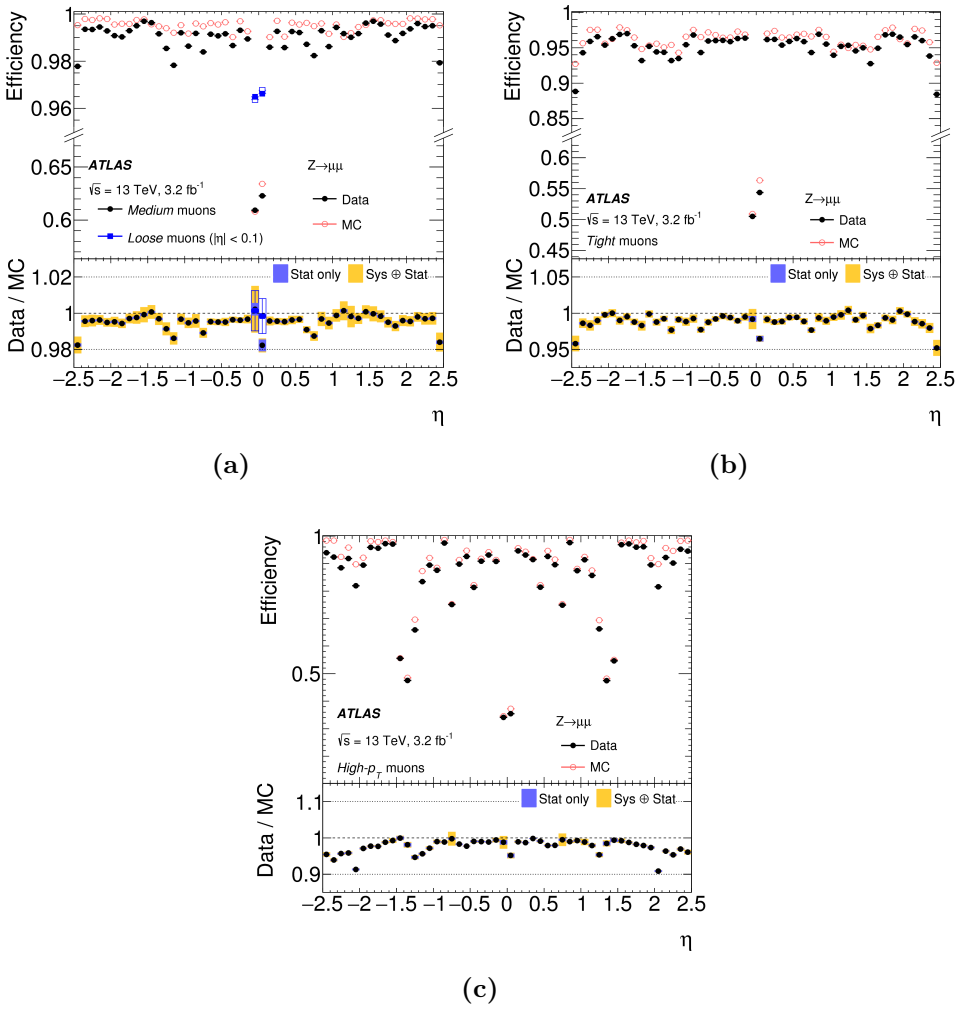

Figure 4.1: Muon reconstruction efficiency as function of η for Medium (a), Tight (b) and High-p_{T} (c) measured in $Z(\mu\mu)+\mathrm{jets}$ events [47].

The efficiencies for Loose, Medium and Tight muons are above 90%, while for High-p_{T} muons the lower values are mainly due to the tight requirement on momentum resolution.

Muon isolation

To reject muons from hadronic decays isolation criteria are applied in order to select muons originating from W,Z decays. Two variables are defined:

- a track isolation variable, $p_{\mathrm{T}}^{\mathrm{varcone30}}$, defined as the sum of the transverse momenta of all tracks within a cone size of $\Delta R = \min(10\ \mathrm{GeV}/p_{\mathrm{T}}\,, 0.3)$

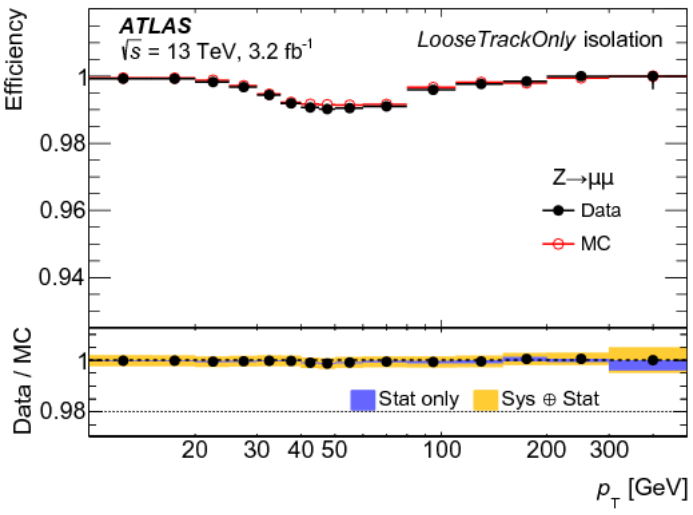

Figure 4.2: Isolation efficiency for *LooseTrackOnly* muons as a function of muon p_{T} [47].

around the track associated to the muon candidate and originating from the reconstructed primary vertex of the hard collision, excluding the muon associated tracks.

- a calorimeter isolation variable, $E_{\mathrm{T}}^{\mathrm{topocone20}}$, defined as the sum of the energies of topological clusters within a cone of $\Delta R = 0.2$ around the candidate electron cluster.

Seven isolation working points are then defined as function of the ratio between the track or calorimeter isolation variable and the transverse momentum of the muon. In Figure 4.2 the isolation efficiency for the *LooseTrackOnly* working point is reported. This working point is defined as $p_{\mathrm{T}}^{\mathrm{varcone30}}/p_{\mathrm{T}}$ with a 99% efficiency constant in η and p_{T} .

4.2 Electron reconstruction

Electron reconstruction uses calorimeter and inner detector information. The algorithm has been designed to provide an high efficiency electron reconstruction on a wide p_T and η range, maximizing jets rejection.
The reconstruction algorithm [48] relies on a clustering procedure in EM calorimeter to which a track in the ID is associated.

Reconstruction in the central region In the central region ($|\eta| < 2.47$) seed clusters must have energies above 2.5 GeV in a window size of 3×5 in $\Delta\eta\Delta\phi$ (0.025×0.025). Seed clusters are then matched to track candidates from the ID using the distance (η, ϕ). Several tracks can be matched to the same seed cluster (as in the case of electromagnetic showers). If this condition occurs tracks are ordered according the minimum difference $\Delta R = \sqrt{\Delta\eta^2 + \Delta\phi^2}$ between ID and seed cluster (η, ϕ) coordinate.
Starting from the seed cluster electron objects are constructed by clustering cells in all four layers of the EM calorimeter. The size of the clustering corresponds to $\Delta\eta\Delta\phi$ equals to 3×7 (5×5) in the central region (in the end-caps). Finally the four-momentum of central electron is computing using information from both the primary track and the EM cluster. Electron candidates without any track associated are considered as photons.

Reconstruction in the forward region In the forward region, with $2.5 < |\eta| < 4.9$, no tracking information is available. Electron candidates are reconstructed from energy deposit in the EM calorimeter with a procedure that takes into account the significance of the interested cells with respect to the expected noise. An electron candidate must have a transverse energy of $E_T > 5\ GeV$ and small hadronic energy component. The barycentre of the cluster defines the electron direction and its energy is computed by summing the energies in the cluster cells.

Electron identification

Electron identification [49] is performed through algorithms that use information from calorimeters and inner detector. The selection criteria applied define a set of quality conditions for the electrons (called *menu*). Three different level of identification are defined: *Loose*, *Medium* and *Tight*; reported here in increasing background rejection. As consequence, Tight electron selection contains the Medium one, which in turn contains Loose selection. The tighter the operating point the purer is the electron sample selected and the lower its identification efficiency.
The identification algorithms exploit the information of the electron cluster and track measurement. A multivariate (MVA) that simultaneously evaluates several properties of the electron candidates is built and used in a likelihood-based (LH) method. The LH method uses the signal and background probability density functions (PDFs) of the discriminating variables and assigns a given probability for the candidate object to be a signal electron or background.

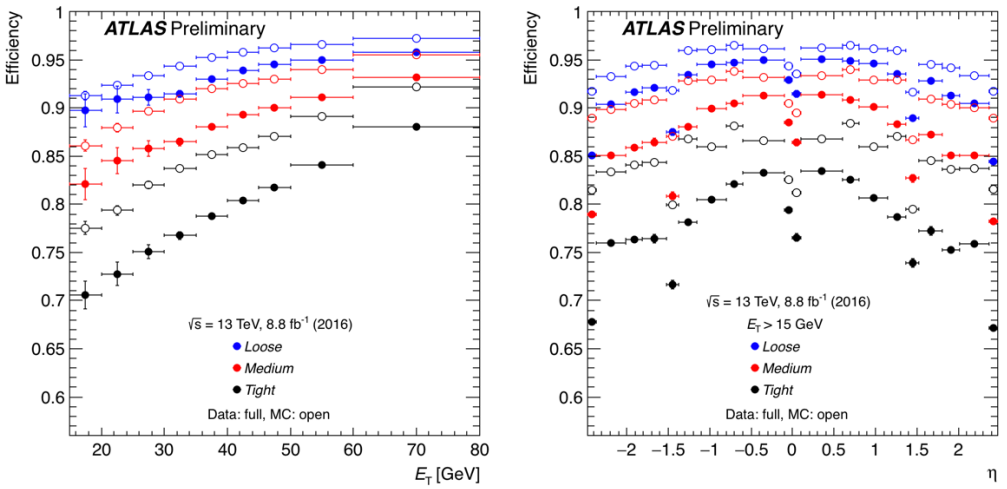

(a) **(b)**

Figure 4.3: Electron identification efficiencies as function of $E_{\mathrm{T}}^{\mathrm{miss}}$ (a) and η (b) in $Z(ee)+$ jets events for Loose (blue), Medium (red) and Tight (black) electrons [50].

Finally for high energy electrons, which deposit small fractions of their energies in in the first layers of the EM calorimeter and more in the hadronic calorimeter a different definition of Tight electrons (which show inefficiencies) is applied. For electron candidates with E_T above 125 GeV, Tight electrons have the same definition as Medium one with the supplement of rectangular cuts on some discriminating variables.

Electron identification efficiency

The distribution of electron shower depends on the pseudorapidity of the electron candidates and on their energies. For this reason the identification operating points were optimised in η and E_T bins. Figure4.3 shows the performance of the LH algorithm. $Z(ee)+$ jets events are selected using 8.8 fb^{-1} of data recorded at $\sqrt{s}=13$ TeV and MC simulations.

Electron isolation

Electron isolation is performed to select *prompt* electrons useful for the analysis from *non-prompt* electrons originating from converted photons, electrons from heavy flavour hadron decays, and light hadrons mis-identified as electrons. Isolation discriminating variables used are:

	Efficiency		
Operating point	Calorimeter isolation	Track isolation	Total efficiency
LooseTrackOnly	-	99%	99%
Loose	99%	99%	$\sim 98\%$
Tight	96%	99%	$\sim 95\%$
Gradient	$0.1143\% \times E_{\mathrm{T}} + 92.14\%$	$0.1143\% \times E_{\mathrm{T}} + 92.14\%$	90/99% at 25/60 GeV
GradientLoose	$0.057\% \times E_{\mathrm{T}} + 95.57\%$	$0.057\% \times E_{\mathrm{T}} + 95.57\%$	95/99% at 25/60 GeV

Table 4.1: Electron isolation operating point definitions. The calorimeter and track isolation refer to the selection based on $E_{\mathrm{T}}^{\mathrm{cone}\ 0.2}$and $p_{\mathrm{T}}^{\mathrm{cone}\ 0.2}$ [49].

- a track isolation variable, $p_{\mathrm{T}}^{\mathrm{cone\ R}}$, defined as the sum of the transverse momenta of all tracks within a cone size of $\Delta R = \min(R, 10\ \mathrm{GeV}/E_{\mathrm{T}})$ around the track associated to the electron candidate and originating from the reconstructed primary vertex of the hard collision, excluding the electron associated tracks.

- a calorimeter isolation variable, $E_{\mathrm{T}}^{\mathrm{cone\ R}}$, defined as the sum of the energies of topological clusters within a cone of $\Delta R =$ R around the candidate electron cluster.

Table 4.1 reports all the electron isolation operating point definitions.

4.3 Jet reconstruction

Due to color confinement partons can't exist in free form but they hadronize. The particles produced in this process can be narrowed to a cone of given dimension and constituting a jet. Jet properties (and consequently original quark or gluon properties) can be determined according the algorithm used in reconstruction.
In ATLAS jets are reconstructed from an algorithm which has as starting point the analysis of energies deposited in the calorimeters from hadronic and electromagnetic showers (called *topological clusters*). Jet four-momenta is assigned from energies and angles with respect to the interaction vertex. Jet energy calibration considers several aspects:

1. Non compensation of the calorimeter due to a partial measurement of hadron energies.

2. Energy losses in region of detector constituted by passive materials.

3. Energy losses of particles outcoming calorimeter.

4. Energy deposits of particles belonging to the jet but non included in the reconstructed jet.

Jet reconstruction starts from topological cluster, corresponding to a combination of calorimeter cells that follow shower developing. The algorithm identifies a seed cell that has a signal-to-noise ratio greater than 4. The noise is defined as ratio of the energy deposited in the calorimeter cell over the RMS of the energy distribution in events triggered at random bunch crossing. Neighbouring cells around seed with a signal-to-noise ratio greater than 2 are included and finally added to form the topological cluster with final energy corresponding to the sum of the energies of all cells included

The anti $-$ $\mathbf{k_T}$ algorithm

The $anti - k_T$ [51] clustering algorithm is the procedure applied for jet reconstruction.

The algorithm is based on the definition of distance d_{ij} between two objects i and j and the distance d_{iB} between the $i - th$ objects and the beam (B). Clustering procedure selects the smallest distance, if this condition is satisfied by d_{ij} the objects i and j are combined (the four-momenta are summed), otherwise if d_{iB} matches the requirements i is considered as jet and removed from the list. The iteration procedure ends when all object list is completed. The distance definitions are:

$$d_{ij} = min\left(k_{T_i}^{2p}, k_{T_j}^{2p}\right)\frac{\Delta_{ij}}{R^2} \tag{4.3}$$

$$d_{iB} = k_{T_i}^{2p} \tag{4.4}$$

where $\Delta_{ij} = (y_i - y_j)^2 + (\phi_i - \phi_j)^2$ ans k_{T_i}, y_i and ϕ_i are respectively the transverse momentum, the rapidity and the azimuthal angle of the particle i. The power parameter p is a feature of the algorithm: $p = 1$ for k_T algorithm. For $p = -1$ the distance is

$$d_{ij} = min\left(\frac{1}{k_{T_i}^{2p}}, \frac{1}{k_{T_j}^{2p}}\right)\frac{\Delta_{ij}}{R^2}$$

completely dominated by the particle with the greatest transverse momentum, hence soft particles will cluster with this particle. In this way a jet is defined around the particle with the highest k_T, which includes all the soft particles within a circle of radius R. If two hard particles are present and close each

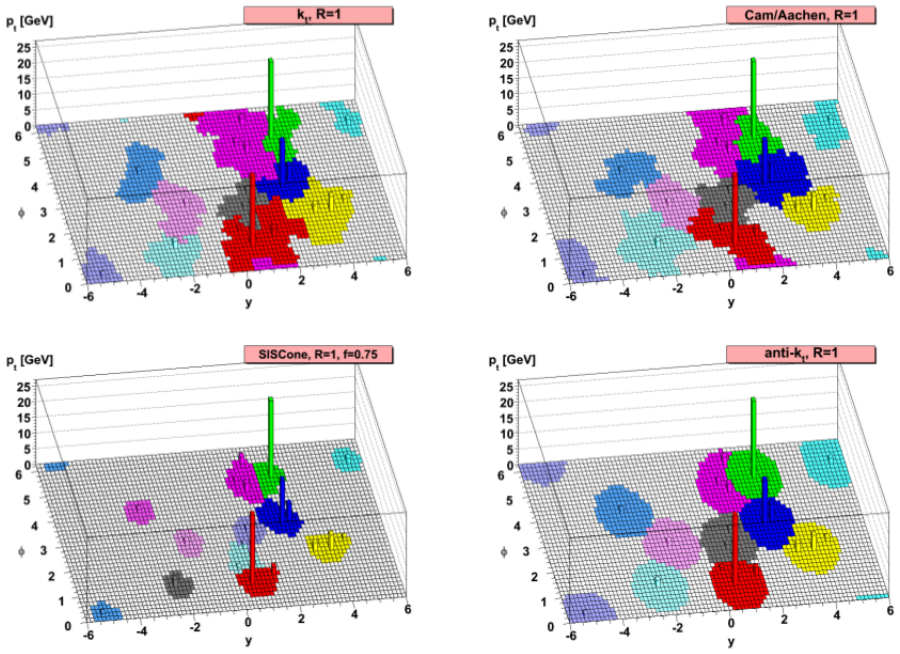

Figure 4.4: Shape output of the different reconstruction jet algorithms for the same event. $anti-k_T$ algorithm is on right bottom.

other, the overlapping region is assigned to the *hardest* particle. Soft particles don't change the shape of the jet: jet boundary is not dependent from soft radiation (*soft-resilient*) but only from the hard one.

Pile-up suppression

The suppression of pile-up jets has been developed with the definition of a jet-vertex tagging technique, JVT [52]. This algorithm combines both calorimeter and tracking information in a two-dimensional discriminant. The variables used in the discriminant definition are Jet Vertex Fraction and R_{pT} which contribute to separate hard-scatter (HS) events from pile-up events:

- Jet Vertex Fraction (JVF), is defined as the scalar transverse momentum sum of the tracks that are associated with the jet and originate from the hard-scatter vertex divided by the scalar p_{T} sum of all associated tracks. This quantity is then corrected by including a term which takes into account the scalar p_{T} sum of the tracks originating from pile-up interactions.

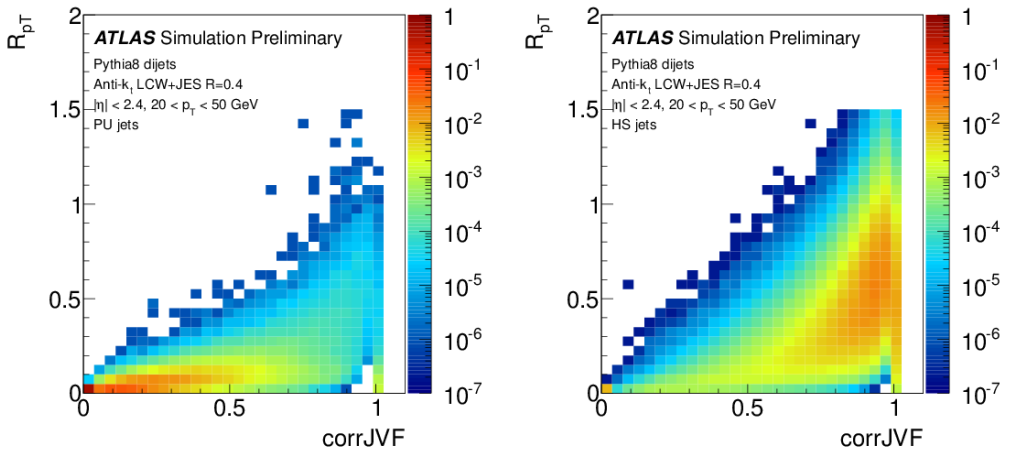

(a) **(b)**

Figure 4.5: 2-dimensional correlation of JVT and R_{pT} for pile-up (left) and hard scatter (right) jets [52].

- R_{pT} is defined as the the scalar p_{T} sum of the tracks that are associated with the jet and originate from the hard-scatter vertex divided by the fully calibrated jet p_{T} , which includes pileup subtraction.

The correlation plots in Figure 4.5 show that pile-up jets are expected to have low values of both variables, while HS jets are characterized by large values of JVT and R_{pT}.

Jet calibration

Reconstructed jets do not have energies corresponding to the initial one. A calibration is hence needed in order to assign the correct value of the energy. A jet energy scale (JES) calibration is applied in order to correct the values of measured energy, which takes into account several effects: calorimeter non compensations, energy losses due to passive materials in the detector, leaking due to showers outgoing calorimeters, pile-up jets and signal losses in the calorimeter clustering. The method relates the energy measured by the calorimeters to the true jet energy by considering the mean of the jet response distribution ($\mathrm{E_{reco}/E_{truth}}$) in p_{T} and η bins. The calibration follows four steps, as described in details in [53].
The width of jet energy distribution provides the jet energy resolution (JER) term. JER can be measured studying the asymmetry observed between the jet p_{T} in the same pseudorapidity region (in order to minimize detector

effects). The jet energy resolution is obtained in $p_{\mathrm{T}} \times \eta$ bins. The JER can be parametrised as follows [54]:

$$\frac{\sigma_{p_{\mathrm{T}}}}{p_{\mathrm{T}}} = \frac{N}{p_{\mathrm{T}}} \oplus \frac{S}{\sqrt{p_{\mathrm{T}}}} \oplus C \tag{4.5}$$

Where N, S, and C are the noise, stochastic and constant terms respectively. Equation 4.5 shows that JER becomes less significant for high jet energies.

4.4 b-tagging

The b-tagging identification is crucial in top quark reconstruction and in b-tagged analyses. In Run-2 the fourth pixel layer installed in ATLAS, the insertable B-layer (IBL) provides a better track and vertex reconstruction performances. Also b-tagging algorithms have been revisited, thus leading to an improvement in the low and medium jet p_{T} region.
The b-tagging algorithms [55, 56] use track information of charged particles from ID, which cover the $|\eta| < 2.5$ region. Three different algorithms which provides complementary information constitute the b-tagging identification:

- **IP2D, IP3D** are algorithms based on the impact parameter,
- **SV** is a secondary vertex algorithm,
- **JetFitter** algorithm evaluates the decay chain.

These information constitute the inputs for a boosted decision tree (BDT) algorithm, giving MV2 algorithm as output, which discriminate b-jets from c-jets and light jets. In the following details on the algorithm will be provided.

IP2D and IP3D algorithms

These algorithms exploit the topology of b-hadron decays. Due to their long lifetimes, b-hadron decay vertexes are displaced from primary vertexes. The transverse impact parameter d_0 and the longitudinal impact parameter $z_0 sin\theta$ measure this distance. The corresponding significance parameters, d_0/σ_{d_0} and $z_0 sin\theta/\sigma_{z_0 sin\theta}$ are then built and used to discriminate tracks matched to jets. A sign is assigned to the impact parameter as function of primary vertex and the jet direction: positive (negative) if primary vertex is in front (behind) with respect to the jet direction. Both transverse and longitudinal impact parameters information are taken into account in the IP3D tagger, which uses a two dimensional template, while IP2D only uses transverse

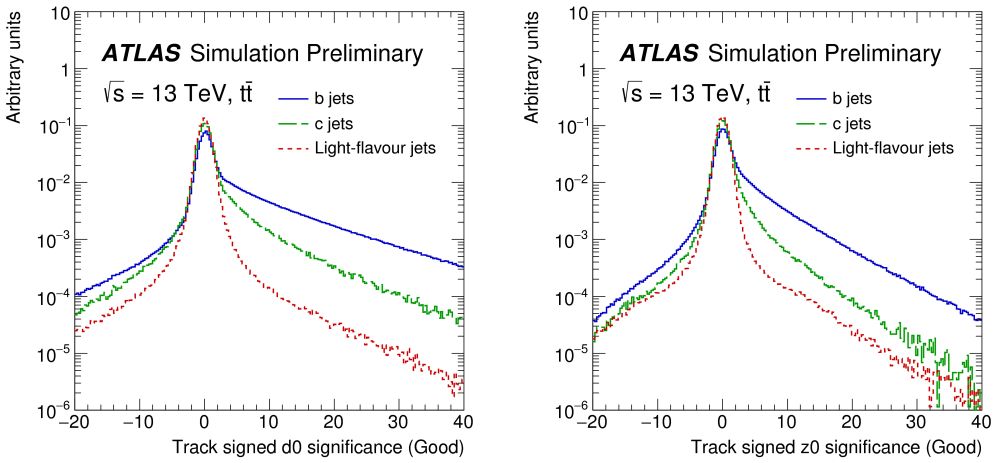

(a) **(b)**

Figure 4.6: The transverse (a) and longitudinal (b) signed impact parameter significance for b (solid green), c (dashed blue) and light-flavour (dotted red) jets [55].

impact parameters, thus resulting in a more performing discriminant not depending on pile-up effects, which are related to the longitudinal impact parameter. Finally a log-likelihood-ratio (LLR) discriminant is built for b-jets, c-jets and light jets separations. In Figure 4.6 the distributions for d_0/σ_{d_0} and $z_0 sin\theta/\sigma_{z_0 sin\theta}$ significances are shown for b-, c- and light jets.

SV algorithm

The secondary vertex algorithm looks for a displaced secondary vertex within the jet. Candidate tracks are considered in pairs and used to reconstruct two-track vertices. If the candidate pair forms a secondary vertex that can be associated to long-lived particles (K_s or Λ), photon conversions or hadronic interaction with the detector material, it is rejected. The final reconstruction efficiency as function of jet p_{T} and η is shown in Figure 4.7 for light, c- and b-jets.

Jet Fitter algorithm

This algorithm reconstruct the whole decay chain, from primary vertex to c-jet, using a Kalman filter to find a common line on which the primary, bottom and charm vertices lie. Some output variables distributions are shown in Figure 4.8.

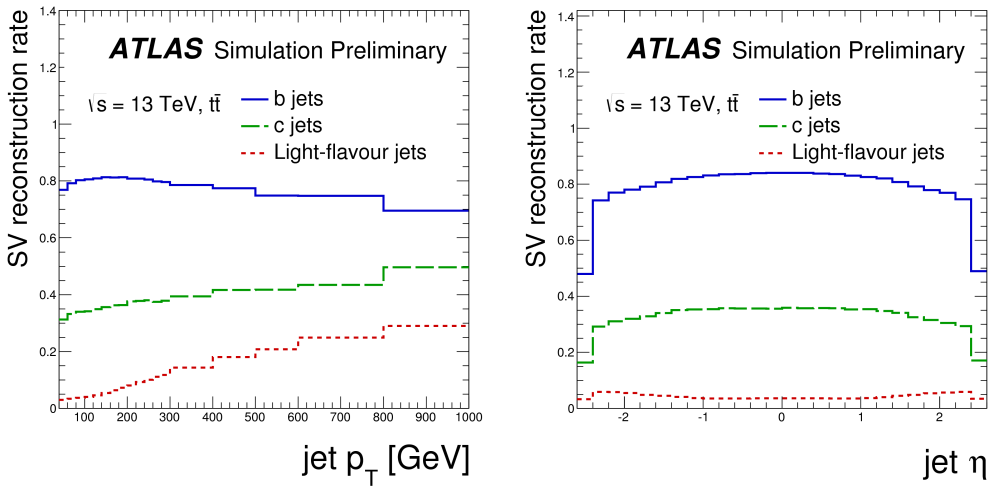

(a) (b)

Figure 4.7: Secondary vertex reconstruction rate as function of jet p_{T} (a) and $|\eta|$ (b). Blue, green and red lines correspond respectively to b-, c- and light flavour jets [55].

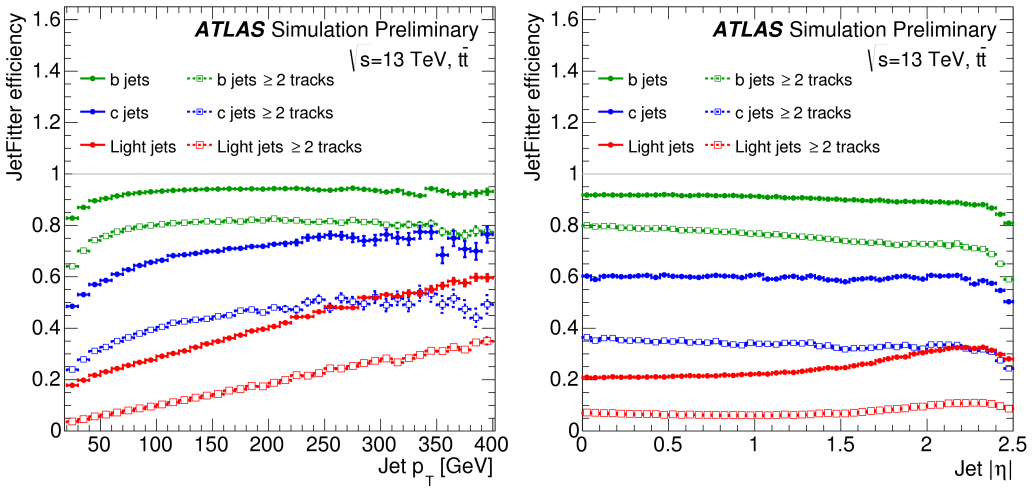

(a) (b)

Figure 4.8: JetFitter vertex efficiency as function of jet p_{T} (a) and η for b (green),c (blue) and light-flavour (red) jets [56].

MV2 algorithm

The outputs of the three algorithms described above, constitute the inputs for a boosted decision tree algorithm, which gives MV2 output. The training

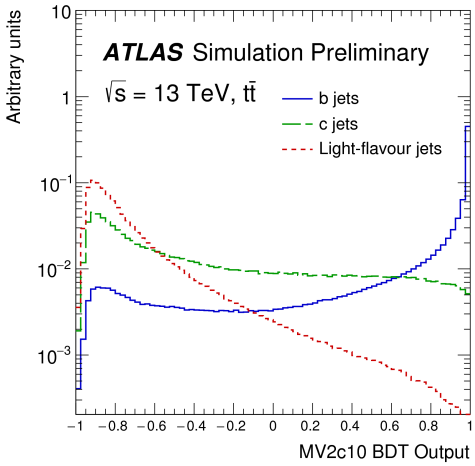

Figure 4.9: BDT output for MV2c10 tagger. Blue, green and red lines correspond respectively to b-, c- and light flavour jets [55].

has been performed on a sample of 5 million $t\bar{t}$ events. It also takes into account p_{T} and $|\eta|$ of the jets in order to exploit correlations with the other input variables, but p_{T} and $|\eta|$ signal distributions are reweighted to match the light flavour jets ones.
Three different versions of the algorithm are implemented: MV2c00, MV2c10 and MV2c20, where cXX represents the c-jet fraction in the training. Hence MV2c20 is a tagger in which 20% (80%) of the background sample is composed by c- (light-flavour) jets. In the current analyses the c-jet rejection has a greater relevance than light flavour rejection: it is possible to perform a training more dedicated to c-jets rejection. This improvement has been reached in the the 2016 tagger configurations: e.g. for MV2c10 provides a light flavour rejection improved of 4% at 77% b-jet efficiency with respect to 2015 configuration, while for c-jet rejection provides an improvement of 40%. Figure 4.9 show the BDT output for the signal and background for MV2c10 and in table 4.2 are reported the relative operating points for different b-jet efficiencies.

4.5 Missing energy reconstruction

Protons colliding at LHC have low momenta in the plane orthogonal to beam pipe. Hence momentum conservation is expected in the transverse plane, whose value is zero. An imbalance in the sum of visible momenta is

BDT Cut Value	b-jet Efficiency [%]	c-jet Rejection	Light-jet Rejection	τ Rejection
0.9349	60	34	1538	184
0.8244	70	12	381	55
0.6459	77	6	134	22
0.1758	85	3.1	33	8.2

Table 4.2: Operating points for MV2c10 tagger [55].

defined as missing transverse energy, $E_{\mathrm{T}}^{\mathrm{miss}}$. The missing transverse energy can indicate the presence of non-detectable particles, such as neutrinos in SM, or new non-interacting particles expected in BSM theories.
Different algorithms for missing transverse energy have been developed: CSR $E_{\mathrm{T}}^{\mathrm{miss}}$, Track $E_{\mathrm{T}}^{\mathrm{miss}}$ and TST $E_{\mathrm{T}}^{\mathrm{miss}}$ [57, 58].
CST (calorimeter-based soft term) $E_{\mathrm{T}}^{\mathrm{miss}}$ compute missing energy form energy deposits in the calorimeters. The measurement include contribution from hard objects (electrons, photons, taus, muons or jets) and soft term related to soft radiation. This method is affected by pile-up interactions, which give additional contributions to the CST term. The Inner Detector information is used in Track-based methods, thus giving a more robustness with respect to pile-up but the method is insensitive to neutral particles and has an acceptance limited by the region covered from ID. TST $E_{\mathrm{T}}^{\mathrm{miss}}$ method both combines information from calorimeters and trackers, the latter being included as track-based soft term (TST).In Run-2 analyses TST $E_{\mathrm{T}}^{\mathrm{miss}}$ is the method adopted.
The $E_{\mathrm{T}}^{\mathrm{miss}}$ of an event is computed as the negative sum of the momenta of all final state objects in the transverse plane:

$$E_{x(y)}^{miss} = E_{x(y)}^{miss,e} + E_{x(y)}^{miss,\gamma} + E_{x(y)}^{miss,\tau} + E_{x(y)}^{miss,jets} + E_{x(y)}^{miss,\mu} + E_{x(y)}^{miss,soft}. \quad (4.6)$$

Where the order of the objects follows the reconstruction order of energy deposits in the calorimeters. The choice of soft term (TST or CST) affects the performance and the uncertainties in the missing energy reconstruction. The corresponding magnitude and azimuthal angle are:

$$E_{\mathrm{T}}^{\mathrm{miss}} = \sqrt{(E_x^{miss})^2 + (E_y^{miss})^2} \quad (4.7)$$

$$\phi^{miss} = \arctan(E_y^{miss}/E_x^{miss}). \quad (4.8)$$

Chapter 5

Search for beyond Standard Model Physics in events with bottom quarks and missing transverse energy

The analysis with bottom quarks and missing transverse energy in the final state will be described in this chapter. The dataset corresponds to the full available Run-2 statistics collected by ATLAS at $\sqrt{s} = 13\text{TeV}$. Several improvements in the analysis have been introduced with respect to the Run-1 results: for the signal samples simplified models have been adopted in place of EFT models and new fitting strategies have been used to improve sensitivity limits.

5.1 Data and Monte Carlo samples

5.1.1 Experimental dataset

The full Run-2 dataset collected by ATLAS detector at a center of mass energy of $\sqrt{s} = 13\text{TeV}$ has been used. 2015 data taking operations covered the period from June to November while 2016 from April to October, both with a bunch-crossing space of 25 ns. The data collected in 2015 and 2016 correspond respectively to an integrated luminosity of $3.2\,\text{fb}^{-1}$ and $32.9\,\text{fb}^{-1}$, for a total collected luminosity of $36.1\,\text{fb}^{-1}$. For physics analyses only datasets satisfying some quality criteria are used: the list containing these runs is the GoodRunList (GRL), which provides that events have been selected when all ATLAS subdetectors were fully operating thus ensuring good data quality.

5.1.2 Monte Carlo simulation

Monte Carlo (MC) samples have been generated in order to reproduce Run-2 LHC collisions with an energy in the centre of mass of $\sqrt{s} = 13$ TeV and a bunch cross spacing of 25 ns. These simulations are used to control each step of physics analyses, from background and signal modelling to final results. Different MC generators have been used in order to simulate signal and background processes.

Signal samples: s-channel models

The signal processes for the s-channel models are generated from LO matrix elements with two b-quarks and up to one extra parton, using the MadGraph [59] v2.2.3 generator interfaced to Pythia 8.186 with the A14 tune [60] for the modelling of parton showering, hadronisation and the description of the underlying event. Parton luminosities are provided by the NNPDF30LO [61] PDF set. The samples were generated following 4-flavour scheme with massive b-quarks. Jet-parton matching is realised following the CKKW-L prescription [62], with a fixed matching scale (30 GeV). Following the prescriptions agreed with CMS in the DMForum [25], the samples were generated applying the following cuts at MadGraph level:

1. ptj cut 30 GeV ,
2. xptb cut 30 GeV .

The second cut is effectively increasing the generation fiducial phase space and effectively behaving as a filter. The effect of this requirement is propagated into the LO MadGraph cross section. An additional $E_{\mathrm{T}}^{\mathrm{miss}}$ filter of 80 GeV was also applied, in order to enhance the samples efficiency in the phase space interesting for this analysis. Two grids of signals have been generated, both for scalar and pseudoscalar mediators. For the fixed DM mass $m_\chi = 1$ GeV a scan on mediator mass m_Φ has been performed with considered masses $m_\Phi = 10, 20, 50, 100, 200, 300, 500, 1000$ GeV . The corresponding Feynman diagram for this process is shown in Figure 5.1a.

Signal samples: t-channel b-FDM models

The signal processes for the t-channel models are generated from LO matrix elements with up to three extra parton (in addition to the DM pair), using the MadGraph v2.2.3 generator interfaced to Pythia 8.186 with the A14 tune for the modelling of parton showering, hadronisation and the description of the underlying event. Parton luminosities are provided

by the NNPDF30LO PDF set. The samples were generated following 5-flavour scheme with massless b-quarks. The grid for t-channel models is a two-dimensional grid produced by scanning the mediator mass $m_\Phi = 10, 50, 100, 200, 400, 500, 600, 800, 1000, 1200, 1400, 1600$, for few DM masses $m_\chi = 1, 35, 50, 100$ GeV. The corresponding Feynman diagram for this process is shown in Figure 5.1b.

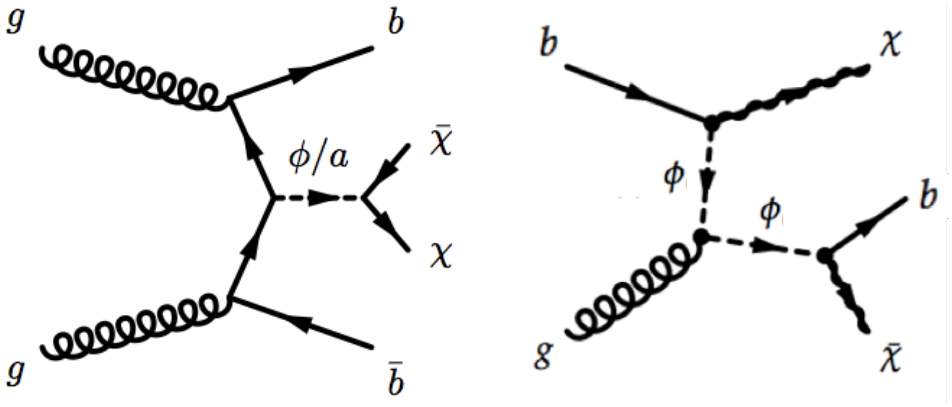

(a) s-channel **(b)** t-channel

Figure 5.1: Representative diagrams for s-channel spin-0 (a) and t-channel scalar (b) mediators production.

Background samples

V+jets backgrounds have been generated using SHERPA [63]. Each final state, $Z \to \nu\nu$, $Z \to ee$, $Z \to \mu\mu$, $Z \to \tau\tau$, $W \to e\nu$, $W \to \mu\nu$, $W \to \tau\nu$ is separately generated. All single final state process is split in p_{T} slices and in heavy flavour components, namely B-veto, C-filter-B-veto and B-filter and then summed to get an inclusive set of samples. The $Z \to \ell\ell$ samples have a cut on $m(\ell\ell) > 40$GeV applied.
The production of top quark pairs ($t\bar{t}$) is simulated using Powheg+Pythia6 using the P2012 tune. Single top samples are generated with Powheg+Pythia6, with the P2012 tune and the PDF set CTEQ6L1.
Diboson MC samples have also been generated with SHERPAwith next-to-leading order (NLO) parton distribution functions (PDF) set CT10, with up to 4 jets from matrix element (ME), with massive charm and bottom quarks.
Samples of $t\bar{t} + V$ (with $V = W$ and Z, including non-resonant Z/γ^* contributions) production are generated at NLO with MADGRAPH5_aMC@NLO v2.2.2 interfaced to the PYTHIA 8.186 parton shower model [64].
Samples of $t\bar{t} + WW$ production are generated at LO with MADGRAPH5_aMC@NLO +

Pythia 8 without additional partons included in the generation. The A14 tune [60] was used together with the NNPDF23LO PDF set[65].
The $t\bar{t} + W$, $t\bar{t} + Z$, $t\bar{t} + WW$ events are normalised to their NLO cross section [59]. In order to reproduce the pile-up levels present in the collisions data the distribution of the average number of expected interactions per bunch crossing ($< \mu >$) in the MC is re-weighted to match that observed in data.

5.2 Object Reconstruction

In this analysis jets, b-jets, muons, electrons and missing transverse momentum are the objects selected. *Baseline* and *Good* object definitions are introduced for jets, electrons and muons: baseline objects are used for preselection and overlap removal procedure good objects are required for the final event selection both in signal and control regions.

Jets

The jet reconstruction follows the procedure described in Section 4.3. Baseline jets requires $p_{\mathrm{T}} > 20\,\mathrm{GeV}$ and $|\eta| < 2.8$; good jets are further required to pass JVT > 0.59 (defined in Section 4.3) if its p_{T} is below 60 GeV and $|\eta| < 2.4$. The non-collision background originating from muons coming from inelastic interactions and calorimeter noise contributions are suppressed by requiring the Loose jet cleaning criteria to baseline jets that pass the overlap removal procedure.
Jets with $p_{\mathrm{T}} > 20\,\mathrm{GeV}$ and $|\eta| < 2.4$ are identified as b-jets if MV2c10 b-tagging discriminant (Section) is above 0.9349, which corresponds to a b-tagging efficiency $\epsilon_b = 60.03\%$. The rejection rated for c-, light flavour and τ jets are reported in Table 4.2. The choice of a tighter Working Point (WP) is motivated by sensitivity studies, which show (Figure 5.2) a better rejection on the background with a small signal efficiency loss (for a signal benchmark with $M_{med} = 20\,\mathrm{GeV}$ and $m_\chi = 1\,\mathrm{GeV}$ the sensitivity of requiring 2 b-jets at 60% WP is $\sim 30\%$ greater with respect to the 85% WP).
The analysis jet selection is summarised in Table 5.1.

Electrons and Muons

Baseline electrons are required to have $E_{\mathrm{T}} > 7\,\mathrm{GeV}$ and $|\eta| < 2.47$ and pass the "LooseAndBLayerLLH" definition. Baseline electrons are used to perform the overlap removal between jets and electrons, and in lepton veto. This definition improves the W+jets rejection at preselection step

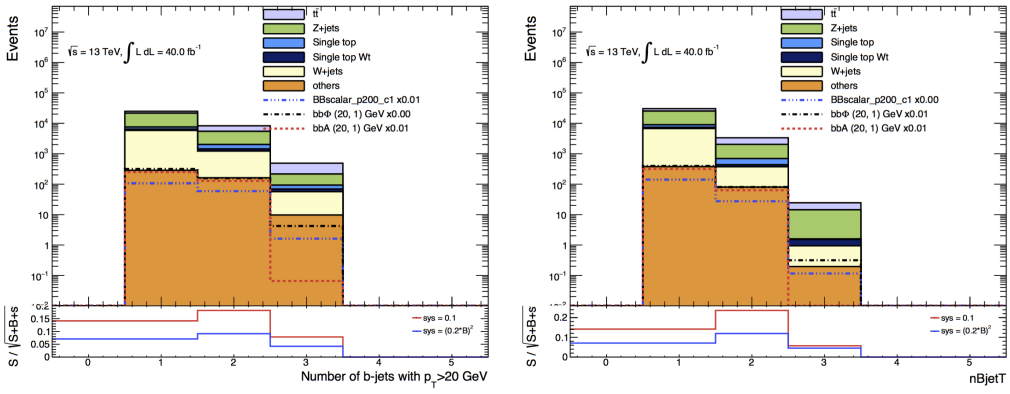

(a) nBjet 85% WP **(b)** nBjet 60% WP

Figure 5.2: Study of the optimal working point at preselection level for s-channel models. MV2c10 with 85% (a) and 60% (b) are shown.

of the analysis (between 10% and 40%) with respect to a previous tighter definition of baseline electrons with $E_{\mathrm{T}} > 20\,\mathrm{GeV}$. Signal electrons are "TightLLH" electrons with $E_{\mathrm{T}} > 25$ GeV. Further requirements are applied by requiring isolated electrons with "LooseTrackOnly" as working point, and cuts are applied on impact significance parameters $d_0/\sigma_{d_0} < 5$ and $z_0 sin\theta/\sigma_{z_0 sin\theta} < 0.5$.
Muon candidates pass "Medium" identification criteria. Baseline muons have $p_{\mathrm{T}} > 6\,\mathrm{GeV}$ and $|\eta| < 2.5$, $d_0/\sigma_{d_0} < 3$ and $z_0 sin\theta/\sigma_{z_0 sin\theta} < 0.5$. They are used in the overlap removal procedure between jets and muons and for vetoing events. Signal muons have $p_{\mathrm{T}} > 25\,\mathrm{GeV}$ and satisfy "LooseTrackOnly" isolation criteria.
Electrons and Muons definitions are listed in Table 5.2.

Missing transverse momentum

The missing transverse momentum used in this analysis includes track-soft-term (TST, see Section 4.5). Quality criteria are applied to remove fakes or bad tracks included in the TST: jet threshold is above 20 GeV while only charged particle below this threshold will be included in TST. The missing transverse momentum is calculated as the negative vector sum of the transverse momenta of all objects, after internal overlap removal to avoid double counting. Two missing transverse momentum are used according to selection: the standard one, referred as $E_{\mathrm{T}}^{\mathrm{miss}}$ and the missing energy corrected by the lepton momenta $E_{\mathrm{T}}^{\mathrm{miss}}$ nolep, which treats leptons as invisible objects.

Cut	Value
Baseline	
p_{T}	$> 20\,\mathrm{GeV}$
Signal	
p_{T}	$> 20\,\mathrm{GeV}$
$\lvert\eta\rvert$	< 2.8
JVT	> 0.59 for $\lvert\eta\rvert < 2.4$ and $p_{\mathrm{T}} < 60\,\mathrm{GeV}$
b-jets	
p_{T}	$> 20\,\mathrm{GeV}$
$\lvert\eta\rvert$	< 2.5
JVT	> 0.59 for $\lvert\eta\rvert < 2.4$ and $p_{\mathrm{T}} < 60\,\mathrm{GeV}$
MV2c10	60% WP

Table 5.1: Selection criteria for jets and b-jets.

Cut	Value
Baseline	
ID	LooseAndBLayerLLH
E_{T}	$> 7\,\mathrm{GeV}$
$\lvert\eta\rvert$	< 2.47
Signal	
ID	TightLLH
E_{T}	$> 25\,\mathrm{GeV}$
Isolation	LooseTrackOnly
d_0 significance	< 5
$z_0 \sin(\theta)$	$< 0.5\,\mathrm{mm}$

(a) Electron selection criteria

Cut	Value
Baseline	
ID	Medium
p_{T}	$> 6\,\mathrm{GeV}$
$\lvert\eta\rvert$	< 2.5
Signal	
ID	Medium
p_{T}	$> 25\,\mathrm{GeV}$
Isolation	LooseTrackOnly
d_0 significance	< 3
$z_0 \sin(\theta)$	$< 0.5\,\mathrm{mm}$

(b) Muon selection criteria

Table 5.2: Summary of the electron (a) and muon (b) selection criteria.

5.2.1 Overlap removal

An overlap removal procedure is applied in order to avoid overlapping between candidate objects. The ambiguity is solved according to the distance ΔR between the objects. The following criteria are applied:

1. A jet is removed if its distance with a baseline electron is $\Delta R < 0.2$. The object is considered as electron unless the jet is b-tagged (85% WP): in this case the electron is removed.

2. A muon is removed if its distance with a jet is $\Delta R < 0.4$ and the jet has at least three tracks (with $p_{\mathrm{T}} > 500\,\mathrm{MeV}$), otherwise the muon is kept and the jet is removed.

3. If an electron and a jet are within a distance $0.2 \leq \Delta R < 0.4$, the jet is kept and the electron is removed.

5.2.2 Trigger

The trigger items used in this analysis are missing energy (xe) and single lepton triggers.
The signal samples show have a very soft $E_{\mathrm{T}}^{\mathrm{miss}}$ spectrum: for a signal with $M_{med} = 20\,\mathrm{GeV}$ and $m_{\chi} = 1\,\mathrm{GeV}$ a $E_{\mathrm{T}}^{\mathrm{miss}} > 200\,\mathrm{GeV}$ cut leads to a signal efficiency of 0.4%. In order to improve the signal efficiency trigger strategy is based on the lowest unprescaled $E_{\mathrm{T}}^{\mathrm{miss}}$ triggers. Since they change during data taking periods, different trigger items have been considered in the selection:

- 2015: HLT_xe70_mht or HLT_j80_xe80
- 2016 until period D3: HLT_xe90_mht_L1XE50 or HLT_xe100_mht_L1XE50
- 2016 from period D3: HLT_xe110_mht_L1XE50

where "_L1XE50" indicates a seed corresponding to a Level 1 requiremet on $E_{\mathrm{T}}^{\mathrm{miss}} > 50$ GeV and _mht refers to the $E_{\mathrm{T}}^{\mathrm{miss}}$ calculation implemented from the vectorial sum of all jets in the event with $p_{\mathrm{T}} > 7$ GeV. For each trigger the efficiency curve (*turn-on*) as function of the $E_{\mathrm{T}}^{\mathrm{miss}}$ has been obtained both on data and on MC using a single muon trigger as support. The selection requires events with exactly one muon, 2-3 jets, 1 b-jet. The corresponding turn-on curves are shown in Figure 5.3 for 2015 triggers, in Figure 5.4 for HLT_xe90_mht_L1XE50 and HLT_xe100_mht_L1XE50 triggers, and Figure 5.5 for the HLT_xe110_mht_L1XE50 trigger as a function of the offline $E_{\mathrm{T}}^{\mathrm{miss}}$ corrected for the leptons. All trigger items are fully efficient for $E_{\mathrm{T}}^{\mathrm{miss}} > 180$ GeV.

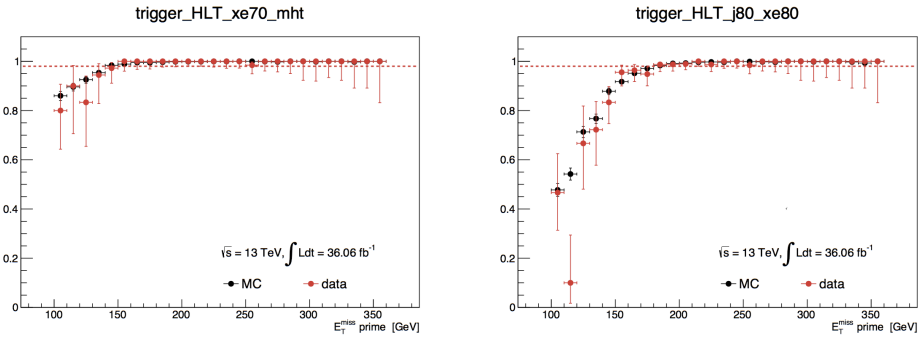

(a) HLT_xe70 **(b)** HLT_j80_xe80

Figure 5.3: Trigger efficiency curves for 2015 xe triggers (data and MC), as a function of the offline $E_{\mathrm{T}}^{\mathrm{miss}}$, corrected for the leptons.

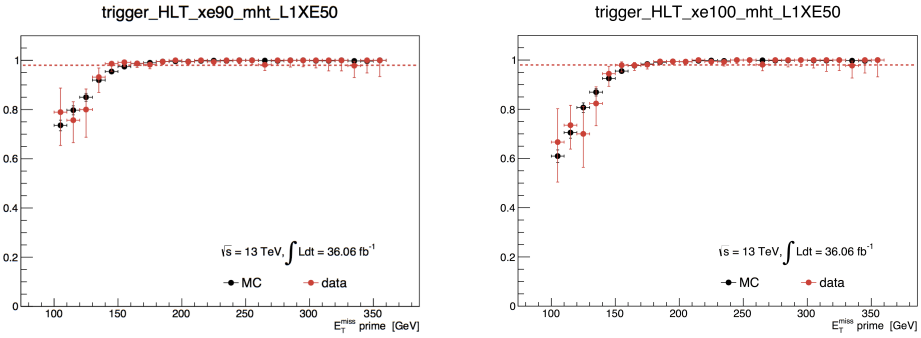

(a) HLT_xe90_mht_L1XE50 **(b)** HLT_xe100_mht_L1XE50

Figure 5.4: Trigger efficiency curves for 2016 xe primary triggers (data and MC), as a function of the offline $E_{\mathrm{T}}^{\mathrm{miss}}$, corrected for the leptons.

Single lepton triggers are used in selection containing one or two leptons, using an OR of the triggers listed in Table 5.3. The trigger items employ different identification and isolation criteria for the leptons (loose, medium, tight); HLT_e24_lhmedium_L1EM20VH and HLT_mu20_iloose_L1MU5 use a Level 1 seed on lepton transverse energy, and _nod0 indicates that requirements on d_0 are not applied in the online identification. A full trigger efficiency is reached for lepton $p_{\mathrm{T}} > 30$ GeV.

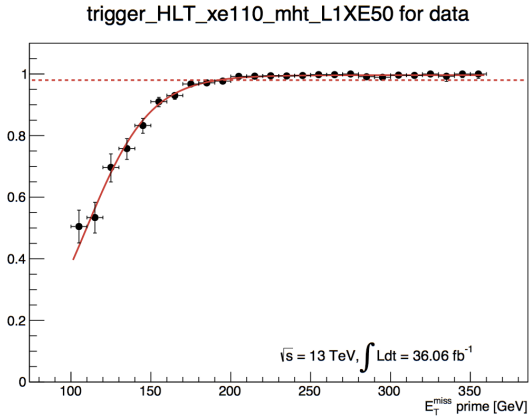

Figure 5.5: Trigger efficiency for the highest xe trigger threshold in 2016 data, as a function of $E_{\mathrm{T}}^{\mathrm{miss}}$, corrected for the leptons.

Year	Lepton	Trigger chains
2015	electron	HLT_e24_lhmedium_L1EM20VH ‖ HLT_e60_lhmedium ‖ HLT_e120_lhloose
2015	muon	HLT_mu20_iloose_L1MU5 ‖ HLT_mu50
2016	electron	HLT_e26_lhtight_nod0_ivarloose ‖ HLT_e60_lhmedium_nod0 ‖ HLT_e140_lhloose_nod0
2016	muon	HLT_mu26_ivarmedium ‖ HLT_mu50

Table 5.3: Lepton trigger scheme for the 1- and 2-lepton control regions.

5.3 Event selection

5.3.1 Preselections

A preliminary data/MC comparison has been performed at the initial step of the anlaysis (*Preselection*). The modelling of kinematic variables has been validated by defining different preselection cuts for s-channel and t-channel analyses. Both models are characterized by the presence of b-jets with a low jet multiplicity. In s-channel models in order to reduce the contamination from high jet multiplicity backgrounds, especially $t\bar{t}$ production, a veto on the third jet with $p_{\mathrm{T}} > 60\,\mathrm{GeV}$ is applied.
For s-channel models preselections applied are:

- a zero lepton selection (PRE0L_2b) to collect events with similar kinematic properties of signal region,
- a single lepton selection (PRE1L_2b) to validate backgrounds containing leptonic W-decays,
- a dilepton selection to validate backgrounds containing a Z boson. In

this selection $E_{\mathrm{T}}^{\mathrm{miss}}$ nolep has been used in order to mimic the $Z \to \nu\nu$ decay which constitutes the dominant background in signal region.

The full list of cuts applied is shown in Table 5.4.
For t-channel models preselections are the following:

- a zero lepton selection (PRE0L_1b) in order to have a region kinematically similar to the signal region,
- a dilepton selection (PRE2L_1b) to validate backgrounds containing a Z boson in the event.

All selection cuts are summarized in Table 5.5. Both for one lepton and two lepton preselections, the electron and muon channels are combined.

Variable	PRE0L_2b
Trigger	xe
$\mathcal{N}_{jets}$	$[2, 3]$
$\mathcal{N}_{bjets}$	> 1
$\mathcal{N}_{lep}$ (baseline)	0
$p_{\mathrm{T}}^{\mathrm{j1}}$	$> 150\,\mathrm{GeV}$
$p_{\mathrm{T}}^{\mathrm{j2}}$	$> 20\,\mathrm{GeV}$
$p_{\mathrm{T}}^{\mathrm{j3}}$	$< 60\,\mathrm{GeV}$
$E_{\mathrm{T}}^{\mathrm{miss}}$	$> 180\,\mathrm{GeV}$
$\min \Delta\phi(j_i, E_{\mathrm{T}}^{\mathrm{miss}})_{i=1,2,3}$	> 0.4

(a) Zero lepton pre-selections

Variable	PRE1L_2b
Trigger	single lepton
$\mathcal{N}_{jets}$	$[2, 3]$
$\mathcal{N}_{bjets}$	> 0
$\mathcal{N}_{bjets}$	> 1
$\mathcal{N}_{lep}$ (signal)	1
$\mathcal{N}_{lep}$ (baseline)	1
$p_{\mathrm{T}}^{\mathrm{j1}}$	$> 150\,\mathrm{GeV}$
$p_{\mathrm{T}}^{\mathrm{j2}}$	$> 20\,\mathrm{GeV}$
$p_{\mathrm{T}}^{\mathrm{j3}}$	$< 60\,\mathrm{GeV}$
$E_{\mathrm{T}}^{\mathrm{miss}}$	$> 180\,\mathrm{GeV}$
$\min \Delta\phi(j_{1,2,3}, E_{\mathrm{T}}^{\mathrm{miss}})$	> 0.4
lep p_{T}	$> 30\,\mathrm{GeV}$
m_T^{lep}	> 30

(b) Single lepton pre-selections

Variable	PRE2L_2b
Trigger	single lepton
$\mathcal{N}_{jets}$	$[2, 3]$
$\mathcal{N}_{bjets}$	> 1
$\mathcal{N}_{lep}$ (signal)	2
$\mathcal{N}_{lep}$ (baseline)	2
$p_{\mathrm{T}}^{\mathrm{j1}}$	$> 150\,\mathrm{GeV}$
$p_{\mathrm{T}}^{\mathrm{j2}}$	$> 20\,\mathrm{GeV}$
$p_{\mathrm{T}}^{\mathrm{j3}}$	$< 60\,\mathrm{GeV}$
$E_{\mathrm{T}}^{\mathrm{miss}}$ (nolep)	$> 180\,\mathrm{GeV}$
$E_{\mathrm{T}}^{\mathrm{miss}}$	$< 60\,\mathrm{GeV}$
$\min \Delta\phi(j_i, E_{\mathrm{T}}^{\mathrm{miss}})_{i=1,2,3}$	> 0.4
lep1 p_{T}	$> 30\,\mathrm{GeV}$
lep2 p_{T}	$> 25\,\mathrm{GeV}$
$m_{\ell\ell}$	$[71, 111]$

(c) Two leptons pre-selections

Table 5.4: Preselection cuts for zero (a) one (b) and two leptons (c) preselections for s-channel models.

Variable	PRE0L_1b
Trigger	xe
$\mathcal{N}_{jets}$	$[2, 3]$
$\mathcal{N}_{bjets}$	> 0
$\mathcal{N}_{lep}$ (baseline)	0
$p_{\mathrm{T}}^{\mathrm{j1}}$	$> 100\,\mathrm{GeV}$
$p_{\mathrm{T}}^{\mathrm{j2}}$	$> 100\,\mathrm{GeV}$
$p_{\mathrm{T}}^{\mathrm{j3}}$	$< 60\,\mathrm{GeV}$
$E_{\mathrm{T}}^{\mathrm{miss}}$	$> 300\,\mathrm{GeV}$
$\min \Delta\phi(j_i, E_{\mathrm{T}}^{\mathrm{miss}})_{i=1,2,3}$	> 0.4

(a) Zero lepton pre-selections

Variable	PRE2L_1b
Trigger	single lepton
$\mathcal{N}_{jets}$	$[2, 3]$
$\mathcal{N}_{bjets}$	> 0
$\mathcal{N}_{lep}$ (signal)	2
$\mathcal{N}_{lep}$ (baseline)	2
$p_{\mathrm{T}}^{\mathrm{j1}}$	$100\,\mathrm{GeV}$
$p_{\mathrm{T}}^{\mathrm{j2}}$	$100\,\mathrm{GeV}$
$p_{\mathrm{T}}^{\mathrm{j3}}$	-
$E_{\mathrm{T}}^{\mathrm{miss}}$ (nolep)	$100\,\mathrm{GeV}$
$E_{\mathrm{T}}^{\mathrm{miss}}$	$< 60\,\mathrm{GeV}$
$\min \Delta\phi(j_i, E_{\mathrm{T}}^{\mathrm{miss}})_{i=1,2,3}$	> 0.4
lep1 p_{T}	$> 30\,\mathrm{GeV}$
lep2 p_{T}	$> 25\,\mathrm{GeV}$
$m_{\ell\ell}$	$[71, 111]$

(b) Two leptons pre-selections

Table 5.5: Preselection cuts for zero (a) and two leptons (b) preselections for t-channel models.

5.3.2 Discriminating variables

In order to improve signal selection with respect to the background several kinematic variables have been implemented:

Minimum angular separation of all jets to $E_{\mathbf{T}}^{\mathbf{miss}}$, $\min \Delta\phi(j_i, E_{\mathbf{T}}^{\mathbf{miss}})$. A cut on this variable helps to reduce multi-jet contamination. $\min \Delta\phi(j_i, E_{\mathrm{T}}^{\mathrm{miss}})$ computes the minimum of the azimuthal distance between the $E_{\mathrm{T}}^{\mathrm{miss}}$ and all jets selected in the event. (Figure 5.6a)

Minimum angular jets separation, ΔR_{min}. The angular separation ΔR between two jets is defined as

$$\Delta R(j1, j2) = \sqrt{(\eta_1 - \eta_2)^2 + (\phi_1 - \phi_2)^2}. \tag{5.1}$$

In this analysis, $\Delta R_{min}$is used, as the minimum ΔR between all jets in the event (Figure 5.6f).

Event imbalance, $p_{\mathrm{T}}^{\mathrm{jet1}}/\mathrm{H_T}$, particularly performing in $t\bar{t}$ event rejection, is defined as the ratio between the leading jet transverse momentum ($p_{\mathrm{T}}^{\mathrm{jet1}}$) and the jet transverse momentum scalar sum of all signal jets in the event $\mathrm{H_T}$ (Figure 5.6b).

Pseudorapidity separation, $\Delta\eta_{bb}$, which is the pseudorapidity separation between the two bjets of the event. If only one b-jet is present in the selected event, the second jet with the highest b-tagging weight is considered in the variable computation.

Correlation variables x1 and y1. These two variables are strongly correlated to $\min \Delta\phi(j_i, E_{\mathrm{T}}^{\mathrm{miss}})$ and $\Delta\phi_{bb}$ and defined as:

$$x1 = \min \Delta\phi(j_i, E_{\mathrm{T}}^{\mathrm{miss}}) - \Delta\phi_{bb} \tag{5.2}$$

$$y1 = \pi - \min \Delta\phi(j_i, E_{\mathrm{T}}^{\mathrm{miss}}) - \Delta\phi_{bb} \tag{5.3}$$

Their representation can be seen in a $\min \Delta\phi(j_i, E_{\mathrm{T}}^{\mathrm{miss}}) - \Delta\phi_{bb}$ correlation plot, as shown in Figures 5.6d 5.6e and 5.7 for the major backgrounds and a signal model.

The variable $\cos\theta^*$, proposed for DM searches in [66], is used as discriminating variable in the fit procedure. It is defined as the cosine of the bjets system opening angle (Figure 5.6c):

$$\cos\theta^* = |\tanh(\Delta\eta_{bb}/2)|. \tag{5.4}$$

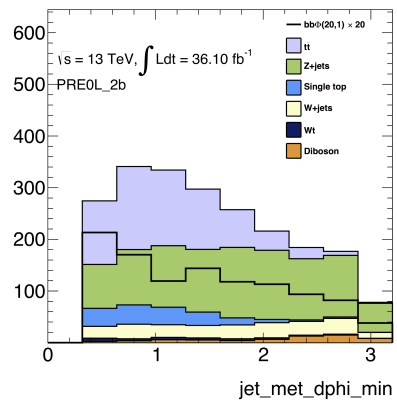

(a) $\min \Delta\phi(j_i, E_{\mathrm{T}}^{\mathrm{miss}})_{i=1,2,3}$

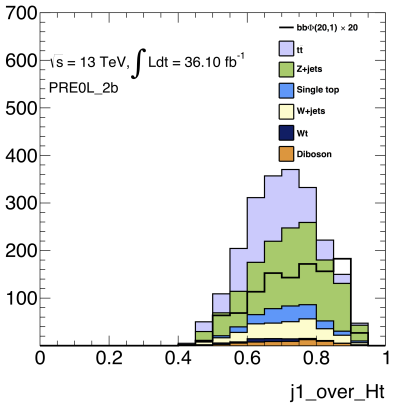

(b) $p_{\mathrm{T}}^{\mathrm{jet1}}/\mathrm{H_T}$

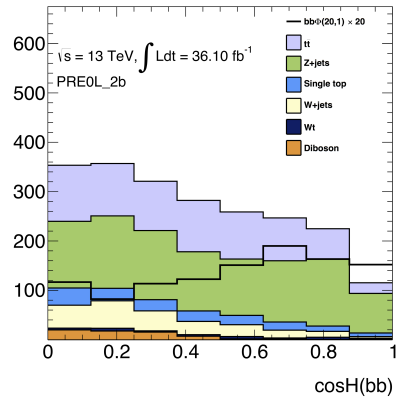

(c) $\cos\theta^*$

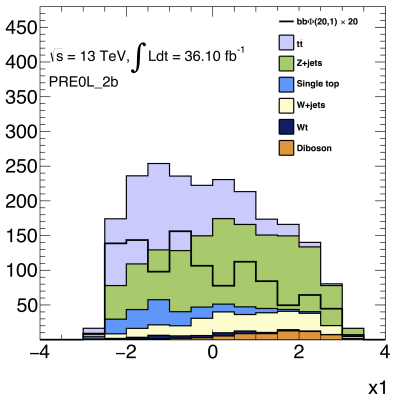

(d) $x1$

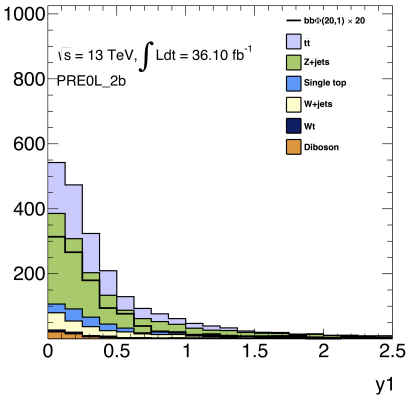

(e) $y1$

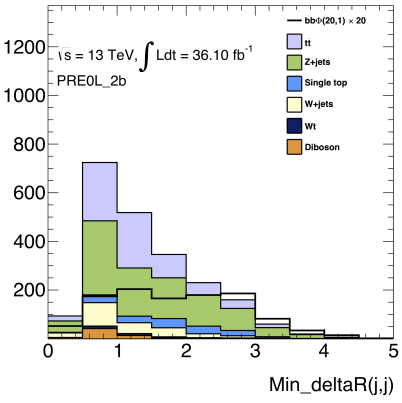

(f) ΔR_{min}

Figure 5.6: Comparison between the benchmark signal model with $M_{med} = 20\,\mathrm{GeV}$ and $m_\chi = 1\,\mathrm{GeV}$ and the SM background at preselection level for the most important discriminating variables of this analysis. The signal yields are multiplied by a factor 20.

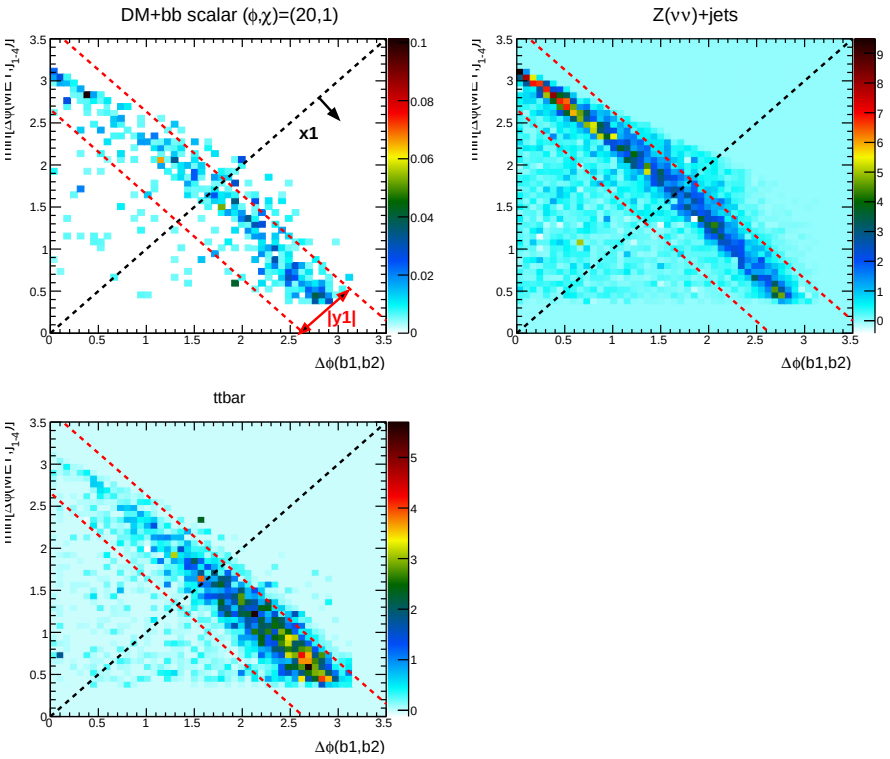

Figure 5.7: 2-dimensional representation of the definition of variable x1 and y1. x-axis is the $\Delta\phi_{bb}$ and y-axis is the $\min\Delta\phi(j_i, E_{\mathrm{T}}^{\mathrm{miss}})_{i=1,2,3}$.

5.3.3 Signal region selections

Signal region for s-channel models

Signal samples from simplified models are characterized by low jet multiplicity and low $E_{\mathrm{T}}^{\mathrm{miss}}$ spectrum. The analysis selections exploits the kinematic variables described in section 5.3.2 in order to maximize the following figure of merit (*significance*)

$$\frac{s}{\sqrt{(1+b+(b\times err_b)^2}}, \tag{5.5}$$

where s and b are respectively the expected number of signal and background events and err_b refers to a global systematic uncertainty on the background. This means that each cut has been chosen in a such way to give the highest value of the significance. In order to adopt a conservative approach before background uncertainty estimation for signal region optimizations the value chosen corresponds to $err_b = 0.20$.
Two signal regions have been defined for this analysis: SRB and SRM. While the former is the nominal one, the latter is kept as a cross check for its similarity with the previous analysis [67]. In SRM a different momentum imbalance has been used, and defined as

$$\mathcal{I}(jw1, jw2) = \frac{jw1 - jw2}{jw1 + jw2}, \tag{5.6}$$

that is the p_{T} imbalance for the two most "b-like" jets in the event. The corresponding applied cuts are listed in Table 5.6. The distributions of discriminating variables where all cuts are applied except the one based on the plotted variable (usually referred as *N-1* distributions) are shown in Figure 5.8 for SRB and in Figure 5.9 for SRM.

Signal region for t-channel models

These models are characterized by a high momentum b-jet and large $E_{\mathrm{T}}^{\mathrm{miss}}$. The signal region optimization has been designed for high mediator masses (> 1 TeV), by following the procedure described for s-channel models, using as figure of merit the significance defined in equation 5.5. The final selections are listed in Table 5.7 for a signal region named SRBFH. The variable HT3 defined as

$$HT3 = \sum_{i=3}^{\mathrm{Njets}} p_{\mathrm{T}}^{\mathrm{jet}} \tag{5.7}$$

has been exploited to control $t\bar{t}$.

Quantity	SRB
Preselections	0-lep
$\mathcal{N}_{jets}$	$[2, 3]$
$\mathcal{N}_{\mathrm{b}jets}$	≥ 2
Bjet 1 p_{T} [GeV]	> 150
jet 1 p_{T} [GeV]	> 150
jet 2 p_{T} [GeV]	> 20
jet 3 p_{T} [GeV]	< 60
$E_{\mathrm{T}}^{\mathrm{miss}}$ [GeV]	> 180
$p_{\mathrm{T}}^{\mathrm{jet1}}/\mathrm{H}_{\mathrm{T}}$	> 0.75
$x1$	< 0
$\lvert y1 \rvert$	< 0.5

(a) SRB definition

Quantity	SRM
Preselections	0-lep
$\mathcal{N}_{jets}$	$[2, 3]$
$\mathcal{N}_{\mathrm{b}jets}$	2
Bjet 1 p_{T} [GeV]	> 50
jet 1 p_{T} [GeV]	> 150
jet 2 p_{T} [GeV]	> 20
jet 3 p_{T} [GeV]	< 60
$E_{\mathrm{T}}^{\mathrm{miss}}$ [GeV]	> 180
$\mathcal{I}(jw1, jw2)$	> 0.5
$\Delta R_{min}(j1, j2)$	> 2.5

(b) SRM definition

Table 5.6: Summary of the selections for SRB and SRM. Preselection refers to the requirements summarised in Table 5.4.

Quantity	SRBFH
$\mathcal{N}_{\mathrm{b}jets}$	≥ 1
$\mathcal{N}_{\mathrm{j}ets}$	≥ 2
$E_{\mathrm{T}}^{\mathrm{miss}}$ [GeV]	> 650
Jet 1 p_{T} [GeV]	> 160
Jet 2 p_{T} [GeV]	> 160
HT3 [GeV]	> 100
$\lvert \min \Delta\phi(j_i, E_{\mathrm{T}}^{\mathrm{miss}}) \rvert \; i = 1, 2$	> 0.6

Table 5.7: Selections applied in SRBFH.

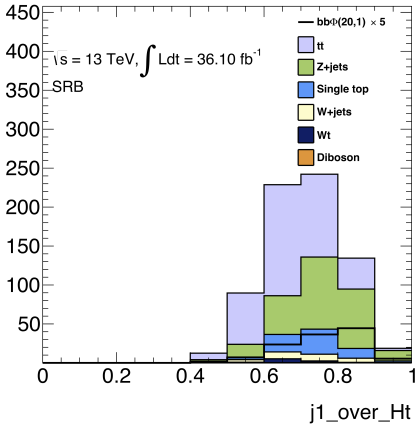

(a) $p_{\mathrm{T}}^{\mathrm{jet1}}/\mathrm{H_T}$

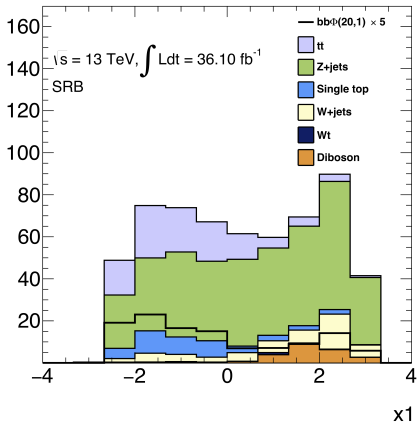

(b) $x1$

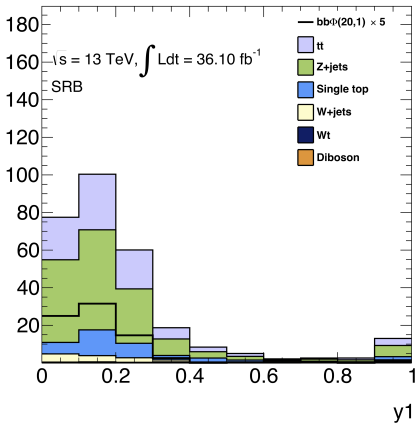

(c) $y1$

Figure 5.8: Discriminating variables for SRB. For each distribution all cuts except the one showed in the plot are applied. Signal models with $m_\chi = 1\,\mathrm{GeV}$ and $M_{med} = 20, 200\,\mathrm{GeV}$ have been considered with a cross section increased by a factor 5.

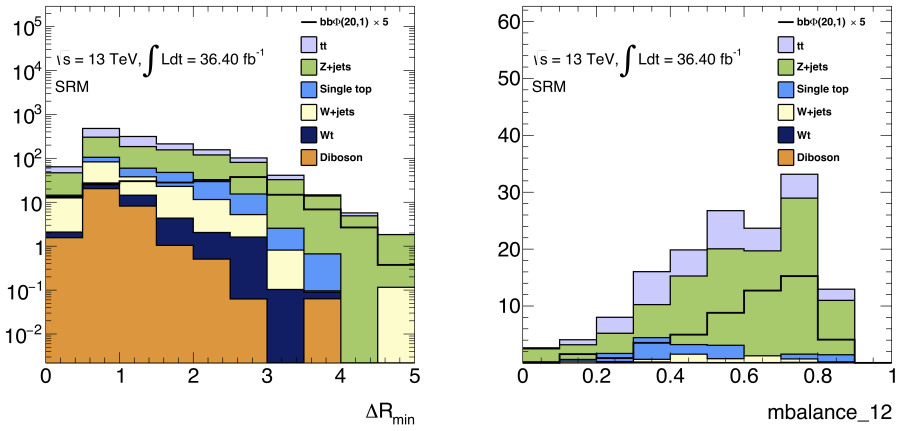

(a) ΔR_{min} **(b)** Jet Imbalance

Figure 5.9: Discriminating variables for SRM. For each distribution all cuts except the one showed in the plot are applied. Signal models with $m_\chi = 1\,\text{GeV}$ and $M_{med} = 20\,\text{GeV}$ have been considered with a cross section increased by a factor 5.

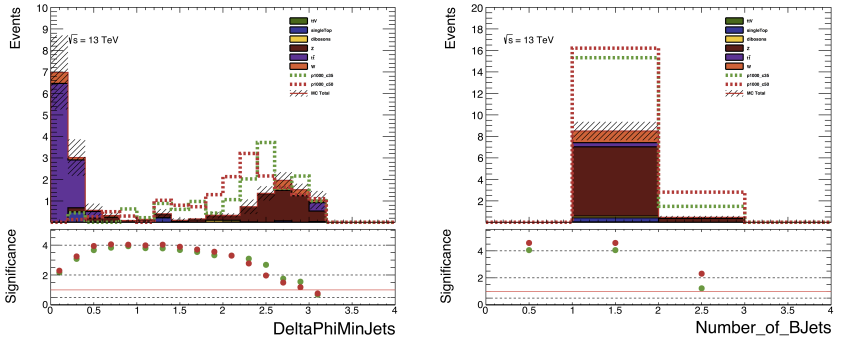

(a) $\mid \min \Delta\phi(j_i, E_{\mathrm{T}}^{\mathrm{miss}}) \mid i = 1, 2$

(b) $\mathcal{N}_{bjets}$

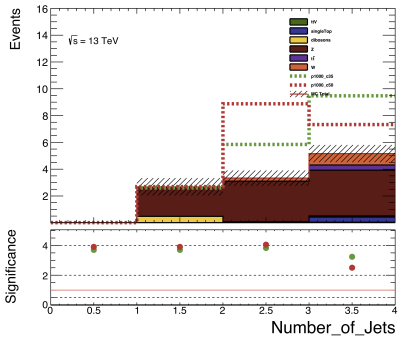

(c) $\mathcal{N}_{jets}$

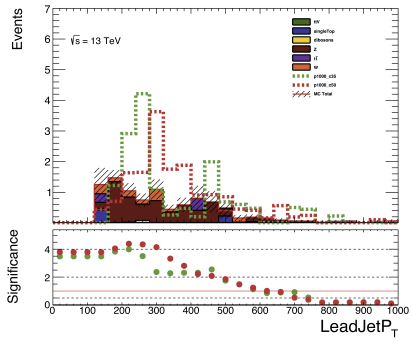

(d) Leading jet p_{T}

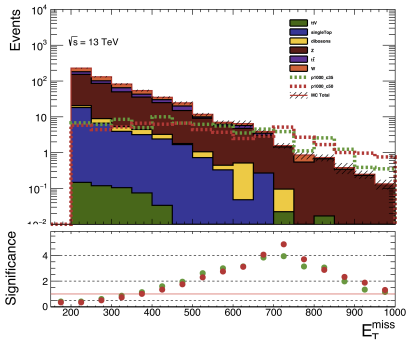

(e) $E_{\mathrm{T}}^{\mathrm{miss}}$

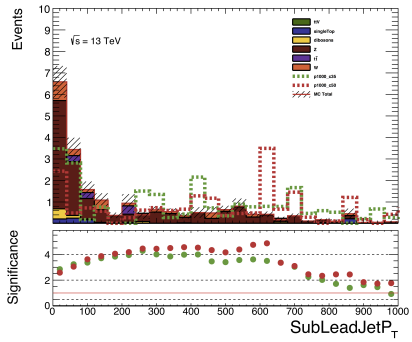

(f) Subleading jet p_{T}

Figure 5.10: N-1 plots for t-channel bFDM models in Signal Region targeting high mediator masses. All requirements of SRBFH are applied except for the one on the distribution shown in the figure. Only statistical uncertainties are shown in the plots. Signal models with $m_\chi = 35, 50\,\mathrm{GeV}$ and $M_{med} = 1000\,\mathrm{GeV}$ have been considered with a cross section increased by a factor 5.

5.4 Background estimation strategy

The impact of the major backgrounds has been performed by exploiting a semi-data-driven approach, in which Control Regions (CR) are defined. Each CR has been designed in order to obtain a region with a high purity of a specific background, that can be controlled by comparison to data samples. The *normalization factors* extrapolated from a simultaneous fit in all regions are used to rescale Monte Carlo predictions in the signal regions and account for cross contamination between control regions. Further information on fitting strategy are given in section 5.5.

5.4.1 s-channel background estimation

Background estimation for SRB

In the s-channel the main contribution corresponds to the irreducible background from $Z(\nu\nu)$ + jets events, since its topology is the same of the signal. This background is estimated in a two lepton dedicated control region, CRZB, where the selected leptons of $Z(\ell\ell)$ + jets events are treated as invisible particles in the $E_{\mathrm{T}}^{\mathrm{miss}}$ calculation. Further cuts are required to be as close as possible to the signal region to minimize extrapolation uncertainties, hence same b-tag multiplicities and similar angular cuts have been applied.
The second dominant background is $t\bar{t}$ production. These events are selected in SR mainly when leptonically W decay yields to a mis-identified lepton. A single lepton control region, denoted as CRTB, is designed for this purpose. In order to increase the purity of the control region a minimal requirement on the transverse mass of the neutrino-lepton system coming from W boson is required.
Finally W+jets , single top and diboson background, which give a minor contribution in signal region, are estimated from MC predictions.
Dedicated Validation Regions (VR) are defined to validate the normalization factors extrapolated from the fitting procedure before signal region data unblinding. A zero lepton validation region denoted as VRB2 is defined. The region has low signal contamination, with the same background composition as signal region whose orthogonality is ensured by reverting the y1 cut.
Table 5.8 reports all the requirements for SRB, CRs and VRs.

Background estimation for SRM

The background composition for this region is very similar to SRB. While $Z(\nu\nu)$ + jets events are estimated in a two lepton control region, CRZM, as for

Quantity	SRB	CRTB	CRZB	VRB2
Preselections	0-lep	1-lep	2-lep	0-lep
$\mathcal{N}_{jets}$	$2-3$	$2-3$	$2-3$	$2-3$
$\mathcal{N}_{bjets}$	≥ 2	≥ 2	≥ 2	≥ 2
Bjet 1 p_{T} [GeV]	> 150	> 150	> 150	> 150
jet 1 p_{T} [GeV]	> 150	> 150	> 150	> 150
jet 2 p_{T} [GeV]	> 20	> 20	> 20	> 20
jet 3 p_{T} [GeV]	< 60	< 60	< 60	< 60
$E_{\mathrm{T}}^{\mathrm{miss}}$ [GeV]	> 180	> 180	< 60	> 180
$E_{\mathrm{T}}^{\mathrm{miss}}$ (nolep) [GeV]	-	-	> 120	-
m_T^{lep}	-	> 30	-	-
$p_{\mathrm{T}}^{\mathrm{jet1}}/\mathrm{H_T}$	> 0.75	> 0.75	-	-
$x1$	< 0	< 0	< 1	< 0
$\lvert y1\rvert$	< 0.5	< 0.5	< 0.5	> 0.5

Table 5.8: Summary of the Control and Validation region selections for SRB. Preselection cuts refer to Tables 5.4a, 5.4b and 5.4c.

SRB approach, two different single lepton control regions have been designed according to b-jet multiplicity. A single lepton control region with two b-jet is defined for $t\bar{t}$ estimation denoted as CRTM, while for W+jets and single top backgrounds only one b-jet is required in CRWB definition.
Two validation regions are designed, one for a zero lepton selection, VRLR and the second for a single lepton selection with two b-jet requirement, VRWM. For both VRs orthogonality is ensured by reverting ΔR_{min} cut. All the CR and VR definitions are listed in Table 5.9.

5.4.2 t-channel background estimation

For b-FDM models $Z(\nu\nu) + \text{jets}$ is completely dominant and is the only background estimate from a control region designed with the same cuts as SR except a relaxed cut on $E_{\mathrm{T}}^{\mathrm{miss}}$ (nolep) in order to collect more statistics. It is not possible to define a VR for the high $E_{\mathrm{T}}^{\mathrm{miss}}$ phase space of the SR, given the smaller BR of $Z(\ell\ell)$ with respect to $Z(\nu\nu)$. The full selection list of this control region, denoted as CRZBFH is reported in Table 5.10.

5.4.3 Multi-jet background

Multi-jet background is due to mis-reconstructed jet energies in the calorimeters and to neutrinos present in the jet cone. The estimation of

Quantity	SRM	CRZM	CRWM	VRWM	CRTM	VRLR
Preselections	0-lep	2-lep	1-lep	1-lep	1-lep	0-lep
$\mathcal{N}_{jets}(\lvert\eta\rvert < 2.8)$	$2-3$	$2-3$	$2-3$	$2-3$	$2-3$	$2-3$
$\mathcal{N}_{\mathrm{b}jets}$	$= 2$	$= 2$	$= 1$	$= 2$	$= 2$	$= 2$
jet 1 p_{T} [GeV]	> 150	> 150	> 150	> 150	> 150	> 150
jet 2 p_{T} [GeV]	> 20	> 20	> 20	> 20	> 20	> 20
jet 3 p_{T} [GeV]	< 60	< 60	< 60	< 60	< 60	< 60
$E_{\mathrm{T}}^{\mathrm{miss}}$ [GeV]	> 180	< 80	> 180	> 180	> 180	> 180
$E_{\mathrm{T}}^{\mathrm{miss}}$ (nolep) [GeV]	-	> 180	-	-	-	-
ΔR_{min}	> 2.5	-	> 2.5	$[1.25, 2.5]$	> 2.5	$[2, 2.5]$
$\mathcal{I}(jw1, jw2)$	> 0.5	> 0.5	> 0.5	> 0.5	> 0.3	$[0.3, 0.5]$
m_T^{lep} [GeV]	-	-	$[30, 100]$	$[30, 100]$	> 30	-
$m_{\ell\ell}$	-	$[71, 111]$	-	-	-	-
lep 1 p_{T} [GeV]	-	> 30	> 30	> 30	> 30	-
lep 2 p_{T} [GeV]	-	> 25	-	-	-	-

Table 5.9: Summary of the selections which define control and validation regions for SRM. Preselection cuts refer to Tables 5.4a, 5.4b and 5.4c.

Quantity	SRBFH	CRZBFH
$\mathcal{N}_{\mathrm{b}jets}$	≥ 1	≥ 1
$\mathcal{N}_{jets}$	≥ 2	≥ 2
$E_{\mathrm{T}}^{\mathrm{miss}}$ [GeV]	> 650	< 120
$E_{\mathrm{T}}^{\mathrm{miss}}$ (nolep)	-	300
Jet 1 p_{T} [GeV]	> 160	> 160
Jet 2 p_{T} [GeV]	> 160	> 160
HT3	< 100	< 100
$\lvert \min \Delta\phi(j_i, E_{\mathrm{T}}^{\mathrm{miss}}) \rvert\ i = 1, 2$	> 0.6	-
$\lvert \min \Delta\phi(j_i, E_{\mathrm{T}}^{\mathrm{miss}}\,(\mathrm{nolep})) \rvert\ i = 1, 2$	-	> 0.6

Table 5.10: Control and signal region summary for the b-flavoured DM model SRBFH. In CRZBFH 2 lepton are required in the selection.

such background is evaluated with the *Jet Smearing* method which is based on the following procedure:

1. Events passing a defined set of cuts are selected and considered as *seed events*,

2. A jet response function R is built as the ratio

$$R = \frac{p_{\mathrm{T}}^{\mathrm{reco}}}{p_{\mathrm{T}}^{\mathrm{truth}}}, \tag{5.8}$$

   which is a map that compares truth and reco jet p_{T} for b-veto and b-tagged jets. "Pseudo-events" are generated by correcting each jet 4-momentum in a seed event for a random number extracted from the R map.

3. The smeared jets are rotated around z-axis to match di-jet data.

4. Variables of the pseudo-events are recalculated.

5. A multi-jet control region is defined, where normalization on pseudo-data is performed.

A control region with a loose SR-like selection and $\min \Delta\phi(j_i, E_{\mathrm{T}}^{\mathrm{miss}}) < 0.1$ is defined and the estimate is used to predict the amount of multi-jet events in SR, which is found to be negligible for the cut $\min \Delta\phi(j_i, E_{\mathrm{T}}^{\mathrm{miss}}) > 0.4$ applied in SR (Figure 5.11).

5.5 Fit strategy

The normalization factors extrapolated result from a fit to data which is based on CRs and SRs, each with a different Probability Density Function (PDF), successively combined into a simultaneous fit. All regions share the same PDF parameters thus providing consistent information from each signal and background component and systematics uncertainties. The strategy adopted is the following:

1. Fit CRs to normalize MC predictions to data.

2. *Transfer factors* (TF) extrapolated from CRs are then validated in VRs in order to estimate fitting procedure.

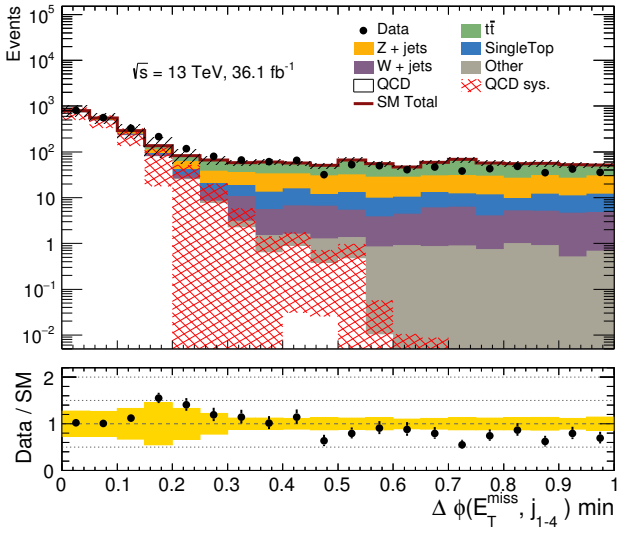

Figure 5.11: $\min \Delta\phi(j_i, E_{\mathrm{T}}^{\mathrm{miss}})_{i=1,2,3}$ at preselection level before a selection on the variable. The hashed area in the lower panel represents the uncertainty due to MC statistics and systematic uncertainty on the QCD (from JetSmearing) described in the text.

3. Backgrounds are extrapolated to SR to achieve final results. By convention the *unblinding* procedure, that is the comparison with observed data, is the final step of the analysis: once all previous steps are validated the unblinding is performed. This methodology avoids to introduce biases in the analysis.

The first two steps described above constitute the *Background-only* fit procedure. If we denote with N_p(region, est.) the background estimate of a process in a certain region and with N_p(region, in.) the expected background, the following relation is valid:

$$N_p(\text{SR, est.}) = \mu_p \times N_p(\text{SR, in.}), \tag{5.9}$$
$$N_p(\text{CR, est.}) = \mu_p \times N_p(\text{CR, in.}), \tag{5.10}$$

where μ_p is the normalization factor obtained from fit. Defining N_p(CR,fit) as the fitted number of the process p in the CR, the relation between SR and CR background estimation can be written as:

$$\begin{aligned} N_p(\text{SR, est.}) &= \mu_p \times N_p(\text{SR, in.}) \\ &\equiv N_p(\text{CR, fit}) \times \left[\frac{N_p(\text{SR, in.})}{N_p(\text{CR, in.})}\right]. \end{aligned} \tag{5.11}$$

The ratio in the square brackets is the transfer factor. Being defined as a ratio, systematics uncertainties on the predicted background can be cancelled in the extrapolation: background uncertainties in the SR are a combination of statistical uncertainties in the CR and residual systematic uncertainties from the extrapolation. As a consequence usually CRs are defined with a kinematic as close as possible to the SR to avoid large uncertainties coming from extrapolation and with a larger statistics.
The PDF contains the normalization factors obtained from data, the rate of a signal process and the systematic uncertainties (described by the *nuisance parameters*). The corresponding likelihood is the product of Poisson distribution in each region considered and an additional distribution for the systematic uncertainties:

$$\begin{aligned} L(\boldsymbol{n}, \boldsymbol{\theta}^0 | \mu_{\text{sig}}, \boldsymbol{\mu_p}, \boldsymbol{\theta}) &= P_{\text{SR}} \times P_{\text{CR}} \times C_{\text{syst}} \\ &= \prod_{i \in \text{SR}} P(n_i | \lambda_S(\mu_{\text{sig}}, \boldsymbol{\mu_p}, \boldsymbol{\theta})) \times \prod_{i \in \text{CR}} P(n_i | \lambda_i(\mu_{\text{sig}}, \boldsymbol{\mu_p}, \boldsymbol{\theta})) \\ &\times C_{\text{syst}}(\boldsymbol{\theta}^0, \boldsymbol{\theta}) \,, \end{aligned} \tag{5.12}$$

where P_{SR} and P_{CR} are Poisson distributions of the observed events. The number of observed events in a region in the i-th bin is n_i with expectation λ_i which is function of the normalization factors, the signal strength μ_{sig} and nuisance parameters $\boldsymbol{\theta}$ that parametrize systematics uncertainties. The function $C_{\text{syst}}(\boldsymbol{\theta}^0, \boldsymbol{\theta})$, usually a Gaussian probability density function with mean zero, constrains nuisance parameters. The signal strength equals to zero means no signal contribution; when $\mu_{\text{sig}} = 1$ the signal corresponds to the expected number of events of the considered model.
As mentioned before the background only-fit is performed only on CR in order to extrapolate transfer factors, the SR term of equation 5.12 is not considered in the likelihood. The full likelihood is built in a model-independent signal fit, where the purpose is to set an upper limit on the signal cross sections. A profile likelihood ratio test statistic is computed in both fitting approaches, the CL_{S} method is used to derive exclusion limits for signal models with a given confidence level. The fitting is performed using the HistFitter package [68].

Fit strategy for SRB and SRM

In order to increase the discovery potential a shape-fit on $\cos\theta^*$ as discriminating variable has been performed for SRB and SRM regions. The fit strategy implemented is based on a simultaneous shape fit where signal region is binned in $\cos\theta^*$. The shape information is hence considered and a

single TF from each CR is extrapolated. In order to avoid any source of bias signal region selections does not include any cut on variables that could be correlated to the discriminating variable. The choice of the binning has been optimized to avoid large statistical uncertainties, thus resulting in a 4 bin division, with $0 < \cos\theta^* < 1$.

Fit strategy for SRBFH

This signal region selects few events and hence has been optimized for a cut-and-count selection: no shape information has been exploited.

5.6 Systematic Uncertainties

Systematics uncertainties give a measure of the impact of experimental and theoretical uncertainties to the final result. For the shape fit approach each systematic uncertainty is considered fully correlated across the bins of the discriminating variable. In addition, a normalisation and a shape component have been considered for all backgrounds which are not normalized in CRs while for backgrounds estimated in CRs the total normalisation uncertainty is not considered since is taken into account by the normalisation factor.
A statistical uncertainties related to MC statistics is also considered.

5.6.1 Experimental uncertainties

Luminosity and pile-up

The integrated luminosity measured in data has an uncertainties estimated in a 3.2% for the combined 2015-2016 dataset and taken into account for MC normalization. In order to evaluate differences between data and MC after pile-up a proper systematics is considered by varying pile-up scaling with respect to the nominal value.

Jet, b-jet and $E_{\mathrm{T}}^{\mathrm{miss}}$

Jet energy scale (JES) and jet energy resolution (JER) are evaluated by in-situ studies. A smearing to jet p_{T} is performed on jets according to their p_{T} and η in order to take into account a possible underestimation of the JER. b-tagging uncertainties are evaluated by up/down variation on scale factor uncertainty for b-, c-, light jets and extrapolations. This uncertainty is expected to be independent of the jet multiplicity.
$E_{\mathrm{T}}^{\mathrm{miss}}$ systematics accounts for the $E_{\mathrm{T}}^{\mathrm{miss}}$ track soft term scale and resolution

uncertainties. It should be noted that JES and JER effects are also propagated to $E_{\mathrm{T}}^{\mathrm{miss}}$.

Leptons

These sources of systematics are related to lepton identification efficiency scale factor and momentum or energy scale and resolution by performing an up/down variation of these parameters.

5.6.2 Theoretical systematics

V+jets

Theoretical systematic uncertainties on V+jets are evaluated by varying a set of parameters fixed in generation phase for SHERPA, samples. These parameters are:

- Matrix element matching (ckkw): this is the merging scale, with a nominal value of 20 GeV , the variations go down to 15 GeV and up to 30 GeV .
- Renormalisation scale (renorm): it's a variation on the scale for the running strong coupling constant. The varied values wit respect to nominal one are 2 and 1/2.
- Factorisation scale (fac): variation on the scale for the parton density functions, it's fixed to 2 and 1/2 with respect to nominal value.
- Resummation scale (qsf): varies the scale used for the resummation of soft gluon emission. 2 and 1/2 are the varied values.

The corresponding weights are calculated from binned boson p_{T} and jet multiplicities map distributions for each SHERPAsample as the ratio of the number of events in the sample with up/down varied parameter over the nominal number of events:

$$w_{i,j} = \frac{N_{i,j}^{\mathrm{Syst}}}{N_{i,j}^{\mathrm{Nomonal}}}. \tag{5.13}$$

The impact of each V+jets systematic is evaluated by computing the up/down yields variation of $\cos\theta^*$distribution with respect to nominal (Nom) as follows:

$$\Delta = \frac{(Sys_{\mathrm{High}} - Sys_{\mathrm{Low}})}{2 \times \mathrm{Nom}} \tag{5.14}$$

The results are shown in Table 5.11 and 5.12, for the control, validation and signal B-regions. CRZB is missing for the W+jets uncertainty as this background's yield in 2-lep selections is zero.

SRB Variation	Δ	Δ $\cos\theta^*$ $[0, 0.25]$	Δ $\cos\theta^*$ $[0.25, 0.5]$	Δ $\cos\theta^*$ $[0.5, 0.75]$	Δ $\cos\theta^*$ $[0.75, 1]$
CKKW	0.064	0.066	0.064	0.062	0.064
Fac. Scale	-0.019	-0.020	-0.019	-0.019	-0.020
Ren. Scale	-0.125	-0.123	-0.133	-0.130	-0.114
QSF	-0.065	-0.064	-0.064	-0.066	-0.067

CRZB Variation	Δ
CKKW	0.059
Fac. Scale	-0.031
Ren. Scale	-0.179
QSF	-0.060

CRTB Variation	Δ
CKKW	0.077
Fac. Scale	-0.027
Ren. Scale	-0.120
QSF	-0.051

VRB Variation	Δ
CKKW	0.073
Fac. Scale	-0.017
Ren. Scale	-0.193
QSF	-0.060

Table 5.11: Z+jets theoretical uncertainties: Variations in SRB regions. Values are provided for the inclusive and per-bin $\cos\theta^*$distribution.

Top

Single top and $t\bar{t}$ uncertainties are the following:

- Cross section: for $t\bar{t}$ are not relevant in the analysis as consequence of using a dedicated CR. For single top cross section uncertainty is taken into account.
- MC generator/hard scatter: a comparison between different generators has been done. The differences are symmetrized and statistical uncertainties added in quadrature.

SRB Variation	Δ	Δ $\cos\theta^*$ $[0, 0.25]$	Δ $\cos\theta^*$ $[0.25, 0.5]$	Δ $\cos\theta^*$ $[0.5, 0.75]$	Δ $\cos\theta^*$ $[0.75, 1]$
CKKW	0.040	0.036	0.041	0.053	0.024
Fac. Scale	-0.032	-0.032	-0.033	-0.032	-0.032
Ren. Scale	-0.181	-0.187	-0.171	-0.172	-0.209
QSF	-0.041	-0.043	-0.038	-0.045	-0.032

CRTB Variation	Δ
CKKW	0.040
Fac. Scale	-0.035
Ren. Scale	-0.209
QSF	-0.035

VRB Variation	Δ
CKKW	0.052
Fac. Scale	-0.032
Ren. Scale	-0.208
QSF	-0.039

Table 5.12: W+jets theoretical uncertainties: Variations in SRB regions.

- Additional radiation, fragmentation and hadronization evaluated by comparing different samples and taking the difference as uncertainty.

Diboson

Only expected MC yields are used for diboson hence the uncertainties include only the full cross section uncertainty of 7%.

Signal

Several source of systematic uncertainties have been taken into account for the signal models, namely factorisation and normalisation scale, uncertainty related to the merging of the matrix element and the parton shower as well as the choice of the parton shower tune and the choice of the pdf.

5.7 Results

5.7.1 Background only fits

The background estimation in SRs and VRs has been performed through a background only fit strategy. In this procedure the background prediction obtained from data are independent of the observed number of events in SRs and VRs, since only CRs are used, thus ensuring an unbiased comparison between observed and expected events in each region. All the results are obtained with the full Run-2 statistics of $36.1\,\text{fb}^{-1}$. All systematics described in Section 5.6 are included in the fit.

SRB background only fit

The results for the background only fit in control and validation regions are shown in Table 5.13 and the extrapolated yields in SRB in Table 5.14. The two fitted normalization factors are:

- $\mu_{t\bar{t}} = 0.66 \pm 0.12$
- $\mu_Z = 1.29 \pm 0.29$.

The distributions of $\cos\theta^*$ after background has been rescaled are shown in Figure 5.12 for each CR and VR.

	CRZB	CRTB	VRB2
Observed	161	129	194
Fitted bkg	160.93 ± 12.66	129.19 ± 11.36	179.51 ± 20.35
Fitted Zjets	147.30 ± 14.36	0.20 ± 0.07	102.13 ± 14.95
Fitted Wjets	0.00 ± 0.00	7.00 ± 4.11	19.13 ± 12.27
Fitted ST	1.19 ± 1.18	24.60 ± 7.75	20.57 ± 6.18
Fitted ttbar	11.35 ± 7.90	97.12 ± 14.83	35.29 ± 8.89
Fitted Others	1.09 ± 0.83	0.28 ± 0.15	2.39 ± 1.46
MC exp. SM	133.17 ± 24.97	180.07 ± 17.02	174.76 ± 26.42
MC exp. Zjets	113.52 ± 22.92	0.15 ± 0.06	78.66 ± 20.07
MC exp. Wjets	0.00 ± 0.00	7.04 ± 4.13	19.22 ± 12.33
MC exp. ST	1.20 ± 1.19	24.70 ± 7.81	20.65 ± 6.21
MC exp. ttbar	17.35 ± 10.18	147.90 ± 11.86	53.82 ± 8.78
MC exp. Others	1.10 ± 0.83	0.28 ± 0.15	2.42 ± 1.47

Table 5.13: Background only fits in the CRs relative to the SRB selections and extrapolated yields in the validation region. All systematic uncertainties except muon and electron scales are included.

	SRB_bin0	SRB_bin1	SRB_bin2	SRB_bin3
Observed	-	-	-	-
Fitted bkg	77.28 ± 12.81	71.79 ± 11.34	75.61 ± 12.70	66.35 ± 9.18
Fitted Zjets	39.59 ± 6.31	44.36 ± 6.65	53.29 ± 9.88	55.55 ± 8.58
Fitted Wjets	4.90 ± 3.95	3.31 ± 2.27	2.73 ± 1.72	0.99 ± 0.95
Fitted ST	14.71 ± 5.83	10.18 ± 3.72	5.51 ± 3.14	2.56 ± 1.67
Fitted ttbar	17.79 ± 6.49	13.89 ± 5.59	14.09 ± 4.78	6.97 ± 2.90
Fitted Others	$0.29^{+0.32}_{-0.29}$	$0.05^{+0.10}_{-0.05}$	0.00 ± 0.00	0.28 ± 0.22
MC exp. SM	77.61 ± 14.52	68.83 ± 12.54	70.71 ± 13.13	57.31 ± 9.08
MC exp. Zjets	30.57 ± 6.15	34.21 ± 6.74	41.07 ± 9.51	42.84 ± 7.99
MC exp. Wjets	4.92 ± 3.96	3.32 ± 2.28	2.74 ± 1.73	1.00 ± 0.95
MC exp. ST	14.74 ± 5.86	10.18 ± 3.72	5.50 ± 3.13	2.57 ± 1.68
MC exp. ttbar	27.08 ± 8.20	21.07 ± 6.93	21.41 ± 6.45	10.62 ± 3.85
MC exp. Others	$0.30^{+0.32}_{-0.30}$	$0.05^{+0.10}_{-0.05}$	0.00 ± 0.00	0.28 ± 0.22

Table 5.14: SRB extrapolated yields from the background only fit in the control regions, divided per bin. All major systematic uncertainties are included.

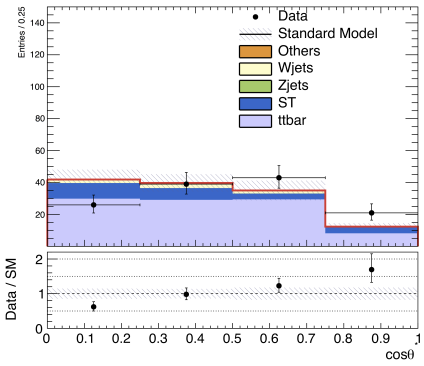

(a) CRTB

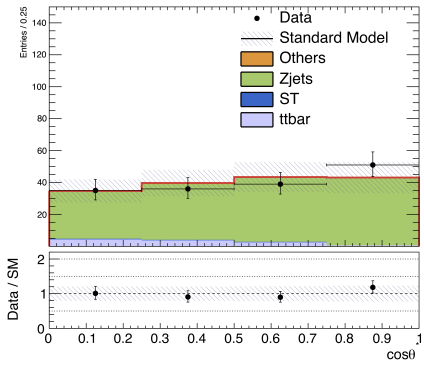

(b) CRZB

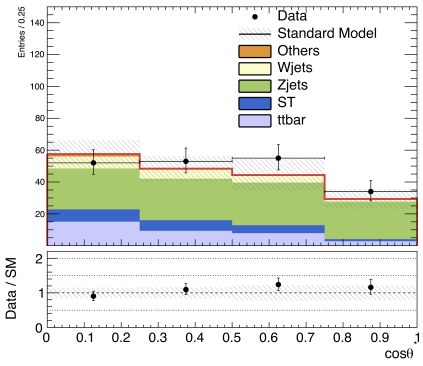

(c) VRB2

Figure 5.12: $\cos\theta^*$ distributions for CRB and VRB regions after background only fits. All systematics described in Section 5.6 have been included in the shaded band.

SRM background only fit

As cross check to SRB, a background only-fit for SRM was performed. The three normalization factors obtained are:

- $\mu_{t\bar{t}} = 0.91 \pm 0.28$
- $\mu_W = 1.06 \pm 0.26$
- $\mu_Z = 1.28 \pm 0.44$

while pre and post-fit yields are listed in Table 5.15 for each control and validation regions and in Table 5.16 for SR. After fit $\cos\theta^*$ distributions are shown in Figure 5.12.

	CRWM	CRTM	CRZM	VRWM	VRLR
Observed events	313	115	109	111	71
Fitted bkg events	312.91 ± 17.64	114.96 ± 10.68	108.95 ± 10.37	109.85 ± 12.95	68.98 ± 7.16
Fitted Zll_0 events	1.82 ± 0.49	0.40 ± 0.12	98.90 ± 10.67	0.04 ± 0.01	36.79 ± 5.13
Fitted Wlnu_0 events	134.96 ± 19.68	3.93 ± 1.11	0.00 ± 0.00	17.70 ± 3.96	3.62 ± 1.65
Fitted ttbar_0 events	79.94 ± 15.38	94.00 ± 12.70	8.00 ± 2.08	57.49 ± 9.27	16.95 ± 3.32
Fitted Wt_0 events	12.78 ± 3.39	3.58 ± 1.32	2.06 ± 0.96	5.69 ± 1.59	0.29 ± 0.29
Fitted singletop_0 events	80.16 ± 17.21	13.05 ± 4.22	0.00 ± 0.00	28.49 ± 7.60	11.10 ± 3.65
Fitted diboson_0 events	3.26 ± 1.12	0.00 ± 0.00	0.00 ± 0.00	0.44 ± 0.33	0.23 ± 0.12
MC exp. SM events	307.17 ± 65.66	122.76 ± 32.06	87.90 ± 28.03	112.42 ± 29.24	61.67 ± 17.90
MC exp. Zll_0 events	1.42 ± 0.63	0.31 ± 0.10	77.20 ± 24.73	0.03 ± 0.00	28.72 ± 8.49
MC exp. Wlnu_0 events	127.22 ± 38.01	3.70 ± 1.28	0.00 ± 0.00	16.68 ± 5.07	3.41 ± 2.03
MC exp. ttbar_0 events	87.67 ± 18.25	103.07 ± 27.27	8.77 ± 3.49	63.05 ± 18.50	18.58 ± 5.96
MC exp. Wt_0 events	12.04 ± 3.01	3.37 ± 1.53	1.94 ± 1.02	5.36 ± 1.57	0.27 ± 0.24
MC exp. singletop_0 events	75.56 ± 18.54	12.30 ± 3.99	0.00 ± 0.00	26.86 ± 6.21	10.45 ± 3.48
MC exp. diboson_0 events	3.25 ± 1.14	0.00 ± 0.00	0.00 ± 0.00	0.44 ± 0.33	0.23 ± 0.12

Table 5.15: Background only fits in the CRs relative to the SRM selections and extrapolated yields in the validation region. All systematic uncertainties except muon and electron scales are included.

	SRM_0	SRM_25	SRM_50	SRM_75	SRM
Observed events	–	–	–	–	–
Fitted bkg events	16.57 ± 2.98	23.19 ± 3.74	42.57 ± 6.20	99.90 ± 12.82	182.2 ± 21.0
Fitted Zll events	7.38 ± 1.37	13.31 ± 2.58	29.96 ± 4.92	86.98 ± 11.39	137.6 ± 17.9
Fitted Wlnu events	1.06 ± 0.57	1.32 ± 0.73	1.77 ± 0.86	1.35 ± 1.20	5.5 ± 2.7
Fitted ttbar events	6.18 ± 2.73	4.62 ± 1.71	7.96 ± 2.04	6.29 ± 1.99	25.1 ± 6.4
Fitted Wt events	0.04 ± 0.02	0.39 ± 0.19	0.09 ± 0.06	1.17 ± 0.76	1.7 ± 0.9
Fitted singletop events	1.79 ± 0.79	3.40 ± 1.28	2.79 ± 1.91	4.09 ± 2.07	12.1 ± 5.3
Fitted diboson events	0.12 ± 0.11	0.13 ± 0.10	0.00 ± 0.00	0.02 ± 0.01	0.3 ± 0.2
MC exp. SM events	15.38 ± 3.98	20.42 ± 6.02	36.48 ± 12.31	81.02 ± 28.05	153.30 ± 48.48
MC exp. Zll events	5.76 ± 2.03	10.39 ± 3.69	23.38 ± 8.23	67.89 ± 22.93	107.42 ± 36.04
MC exp. Wlnu events	0.99 ± 0.60	1.25 ± 0.75	1.67 ± 0.94	1.27 ± 1.07	5.18 ± 2.69
MC exp. ttbar events	6.79 ± 2.30	5.07 ± 1.85	8.73 ± 2.85	6.89 ± 3.33	27.47 ± 8.27
MC exp. Wt events	0.03 ± 0.02	0.37 ± 0.18	0.08 ± 0.06	1.10 ± 0.77	1.59 ± 0.94
MC exp. singletop events	1.69 ± 0.85	3.21 ± 1.16	2.63 ± 1.81	3.85 ± 2.26	11.37 ± 5.45
MC exp. diboson events	0.12 ± 0.11	0.13 ± 0.10	0.00 ± 0.00	0.02 ± 0.01	0.26 ± 0.19

Table 5.16: SRM extrapolated yields from the background only fit in the control regions. Both per-bin and inclusive values are reported. All major systematic uncertainties are included.

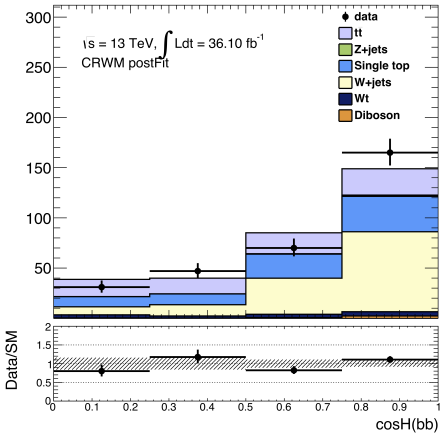

(a) CRWB

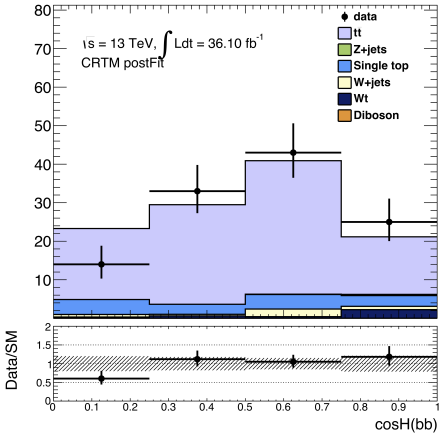

(b) CRTB

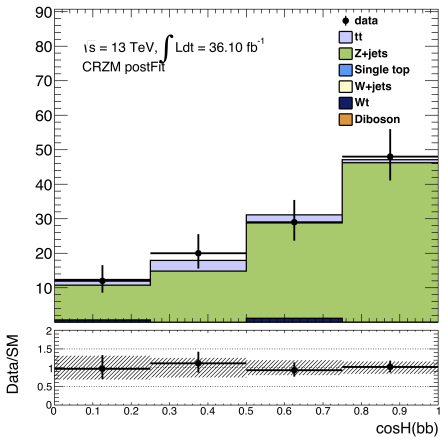

(c) CRZB

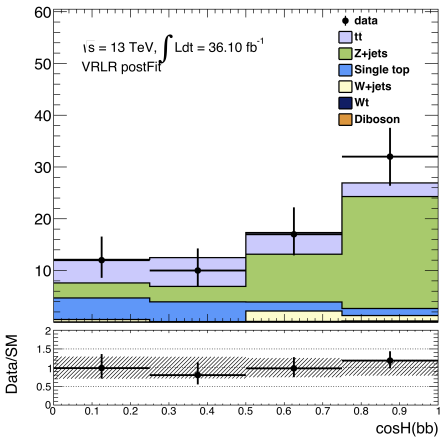

(d) VRLR

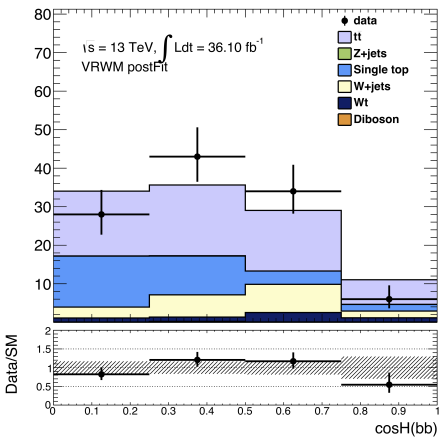

(e) VRWM

Figure 5.13: $\cos\theta^*$ distributions after background only fits.

SRBFH

For b-FDM only Z+jets background has been fitted, giving a normalisation factor of

- $\mu_Z = 1.17 \pm 0.18$.

Table 5.17 reports fit results and the background extrapolation to the SR. $E_{\mathrm{T}}^{\mathrm{miss}}$ distribution after fit is shown in Figure 5.14.

	SRBFH	CRZBFH
Observed	–	–
Fitted bkg	16.94 ± 5.21	47.98 ± 6.92
Fitted Zjets	14.16 ± 5.12	46.25 ± 6.97
Fitted Wjets	1.25 ± 0.82	0.00 ± 0.00
Fitted ST	$0.25^{+0.42}_{-0.25}$	$0.34^{+0.43}_{-0.34}$
Fitted ttbar	0.58 ± 0.17	0.25 ± 0.01
Fitted Others	0.71 ± 0.53	1.14 ± 0.72
MC exp. SM	14.89 ± 4.10	41.31 ± 1.73
MC exp. Zjets	12.11 ± 3.98	39.58 ± 1.42
MC exp. Wjets	1.24 ± 0.82	0.00 ± 0.00
MC exp. ST	$0.25^{+0.43}_{-0.25}$	$0.35^{+0.43}_{-0.35}$
MC exp. ttbar	0.58 ± 0.17	0.25 ± 0.01
MC exp. Others	0.70 ± 0.54	1.13 ± 0.73

Table 5.17: Background only fit results for SRBFH. Total integrated luminosity is $36.1\,\mathrm{fb}^{-1}$. Statistical uncertainties only are included.

5.7.2 Limits

s-channel limits

In the absence of a signal excess over expected backgrounds, the results can be interpreted in terms of upper limits on the production cross section of BSM Physics. The signal-plus-background hypothesis for a specific signal models can be excluded by using a profile likelihood ratio test statistics, and CL_S method is used to derive the confidence level of the exclusion limits: signal models whose CL_S value are below 0.05 are excluded at 95% CL. The quantity used is the signal strength ($\sigma_{\mathrm{excl}}/\sigma(g)$), which is the scaling factor

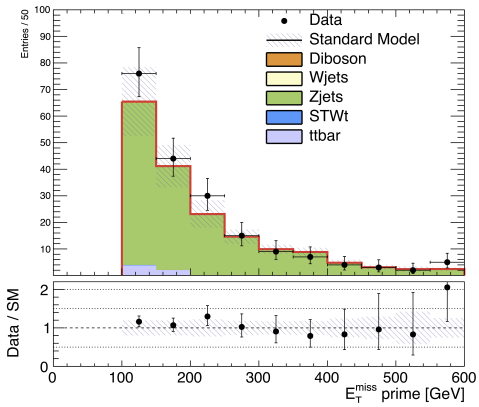

Figure 5.14: Corrected $E_{\mathrm{T}}^{\mathrm{miss}}$ distribution in CRZBFH, where the corrected $E_{\mathrm{T}}^{\mathrm{miss}}$ requirement is relaxed to 100 GeV. All systematics described in Section 5.6 are included in the shaded band.

to be applied to the theoretical cross section of the signal model analysed in order to exclude it at 95% CL. Upper limits are obtained as a function of mediator mass, with mediator (scalar or pseudoscalar) decaying in a DM pair, for a fixed choice of the coupling and DM mass.
For the s-channel analysis, observed limits are available for a dataset corresponding to $13.3\,\mathrm{fb}^{-1}$ for both scalar and pseudoscalar mediator, assuming $m_\chi = 1\,\mathrm{GeV}$ and equal couplings $g_q = g_\chi = 1.0$ as shown in Figure 5.15. The selection criteria used for derive this results are described in Appendix B. Expected limits at $36.1\,\mathrm{fb}^{-1}$ for SRB and SRM are respectively shown in Figure 5.16 and 5.17 with the same assumption described above. Finally a comparison between the results obtained for SRB, SRM and $13.3\,\mathrm{fb}^{-1}$ data are shown Figure 5.18 for both scalar and psudoscalar mediator. As expected, the increasing luminosity and the employment of shape information lead to a significant improvement of upper limits with respect to the results obtained in [67]. Although SRM gives similar results as SRB, the latter is best performing for the largest parameter space, validating the choice of using it as nominal selection in the analysis.

b-FDM limits

The results for b-FDM models are interpreted as contour exclusion plot in the $M_{med} - m_\chi$ plane, as shown in Figure 5.19. The behaviour at $m_\chi = 100\,\mathrm{GeV}$ is due to the fact that DM masses above 100 GeV have not been generated, as the interest for this model was driven by the Galactic Center Excess and therefore was focused around $m_\chi = 35$ GeV. The observed value

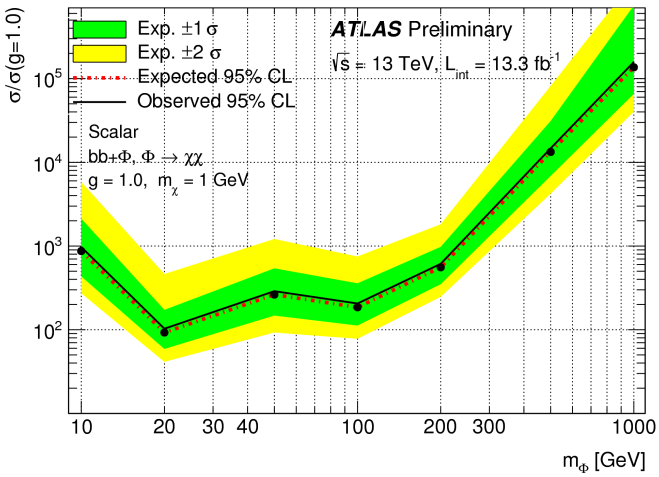

(a) Scalar mediator

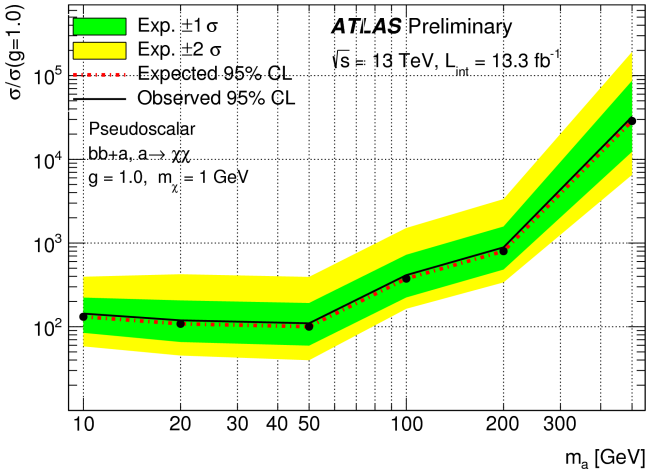

(b) Pseudoscalar mediator

Figure 5.15: Cross section limits obtained for the s-channel analysis with $13.3\,\text{fb}^{-1}$ of data. The dashed red line indicated the expected limits, the solid black line the observed ones [67].

(solid red line) refers to blind pre-fit expected MC yields and it has not been derived from observed data.

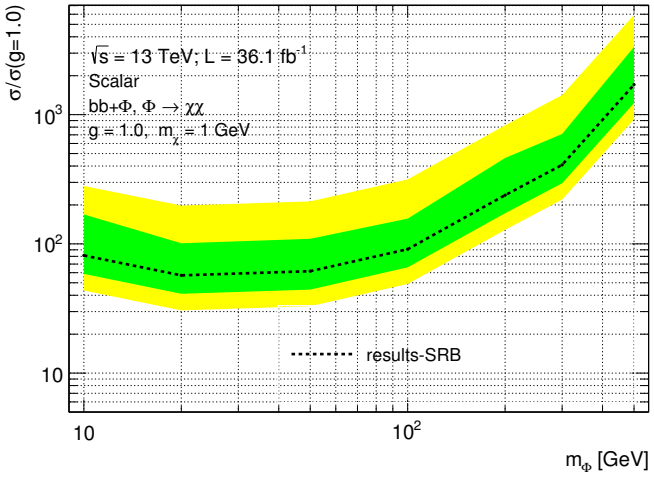

(a) Scalar mediator

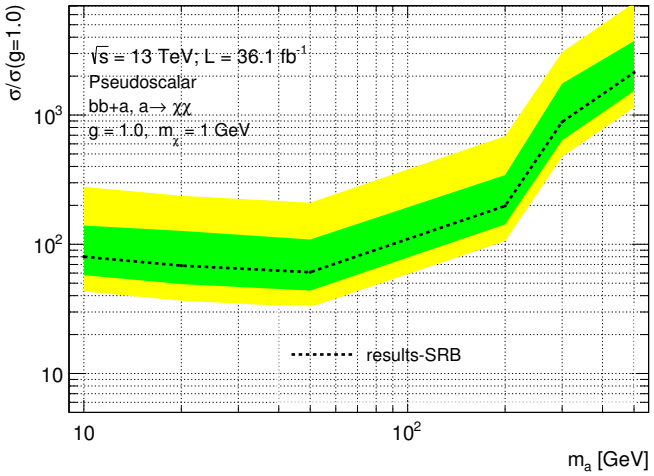

(b) Pseudoscalar mediator

Figure 5.16: Expected cross section limits obtained for SRB. The systematics described in Section 5.6 (both theory and detector) are included in the fit.

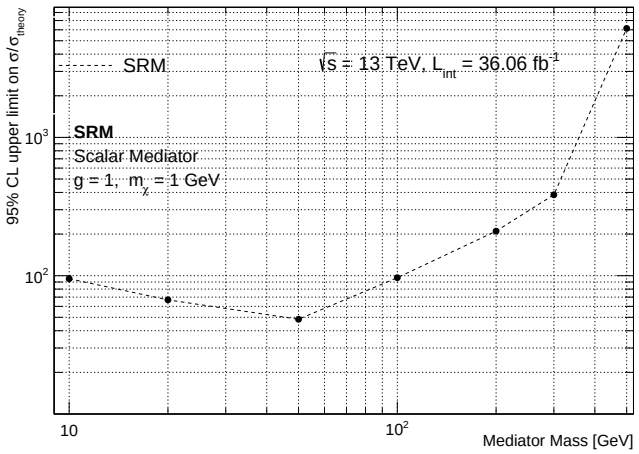

(a) Scalar mediator

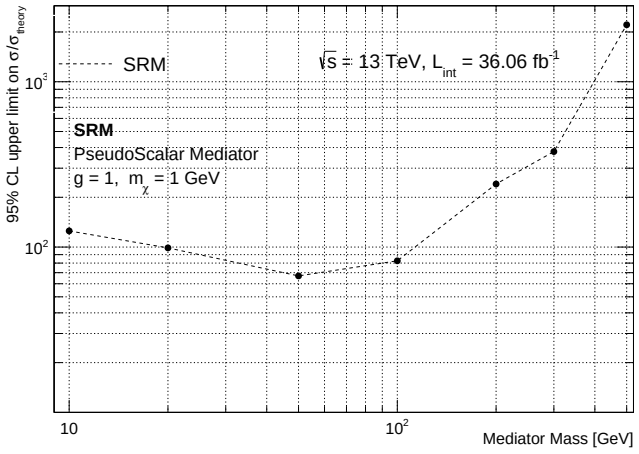

(b) Pseudoscalar mediator

Figure 5.17: Expected cross section limits obtained for SRM for DM scalar (a) and pseudoscalar (b) mediators with a DM mass of 1 GeV. The systematics described in Section 5.6 (both theory and detector) are included in the fit.

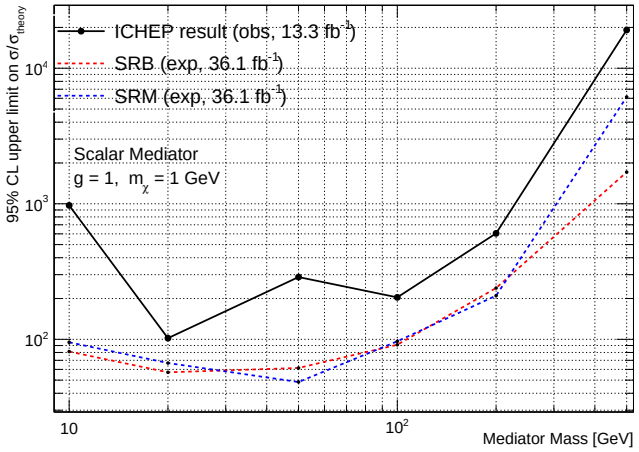

(a) Scalar mediator

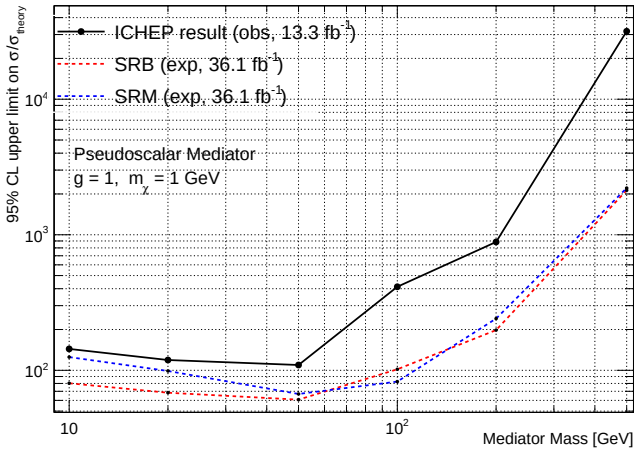

(b) Pseudoscalar mediator

Figure 5.18: Comparison between limits obtained with observed results with 13.3 fb^{-1} data (solid black line) [67] and SRB (dashed red line) and SRM (dashed blue line) expected results for DM scalar (a) and pseudoscalar (b) mediators with a DM mass of 1 GeV.

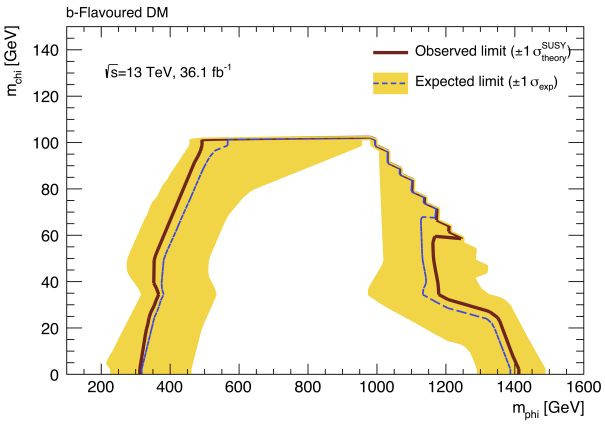

Figure 5.19: Final limit contour for b-FDM models including all major systematics. Mediator masses below 400 GeV are not interesting for this search as they have already been excluded by sbottom analysis and DM masses above 100 GeV have not been generated.

Chapter 6

Summary of Dark Matter analyses

The DM programme at LHC involves several analyses, each one sensitive to a particular simplified model, as described in section 2.4.4. In order to place the search with bottom quarks in a context with a wider description of DM searches, a brief overview on the other analyses will be described in this chapter as well as the possibility to combine them in the direction of achieving more performing results.

6.1 DM production in association with $t\bar{t}$

As for bottom quarks, dedicated DM analyses involving final states with top pairs can probe information about scalar and pseudoscalar spin-0 mediators. As such interactions occur via Yukawa coupling, final states with top quarks are privileged, and higher cross sections with respect to bottom quarks allow to achieve better limits on the models studied.
Depending on top decay, which can be hadronic, semileptonic or leptonic three corresponding signatures have been considered: with no leptons in the final state, with one and two leptons. The results that will be shown correspond to a dataset of $13.3\,\text{fb}^{-1}$ collected at $\sqrt{s} = 13$ TeV.
Upper limits at 95% CL are set in a $M_{med} - m_{\chi}$ plane, where $M_{med} = m_{\phi}$, m_a for scalar and pseudoscalar scenario, for a given choice of the couplings. For DM + $t\bar{t}$ analyses the choice adopted is $g = g_{\chi} = g_q = 3.5$, which provides the scenario with the highest cross sections (~ 10 times higher than the cross sections with $g = g_{\chi} = g_q = 1$). The most sensitive region is expected to correspond to the part of the plane where mediator is on-shell ($M_{med} > 2m_{\chi}$) and low DM masses.

0 lepton analysis

The signal region for this analysis [69] has been optimized for a model with $M_{med} = 350\,\text{GeV}$ and $m_\chi = 1$ GeV: at least four jets are selected, two of which must be b-tagged. The most powerful discriminating variables are $m_T^{b,\min}$ (the transverse mass calculated from $E_{\text{T}}^{\text{miss}}$ and the b-jets closest in ϕ to the missing transverse energy direction) useful to reject $t\bar{t}$ background and a jet reclustered variable with distance parameter $R = 1.2$, with $m_{\text{jet}}^0 > 140\,\text{GeV}$ and $m_{\text{jet}}^1 > 60\,\text{GeV}$, where m indicates the mass of leading and subleading jet. Additional cuts on $E_{\text{T}}^{\text{miss}}$, $E_{\text{T}}^{\text{miss}}/\sqrt{H_T}$ and $\Delta R(b,b)$ are applied.
$Z(\nu\nu)+\text{jets}$, $t\bar{t}$, W+jets and single top events constitute the major backgrounds and have been studied from data in dedicated control regions. A simultaneous fit has been applied in order to determine all SM contributions, which includes theoretical and experimental systematic uncertainties.
The results are interpreted as exclusion limits at 95% CL in the $M_{med} - m_\chi$ plane, for $g = g_\chi = g_q = 3.5$, as shown in Figure 6.1, where the numbers in the contour plot indicate the limits on the coupling.

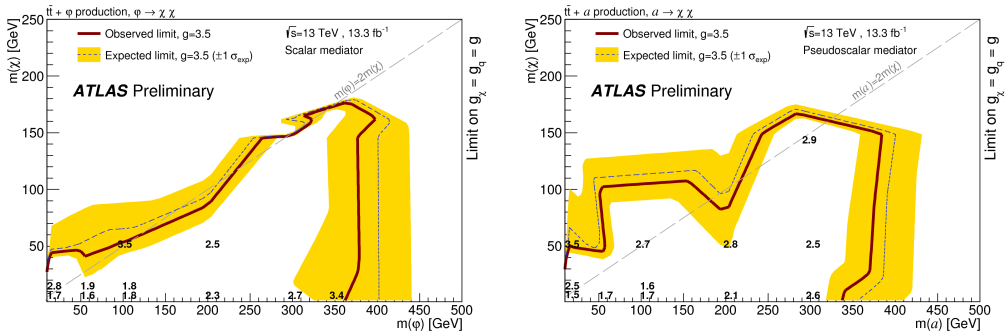

(a) Scalar mediator **(b)** Pseudoscalar mediator

Figure 6.1: Exclusion limits at 95% CL in the $M_{med} - m_\chi$ plane with $g = 3.5$ for the DM+$t\bar{t}$ model with no lepton in the final state [69]. Expected (observed) contour plot corresponds to the blue dashed (red solid) line.

1 Lepton analysis

This analysis targets final states with one lepton, with one W boson from top decaying leptonically. Two signal regions have been developed, DM_low and DM_high, both using angular and kinematic cuts, as described in detail in [70]. Top quark pair, W+jets and single top backgrounds are estimated

from data in three corresponding enriched control regions. The irreducible background of the analysis, namely $t\bar{t}$ events produced in association with a Z boson decaying into neutrinos can not be evaluated in a CR using Z boson since the small branching ratio of Z decaying into leptons and the limited dataset available. For this purpose a data-driven approach using $t\bar{t}+\gamma$ events has been exploited, considering a control region developed in such a way to avoid significant kinematic differences between the two processes and reduce theoretical uncertainties in the extrapolation. Deviations from SM expectations corresponding respectively to $3.3\,\sigma$ and $1.3\,\sigma$ have been observed in DM_low and DM_high SRs, and the 95% CL upper limits in the in the $M_{med} - m_\chi$ plane are shown in Figure 6.2. For a maximum coupling $g = g_\chi = g_q = 3.5$ the mediator masses (both for scalar and psudoscalar) excluded for $Mdm = 1\,\text{GeV}$ are up to 350 GeV.

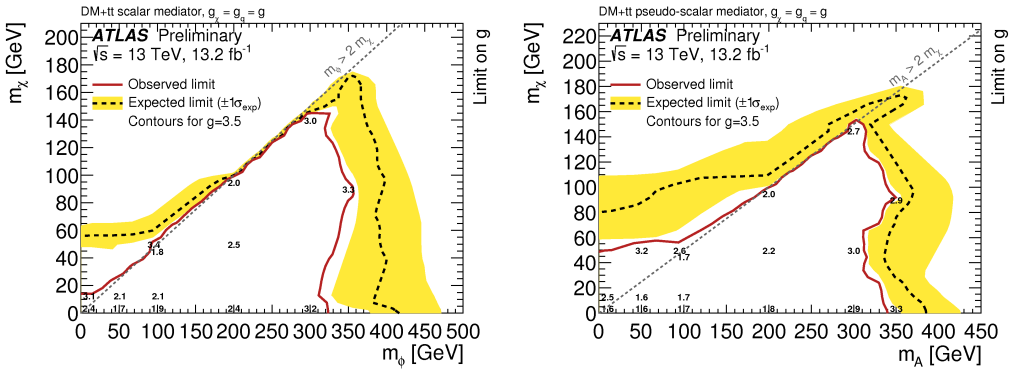

(a) Scalar mediator **(b)** Pseudoscalar mediator

Figure 6.2: Exclusion limits at 95% CL in the $M_{med} - m_\chi$ plane with $g = 3.5$ for the DM+$t\bar{t}$ model with one lepton in the final state [70]. Expected (observed) contour plot corresponds to the blue dashed (red solid) line.

2 Lepton analysis

As for 1 lepton analysis, in 2 lepton search [71] two signal regions optimized for low and high mediator mass have been optimized. The major SM contributions are $t\bar{t}$ and $t\bar{t} + Z$ events, are estimated simultaneously in two control regions. A simultaneous fit on SRs and CRs is performed when setting upper limits at 95% CL on the cross section for each signal model. The observed results are shown in Figure 6.3 in the $M_{med} - m_\chi$ plane.

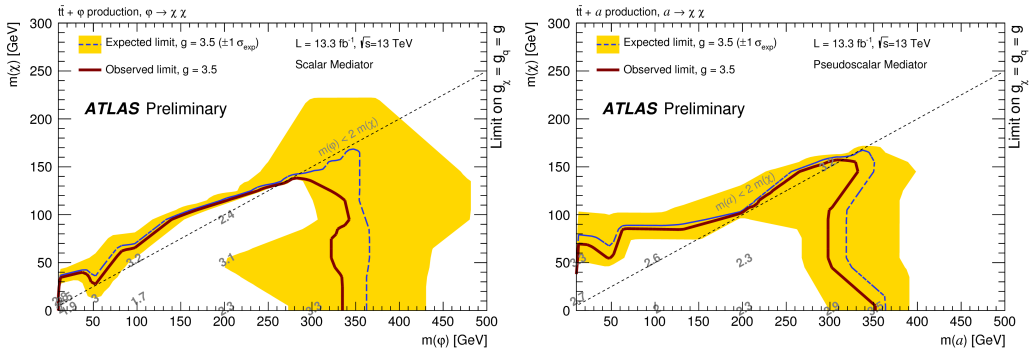

(a) Scalar mediator **(b)** Pseudoscalar mediator

Figure 6.3: Exclusion limits at 95% CL in the $M_{med} - m_{\chi}$ plane with $g = 3.5$ for the DM+$t\bar{t}$ model with two leptons in the final state [69]. Expected (observed) contour plot corresponds to the blue dashed (red solid) line.

6.2 Monojet analysis

In the DM searches picture, the final state with missing transverse momentum and high-p_{T} jets coming from initial state radiation from colliding partons, provides the most sensitive channel for DM discovery. This signature, usually referred as *monojet*, is mainly important in scenarios where DM is produced via an axial-vector mediator, setting limits in the low DM ranges. For the pseudoscalar mediator case monojet channel extends results coming from heavy flavour searches. The results [72] based on 3.2 fb^{-1} data, collected during 2015 collisions will be presented in this section.
The idea pursued in monojet signal region definition is simplicity. In order to be model independent the selection requires a set of cuts on jet multiplicity, leading jet p_{T} and $E_{\mathrm{T}}^{\mathrm{miss}}$.
The triggers employed for the selection of SR events correspond to the lowest unprescaled $E_{\mathrm{T}}^{\mathrm{miss}}$ triggers, with $E_{\mathrm{T}}^{\mathrm{miss}} > 250$ GeV cut, which ensures that all triggers are fully efficient. Events having a primary interaction vertex with at least two associated ID tracks with $p_{\mathrm{T}} > 0.4\,\mathrm{GeV}$ are required. A lepton veto for electrons and muons is applied, and at most four jets are required, the leading one passing tight jet cleaning, with $p_{\mathrm{T}} > 250$ GeV and $|\eta| < 2.4$. In order to suppress multi-jet backgrounds a cut on $\min \Delta\phi(j_i, E_{\mathrm{T}}^{\mathrm{miss}})_{i=1,2,3,4} > 0.4$ is applied.
The main source of background to this search is related to the electroweak background, namely the irreducible background from $Z(\nu\nu)$ + jets events, which mimics the signal, and $W(\ell\nu)$ + jets and $Z(\ell\ell)$ + jets events with mis-

reconstructed leptons. Three dedicated CRs are defined in order to estimate these contributions:

1. a CR with exactly one required muon, CR1μ, to evaluate $Z(\nu\nu)$+jets and $W(\mu\nu)$ + jets backgrounds. The $E_{\mathrm{T}}^{\mathrm{miss}}$ *corr* is taken into account, by treating the selected muon as invisible particle. Although for $Z(\nu\nu)$ + jets a dilepton region would have been the most appropriate choice to control this background, such region suffers of lack of statistics, thus resulting in a larger uncertainty on the final estimate.

2. a CR with exactly one required electron, CR1e, for $W(e\nu)$ + jets , $W(\tau\nu)$ + jets and $Z(\tau\tau)$ + jets estimates. In this CR standard $E_{\mathrm{T}}^{\mathrm{miss}}$ has been used in event selection, mainly for constraining $W(\tau\nu)$+jets process, which is the second dominant background in SR.

3. a CR with exactly two muons, CR2μ for estimating $Z(\mu\mu)$+jets background. Although this contribution is marginal in SR, this CR can give an indication of the compatibility of the normalization factors with the other muon CR.

$Z(ee)$ + jets and diboson events yields a negligible contribution in SR and are estimated only for MC expectations. Despite cuts on $E_{\mathrm{T}}^{\mathrm{miss}}$ and jet multiplicity, top contributions is not negligible due to high cross sections, but the low statistics of a dedicated control regions lead to a MC-only estimation. Non-collision background (NCB) mainly originates from muons created in inelastic beam-gas interactions and from cosmic ray. This source of background dominates the signal region and Tight jet cleaning criteria are applied in order to reject this source which otherwise would be dominating in signal region, and residual NCB is estimated using a data-driven method. Finally multi-jet background is estimated from data with jet smearing method.
The fit strategy used in the analysis relies on a shape fit approach, using $E_{\mathrm{T}}^{\mathrm{miss}}$ as discriminating variable. The distribution has been divided into exclusive $E_{\mathrm{T}}^{\mathrm{miss}}$ bins, and for each bin, a cut-and-count experiment is performed, leading to a final number of normalization factors that depends on the number of defined CRs and bins, $\mathrm{N_{CR}} \times \mathrm{N_{bins}}$. The choice of bin number has been optimized in order to both maximize shape information and avoid statistical fluctuation in the bins. This compromise results in a seven variable $E_{\mathrm{T}}^{\mathrm{miss}}$ bins, starting from $E_{\mathrm{T}}^{\mathrm{miss}} > 250\,\mathrm{GeV}$ and yielding inclusive and exclusive regions. Systematics uncertainties are assumed to be fully correlated between the bins, thus preserving striking changes in nuisance parameters due to statistical fluctuation, particularly significant in high $E_{\mathrm{T}}^{\mathrm{miss}}$ bins. The most significant source of systematics after the fit are related to the theoretical top uncertainties

(2%) and muon uncertainties (2%).
Figure 6.4 shows limits on Dark Matter models set in the $m_\chi - M_{med}$ for an Axial Vector Mediator with $g_\chi = 1$ and $g_q = 0.25$. Mediator mass up to 1 TeV are excluded at 95% CL.

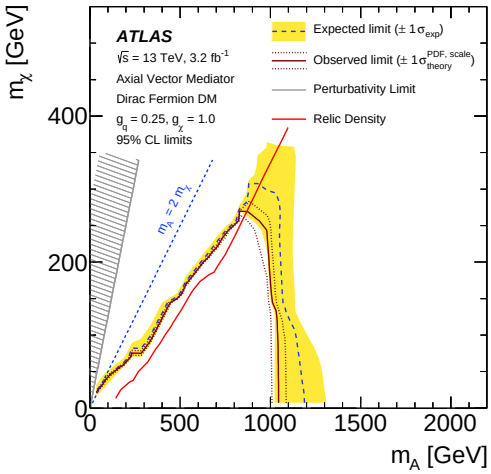

Figure 6.4: 95% CL exclusion contours in the $m_\chi - M_{med}$ plane for an Axial Vector Mediator. The solid (dashed) curve is the observed (expected) limit. The red curve corresponds to the expected relic density (more detail in section 6.5. The region excluded due to perturbativity, defined by $m_\chi > \sqrt{\pi/2}\, m_A$, is indicated by the hatched area. The signal models considered assume minimal mediator width and the coupling values of $g_q = 1/4$ and $g_\chi = 1$ [72].

6.3 Monophoton analysis

The final state with $E_{\mathrm{T}}^{\mathrm{miss}}$ and photon coming from initial state radiation (*monophoton*) constitutes a clear and distinctive signature in DM searches providing a useful cross-check to monojet analysis. However, since $\alpha_{EM} \ll \alpha_S$ a lower statistics is expected to be collected.
In the analysis using $36.1\,\mathrm{fb}^{-1}$ data collected, five signal regions have been designed: three inclusive (SRI1, SRI2, SRi3) with increasing $E_{\mathrm{T}}^{\mathrm{miss}}$ thresholds and two exclusive (SRE1, SRE2) with $E_{\mathrm{T}}^{\mathrm{miss}}$ in two different intervals. A common selection requires at least one isolated photon with $E_{\mathrm{T}} > 150\,\mathrm{GeV}$ with $\Delta\phi(\gamma, E_{\mathrm{T}}^{\mathrm{miss}}) > 0.4$. Lepton and jet vetoes are applied, the latter rejecting events with more than one jet or with a jet with $\Delta\phi(\mathrm{jets}, E_{\mathrm{T}}^{\mathrm{miss}}) < 0.4$. A final cuts on $E_{\mathrm{T}}^{\mathrm{miss}}/\sqrt{\Sigma E_{\mathrm{T}}} > 8.5\,\mathrm{GeV}^{1/2}$ is required to suppress fake $E_{\mathrm{T}}^{\mathrm{miss}}$ events.

The dominant backgrounds of the analysis are $Z/W + \gamma$ events with unidentified electrons or muons and $\gamma +$ jets events where the jets information is partially lost creating fake $E_{\mathrm{T}}^{\mathrm{miss}}$. These contributions are estimated in four dedicated control regions properly defined for each SR. Finally backgrounds originating from fake photons are estimated using data-driven techniques. Two different backgrounds estimation fitting strategies have been adopted: for inclusive signal regions the normalisation factor have been derived independently, while for exclusive signal regions and SRI3 (which is mutually exclusive with SRE1 and SRE2) a background-only multiple-bin fit using simultaneously all corresponding CRs has been applied.
As no excess over SM predictions have been found, limits in the $(m_{\chi} - M_{med})$ plane are set for DM simplified models with an axial-vector and vector mediator. The results are shown in sections 6.5 and 6.6.

6.4 Di-jet analyses

Di-jet searches offer a complementary approach to the mono-X signatures, providing the possibility to look for resonances decaying into a pair quark, which can be interpreted as spin-1 DM mediators. As shown in Figure 6.5 this kind of processes are strongly dependent on the g_q couplings since the cross section results to be proportional to g_q^2.
Different di-jet analyses have been developed in the ATLAS collaboration, using different techniques in order to select the interested events. In the following a brief description of such studies will be given.

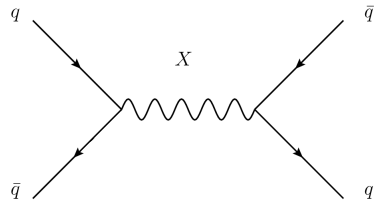

Figure 6.5: Feynman diagram of a di-jet process. The resonance X can be interpreted as vector or axial vector mediator decaying into a quark pair.

6.4.1 Di-jet analysis

Proton-proton interactions at LHC may lead to a $2 \to 2$ parton scattering processes via strong interactions. The presence of a resonance decaying into two jets can be inferred from the study of dijet invariant mass, m_{jj}, in the form of an excess over SM background in the m_{jj} distribution. In particular the dominant SM di-jet background processes coming from multijet events are typically produced at small angles $\theta*$, defined as the polar angle with respect to the direction of the initial partons, while for new BSM signals $\theta*$ is expected to have large values.
The final selection [73] for the analysis based on the total Run-2 statistics of $36.1\,\text{fb}^{-1}$ requires at least two jets with leading (subleading) jet p_{T} above 440 (60) GeV, with at least one jet passing an high level trigger with a 380 GeV p_{T} threshold. The m_{jj} distribution obtained from the selected jets is analysed for two different selections of the Lorentz invariant quantity $y^* = y_1 - y_2$, defined as the rapidity difference of the two outcoming partons, where $y = 1/2ln[(E + p_z)/(E - p_z)]$ with E parton energy and p_z z-axis momentum component. The two selections applied correspond to $|y^*| < 0.6$ and $|y^*| < 1.2$, both optimized for reducing QCD background processes. The respective m_{jj} distributions are shown in Figure 6.6, showing how, with the described requirements, $|y^*| < 0.6$ ($|y^*| < 1.2$) selection is fully efficient above $m_{jj} > 1.1$ TeV ($m_{jj} > 1.7$ TeV).
A dedicated algorithm, BumpHunter [74, 75] is employed for searching resonances in the distribution by evaluating the statistical significance of any localized excess between data and predictions computed in adjacent m_{jj} bins. Final results found a local excess in the interval $4326 - 4595$ GeV for both y^* selections (in Figure 6.6 is indicated by two vertical lines), where, however, without taking into account systematic uncertainties, the probability that background fluctuations would produce an excess at least as significant as the one observed in the data anywhere in the distribution is 0.63 for $|y^*| < 0.6$ selection and 0.83 for $|y^*| < 1.2$ selection. In conclusion, no significant excesses have been found in di-jet analysis.

The energies reached in Run-2 collisions lead to jet triggers with increased thresholds, with the consequence of loosing sensitivity on lighter resonances. In this context the Run-1 di-jet results obtained with $\sqrt{s} = 8$TeV collisions give complementarity to the Run-2 searches. The 8 TeV analysis [76], performed on 20.3fb^{-1} data is similar to 13 TeV one, and the possibility to collect jets with lower p_{T} lead to the m_{jj} distribution shown in Figure 6.7, where only $|y^*| < 0.6$ was applied and a further cut on $m_{jj} > 250\,\text{GeV}$ is required such that the di-jet mass spectrum was unbiased by the kinematic selection on the jet transverse momenta. The most significant discrepancy found by

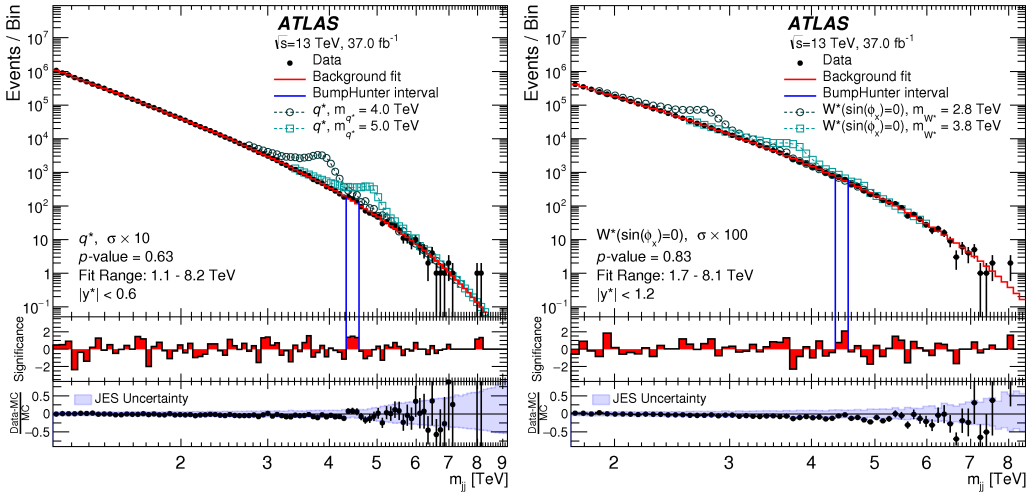

(a) $|y^*| < 0.6$ **(b)** $|y^*| < 1.2$

Figure 6.6: The reconstructed di-jet invariant mass in the $|y^*| < 0.6$ (a) and $|y^*| < 1.2$ selections. The vertical lines indicate the most discrepant intervals identified by the BumpHunter algorithm. In the middle panel the Gaussian significance bin-by-bin of the data with respect to the predicted background is shown. The lower panel shows the relative differences between the data and the prediction of simulation of QCD processes, corrected for NLO and electroweak effects. The shaded band denotes the experimental uncertainty in the jet energy scale calibration [73].

BumpHunter algorithm correspond to a probability of 0.075 and is located in the $390 - 599$ GeV interval.

6.4.2 Trigger Level di-jet analysis

A further possibility to study light resonances in di-jet analysis is to perform a Trigger-object Level Analysis (TLA) exploiting trigger algorithms able to record events containing only information needed for such searches. This technique allows to avoid trigger limitations thus extending discovery potential of di-jet searches to mass range below 1 TeV. The TLA analysis [77] has been performed by ATLAS in Run-2, with an available dataset of $3.4\,\text{fb}^{-1}$ collected events at $\sqrt{s} = 13$ TeV.
A first-level trigger (L1) is implemented to collect jets with $E_{\text{T}} > 75\,\text{GeV}$, identified in region of interest (ROI) in calorimeter segments. The recorded events do not rely on information from tracking on muon detectors, nor on any

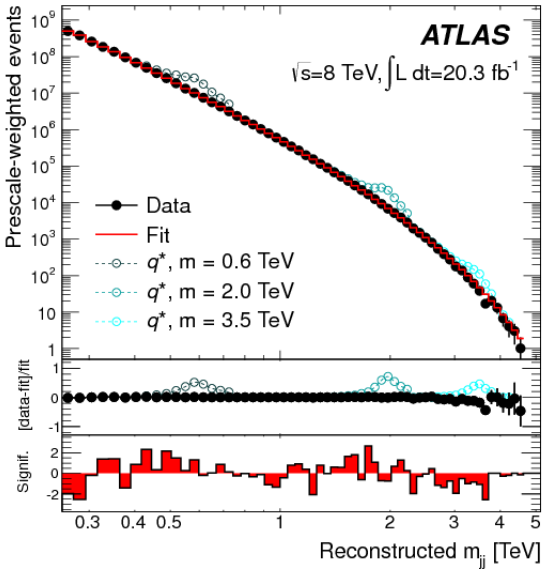

Figure 6.7: The reconstructed di-jet invariant mass in the $|y^*| < 0.6$ selection, for the 8 TeV Analysis [76]. The vertical lines indicate the most discrepant intervals identified by the BumpHunter algorithm. The central panel shows the relative differences between the data and the background fit, while in the lower panel the data-background difference considering statistical uncertainties only is shown.

readout of individual calorimeter elements. Further calibration procedures are then applied on collected jet in order to correct jet four-momenta, pile-up and jet energy scale to match with the calibration scheme used in offline reconstruction.

Event selection follows what described in section 6.4.1. Two signal regions are defined, for $|y^*| < 0.6$ and $|y^*| < 0.3$, with at least two trigger jets within $|\eta| < 2.8$ with p_{T} above 85 GeV, with the leading trigger jet having $p_{\mathrm{T}} > 185$ GeV. The distribution of m_{jj} is shown in Figure 6.8 for the two signal regions, where the blue vertical lines indicate the mass interval where BumpHunter algorithm found the most discrepant interval. As no evidence for significant excess has been found, 95% upper limits on the coupling g_q are derived as function of an axial-vector mediator mass and shown in Figure 6.9 where coupling values above the curves are excluded.

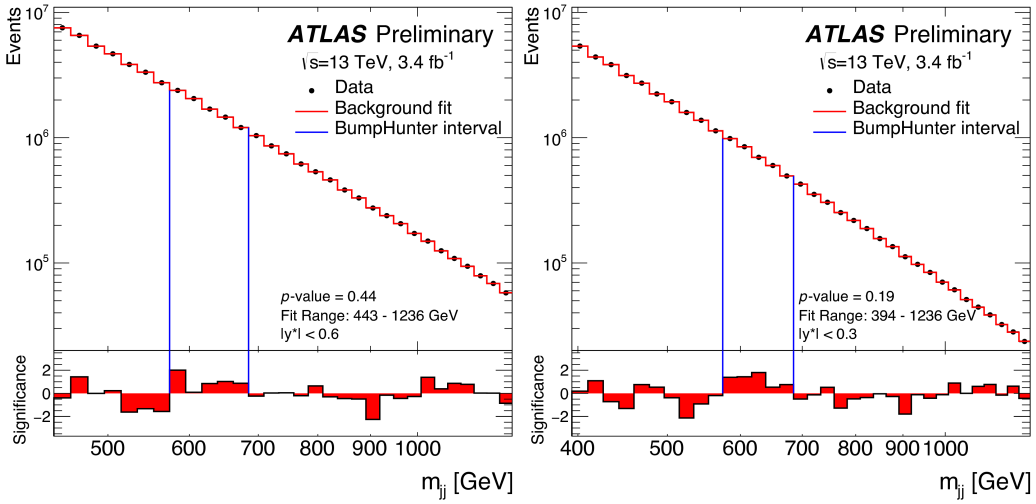

(a) $|y^*| < 0.6$ **(b)** $|y^*| < 0.3$

Figure 6.8: The reconstructed di-jet invariant mass in the $|y^*| < 0.6$ (a) and $|y^*| < 0.3$ (b) selections, for the TLA Analysis [77]. The vertical lines indicate the most discrepant intervals identified by the BumpHunter algorithm. The lower panels show the bin-by-bin significances of the data–fit differences, considering only statistical uncertainties.

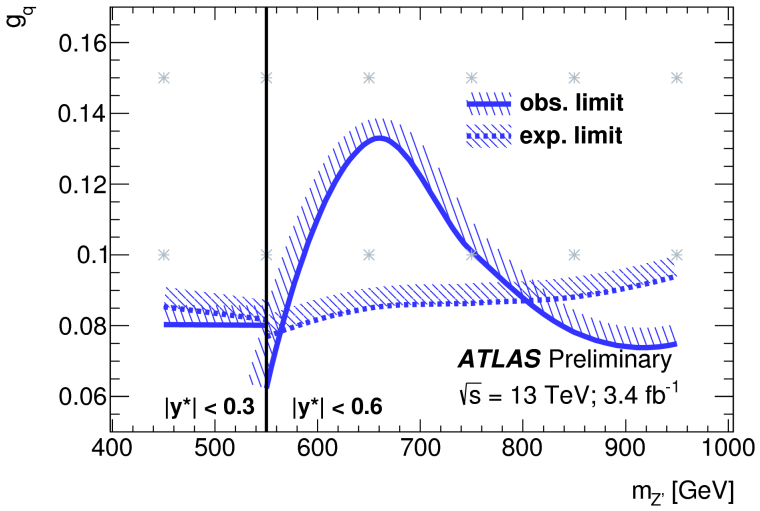

Figure 6.9: The 95% CL upper limit on the coupling g_q as function of the resonance mass $m_{Z'}$. The solid (dotted) lines indicates the observed (expected) limits [77].

6.4.3 Di-jet analysis with Initial State Radiation objects

Another way to go beyond trigger limitations is a search where the resonance produced is boosted in the transverse direction via recoil from an initial state radiation (ISR) object with high p_{T} , namely a photon or a jet, as illustrated in Figure 6.10. While paying in term of signal rates production due to the low cross sections, the ISR tagging allows to explore lower dijet mass ranges: $200-1500$ GeV for the search with an ISR photon and $300-600$ GeV for an ISR jet. The results of the analysis with $15.5\,\mathrm{fb}^{-1}$ [78] at $\sqrt{s} = 13$ TeV will be briefly described in the following.
In the search with a photon $(X+\gamma)$ an isolated photon with $p_{\mathrm{T}} > 150GeV$ and at least two jets with $p_{\mathrm{T}} > 25\,\mathrm{GeV}$ and $|\eta| < 2.8$ are required. The QCD background is reduced by applying a cut on $|y^*/2| < 0.8$. In the ISR jet selection $(X+j)$ a jet with $p_{\mathrm{T}} > 430\,\mathrm{GeV}$ is required along with the aforementioned criteria for the remaining jets. The angular requirements is performed on the difference rapidity of the second and third highest p_{T} jets, $|y^*_{23}/2 < 0.6|$. The distribution of dijet invariant mass for the two searches are shown in Figure 6.11. No significant excesses have been found and 95% upper limits on the coupling g_q as function of mediator mass are shown in Figure 6.12.

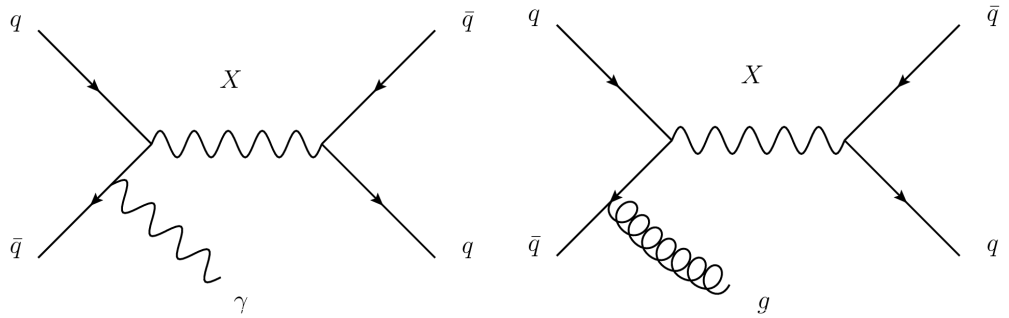

(a) $X+\gamma$ **(b)** $X+j$

Figure 6.10: Feynman diagrams for the production of a new resonance X recoiling against an ISR (a) photon or (b) jet [78].

6.4.4 Setting limits on di-jet analyses

Di-jet analysis results can be interpreted as DM limits in the $(m_\chi\,, M_{med}\,)$ plane in order to compare them with monojet and monophoton results for

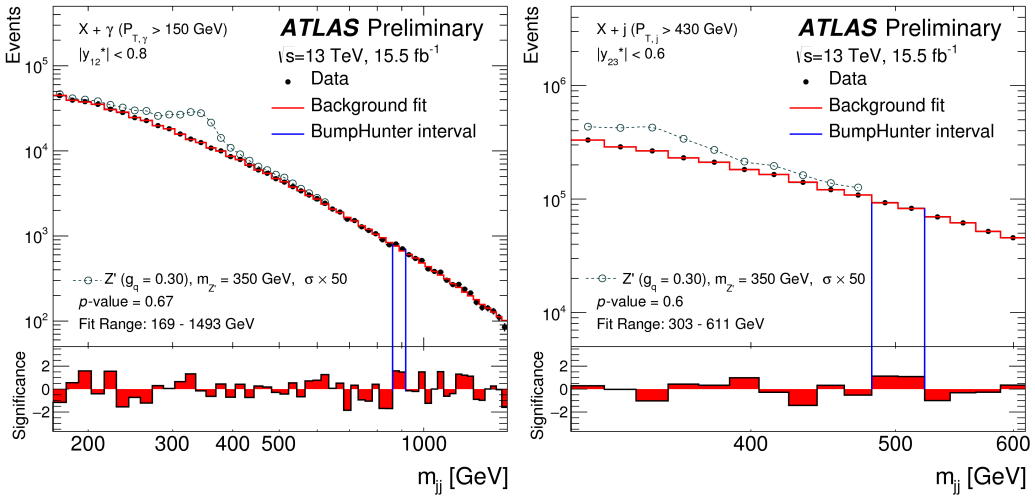

(a) $X + \gamma$ **(b)** $X + j$

Figure 6.11: The reconstructed di-jet invariant mass in the $X + \gamma$ (a) and $X + j$ analyses [78]. The vertical lines indicate the most discrepant intervals identified by the BumpHunter algorithm. In the lower panel the Gaussian significance bin-by-bin of the data with respect to the predicted background is shown.

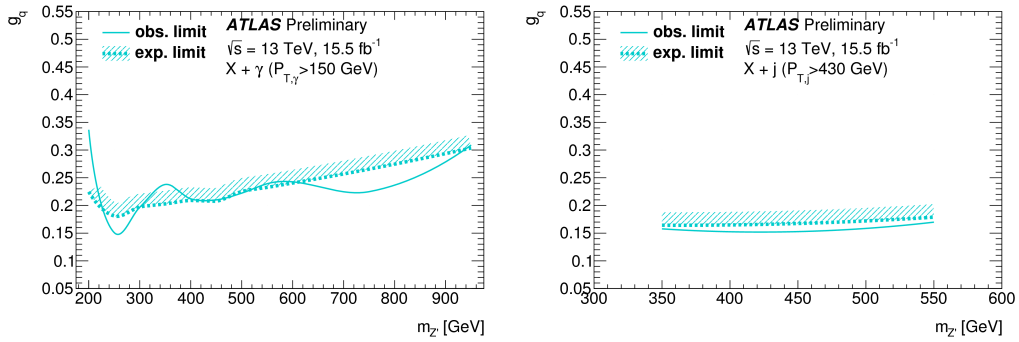

(a) $X + \gamma$ **(b)** $X + j$

Figure 6.12: The 95% CL upper limit on the coupling g_q as function of the resonance mass $m_{Z'}$ for $X + \gamma$ (a) and $X + j$ (b) selections. The solid (dotted) lines indicates the observed (expected) limits [78].

the vector and axial-vector mediator scenario. The procedure relies on resonances that are approximately Gaussian near the core, with tails smaller than background and it follows several steps:

1. A MC samples with new particle with mass M is generated. The

kinematic selection on the parton η, p_{T} and $|y^*|$ is applied.

2. The signal mass distribution is smeared to take into account detector effects. The smearing factor distribution depends on di-jet invariant mass as shown in Figure 6.13.

3. The Gaussian signal distribution is limited to $0.8M$ and $1.2M$: this allows to reject long tails in the reconstructed m_{jj}. The mean mass m is recalculated after this truncation. The fraction of surviving events determines the acceptance $\mathcal{A}$.

4. Select the Gaussian signal with m_G so that $m_G = m$. If there's no exact correspondence among Gaussian samples, consider the limits for m_G values above and below m, and take the larger one in order to be conservative.

5. For this mass point, choose the value of σ_G/m_G such that the region within $\pm 2\sigma_G$ is contained in the truncated mass range.

6. The tabulated 95% CL upper limit corresponding to the chosen Gaussian signal is finally compared to the product of theoretical cross section and acceptance (taking into account its branching ration into two jets), $\sigma \times \mathcal{A}$.

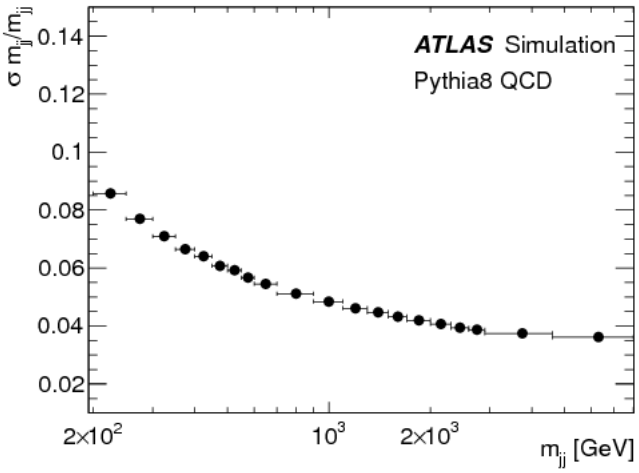

Figure 6.13: Dijet mass resolution obtained from fully simulated PYTHIA QCD Monte Carlo [76].

6.5 Comparison of results

The limits resulting from the monojet, monophoton and di-jet analyses are presented in the $(m_\chi\,, M_{med}\,)$ plane for a fixed choice of the couplings.
In the *freeze-out* scheme of the early Universe the DM abundance, initially present in thermal equilibrium, has changed due to annihilation processes during universe expansion and set the DM density observed today. Simplified models can be used in order to predict the relic density and compare with most recent measurements observed by Planck collaboration, corresponding to $\Omega_\chi h^2 = 0.12$ [15, 79]. Hence relic density calculations can be shown on the $(m_\chi\,, M_{med}\,)$ plane as an indication of where a specific simplified model is likely to explain the observed value [80]. It should be noted that a simplified model is not excluded if its parameters are inconsistent with the relic density curve, rather that other processes in addition to the specific simplified model should be considered.
In Figure 6.14a summary results for an axial-vector mediator with $g_q = 0.25$ and $g_\chi = 1$ are shown. The DM scenarios tested does not include lepton couplings, hence $g_l = 0$. In the region between the two dashed curve indicating relic density annihilation processes described by simplified model lead to Ω_χ below $0.12h^2$. The dotted curve divides on-shell and off-shell regions while the shading in the upper left indicates excluded regions due to perturbativity unitarity. A similar plot for a vector mediator is shown in Figure 6.14b for the same coupling choice and di-jet results combined in a single exclusion. Di-jet searches can exclude up to the TeV scale for both DM and mediator masses, while the mono-X searches are sensitive to low DM masses, thus providing complementary results.

6.6 Comparison with Dark Matter direct detection searches

Simplified models results can be reinterpreted in terms of DM-nucleon scattering cross section as function of DM mass in order to compare with non-collider direct detection searches. The inverse procedure, interpreting non collider results in the simplified model framework, requires a set of assumptions and it is typically more complicated. For example the relic density predicted by the simplified models depends on the specific point of the $(m_\chi\,, M_{med}\,)$ plane, whereas non-collider results assume that DM density saturates the cosmological density thus allowing only one type of DM.
It should be noted that, while non-collider results can be valid for different DM models, this assumption does not hold for simplified models, since only

the specific mediator and couplings choice can be excluded.
As direct detection experiments distinguish between spin-dependent (SD) and spin-independent (SI) results, it is possible to translate vector and scalar mediators for the first case and axial-vector mediator for the second one [79]. In particular, for SD results it is necessary to distinguish between DM-proton and DM-neutron scattering cross section because DM scatters with the spin of the isotope which is approximately due to an unpaired neutron or proton. The SI cross section can be written in the form

$$\sigma_{\mathrm{SI}} = \frac{f^2(g_q)\,{g_\chi}^2\mu_{n\chi}^2}{\pi {M_{med}}^4}\,, \tag{6.1}$$

where $\mu_{n\chi} = m_n m_\chi/(m_n + m_\chi)$ is the DM-nucleon reduced mass with $m_n \simeq 0.939\,\mathrm{GeV}$ the nucleon mass and $f(g_q)$ is the mediator-nucleon coupling, which for a vector mediator is

$$f(g_q) = 3g_q\,, \tag{6.2}$$

and hence

$$\sigma_{\mathrm{SI}} \simeq 6.9\times10^{-41}\ \mathrm{cm}^2 \cdot \left(\frac{g_q\,g_\chi}{0.25}\right)^2 \left(\frac{1\,\mathrm{TeV}}{M_{med}}\right)^4 \left(\frac{\mu_{n\chi}}{1\,\mathrm{GeV}}\right)^2. \tag{6.3}$$

For the axial-vector mediator, the SD cross sections is

$$\sigma_{\mathrm{SD}} = \frac{3f^2(g_q)\,{g_\chi}^2\mu_{n\chi}^2}{\pi {M_{med}}^4}\,. \tag{6.4}$$

The term $f^{p,n}(g_q)$ is different for protons and neutrons and can be w

$$f^{p,n}(g_q) = \Delta_u^{(p,n)}\,g_u + \Delta_d^{(p,n)}\,g_d + \Delta_s^{(p,n)}\,g_s\,, \tag{6.5}$$

where $\Delta_u^{(p)} = \Delta_d^{(n)} = 0.84$, $\Delta_d^{(p)} = \Delta_u^{(n)} = -0.43$ and $\Delta_s = -0.09$ are the values recommended by the Particle Data Group [4].

Assuming that the coupling g_q is the same all quarks, one obtains

$$f(g_q) = 0.32g_q\,, \tag{6.6}$$

and thus

$$\sigma^{\mathrm{SD}} \simeq 2.4\times10^{-42}\ \mathrm{cm}^2 \cdot \left(\frac{g_q\,g_\chi}{0.25}\right)^2 \left(\frac{1\,\mathrm{TeV}}{M_{\mathrm{med}}}\right)^4 \left(\frac{\mu_{n\chi}}{1\,\mathrm{GeV}}\right)^2. \tag{6.7}$$

This result is valid for both DM-neutron and DM-proton scattering.
These procedures have been applied to monophoton and di-jet searches

providing the results shown in Figure 6.15 and 6.16 respectively for SD and SI cases. For direct detection with SD DM-nucleon cross sections 95% limits are both inferred for the DM-neutron (Figure 6.15a) and DM-proton (Figure 6.15b) cross section. The results show the complementarity of LHC searches in the low DM mass region corresponding to $m_\chi < 10, \mathrm{GeV}$, where the very low energy exchanged during the collisions with the nuclei can not be detected from direct direction experiments.

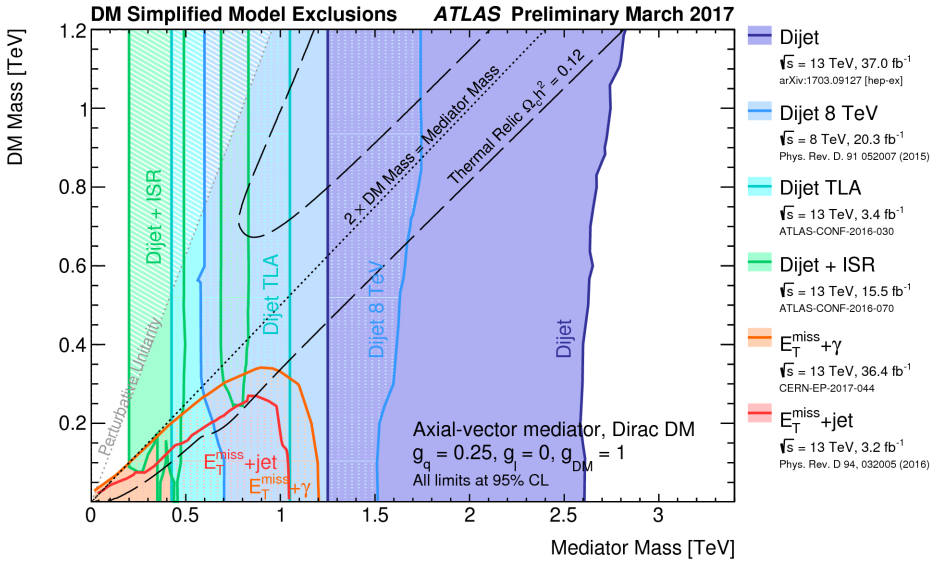

(a) Axial-vector mediator

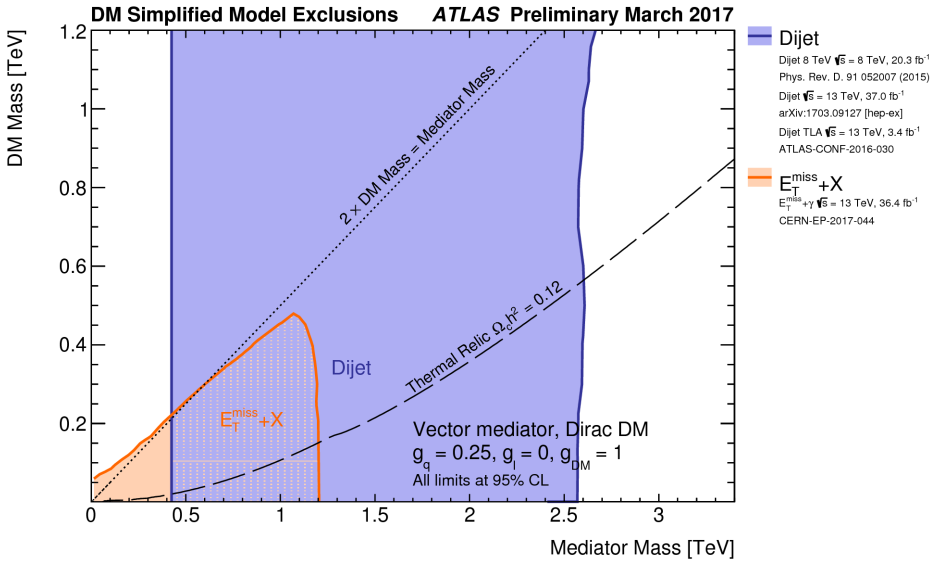

(b) Vector mediator

Figure 6.14: Excluded region at 95% CL in the (m_χ, M_{med}) in the axial-vector (a) and vector (b) mediator scenarios in the monojet, monophoton and di-jet combination results. The choice of couplings corresponds to $g_q = 0.25$, $g_\chi = 1$ and $g_l = 0$. The dashed curve denotes the points in the plane for which $\Omega_\chi h^2 = 0.12$. The dotted line delimits the on-shell and off-shell regions of the plane. For the axial-vector mediator, the shaded regions are excluded due to perturbativity unitarity [81].

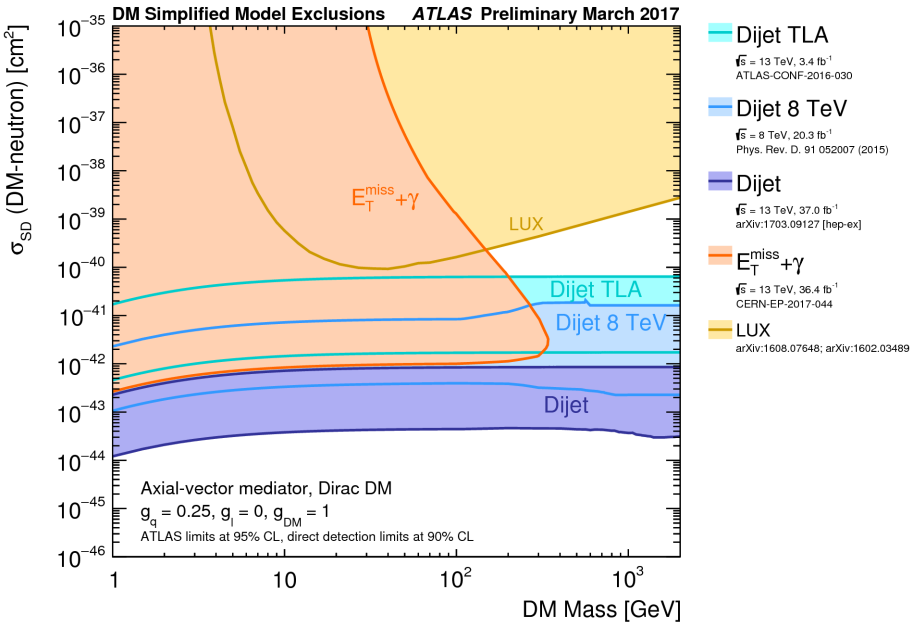

(a) DM-neutron cross section

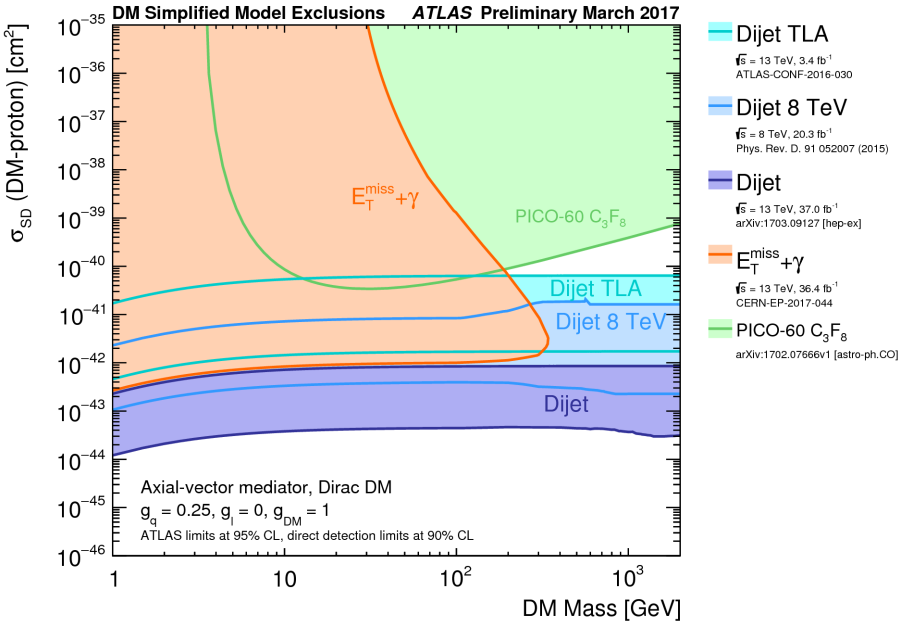

(b) DM-proton cross section

Figure 6.15: A comparison of the inferred limits to the constraints from direct detection experiments on the spin-dependent DM-nucleon scattering cross section in the context of the simplified model with axial-vector couplings [81]. The choice of couplings corresponds to $g_q = 0.25$, $g_\chi = 1$ and $g_l = 0$. LHC limits are shown at 95% CL and direct detection limit at 90%. For DM-neutron cross section limits (a) collider results are compared with LUX experiment [82, 83] while for DM-proton cross section limits PICO-60 [84] results are reported.

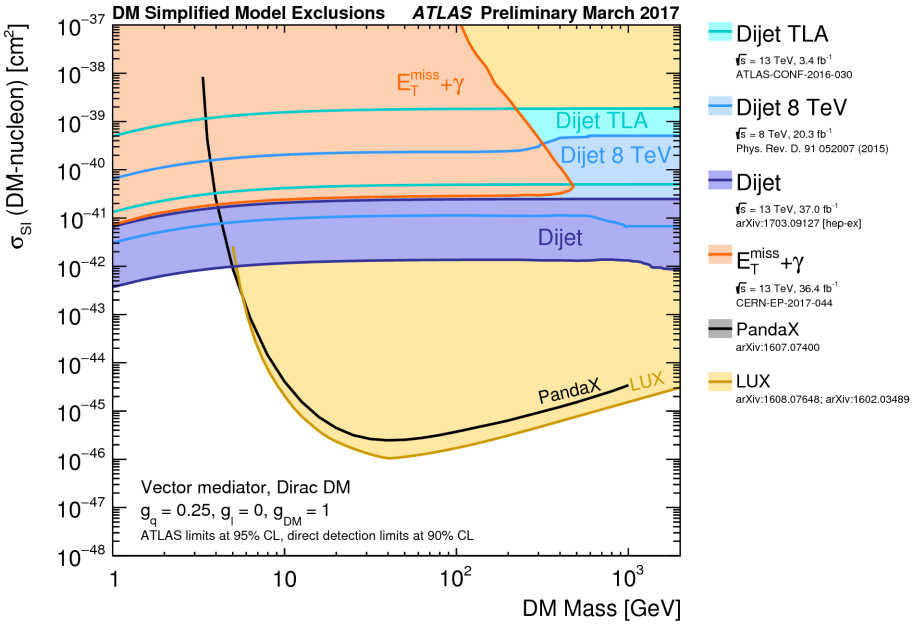

Figure 6.16: A comparison of the inferred limits to the constraints from direct detection experiments on the spin-independent DM-nucleon scattering cross section in the context of the simplified model with axial-vector couplings [81]. The choice of couplings corresponds to $g_q = 0.25$, $g_\chi = 1$ and $g_l = 0$. LHC limits are shown at 95% CL and direct detection limit at 90%. Collider results are compared with LUX [82, 83] and PandaX [85] experiments.

Conclusions

Many theoretical models, such as SUSY, DM, Extra dimensions have been developed in order to provide an extension to the Standard Model framework, which, despite the plethora of experimental successes, can not be considered as a finite theory of Particle Physics. Henceforth Beyond Standard Model Physics represents one of the most challenging goal in the LHC programme where the large energies reached in proton-proton collisions can offer the possibility to discover new particles.
Most of BSM candidates predicted by theory are neutral non interacting particles leading to a peculiar signature with missing transverse momentum $E_{\mathrm{T}}^{\mathrm{miss}}$. This thesis work describes a search for these particles produced in association with jets with a particular focus on signatures involving bottom quarks.
In Run-2 DM analyses simplified models are the paradigma adopted at LHC. Dark Matter pair production occurs via a massive mediator (scalar, pseudoscalar, vector, axial-vector) who couples with non vanishing coupling with SM and DM particles. Several Dark Matter benchmark models have been produced, which cover a wide range of phenomenology, allowing to probe all the phase space and maximise possibilities for early discovery of DM with the upcoming data. As mediators of the scalar and pseudoscalar types are expected to have Yukawa-like couplings to the SM quarks, the final state of E_T^{miss} with heavy flavour quarks (b or t) represents an important signature to probe at hadronic colliders. The $b\bar{b} + E_{\mathrm{T}}^{\mathrm{miss}}$ final state is theoretically motivated by scenarios in which a spin-0 mediator couples to down generation quarks. These studies allow a complementary search to the $t\bar{t}$+ DM models. The channel is also interpreted in light of the bottom-Flavoured Dark Matter model (b-FDM). This model has been proposed for explaining the excess of gamma rays from the galactic centre, observed by the Fermi Gamma-ray Space Telescope and interpreted as a signal for annihilating DM which favors couplings to third generation quarks via Yukawa couplings.
The analysis is based on the full dataset of $36.1\,\mathrm{fb}^{-1}$ collected at $\sqrt{s} = 13$ TeV. Results are expressed in terms of limits on the production cross-section

of scalar and pseudoscalar mediators decaying into DM particles. Upper limits on the signal strength have been obtained as function of the mediator mass. A new fitting procedure has been introduced, which exploits the shape information of the most relevant discriminating variable $cos\theta^*$ (the cosine of the bjets system opening angle), thus providing better sensitivity with respect to the approach adopted in [67]. An overall improvement has been achieved in all mediator masses studied, with the best limit obtained for a signal with $m_\chi = 1\,\text{GeV}$ and $M_{med} = 50\,\text{GeV}$ with couplings $g_q = g_\chi = 1$ where expected results have been improved by a factor 5 with respect to the observed results corresponding to 13.3fb^{-1}.
Finally an overview of the latest results of DM searches has been illustrated: mono-X signatures (final states tagging a SM particle and $E_{\text{T}}^{\text{miss}}$) are compared with di-jet searches. A particular emphasis has been dedicated to the interpretation of LHC results in terms of DM-nucleon scattering cross section to have a direct comparison with non-collider searches.

Appendix A

Systematics breakdown

The breakdown of the systematics for all backgrounds in each CRB, VRB and SRB bin are shown in Tables A.1-A.4

The breakdown of the systematics for all backgrounds in each SRBFH bin and CRZBFH are shown in Tables A.5-A.6

Uncertainty of channel	CRTB
Total background expectation	129.19
Total statistical ($\sqrt{N_{\text{exp}}}$)	±11.37
Total background systematic	±11.36 [8.79%]
mu_ttbar	±17.87 [13.8%]
alpha_JER	±7.71 [6.0%]
alpha_METSoftTrkResoPara	±5.59 [4.3%]
gamma_stat_CRTB_cuts_bin_0	±5.28 [4.1%]
alpha_jesNP1	±4.21 [3.3%]
alpha_FTEFFB	±4.15 [3.2%]
alpha_EGRES	±3.13 [2.4%]
alpha_stRad	±3.11 [2.4%]
alpha_Stxsec	±2.45 [1.9%]
alpha_jesNP3	±1.71 [1.3%]
alpha_WjetsTHSyst3	±1.57 [1.2%]
alpha_FTEFFC	±0.97 [0.75%]
alpha_jesNP2	±0.84 [0.65%]
alpha_FTEFFextrap	±0.78 [0.60%]
alpha_FTEFFLight	±0.44 [0.34%]
alpha_METSoftTrkScale	±0.39 [0.30%]
alpha_METSoftTrkResoPerp	±0.37 [0.29%]
alpha_MUONSSCALE1	±0.35 [0.27%]
alpha_Wjetxsec	±0.35 [0.27%]
alpha_WjetsTHSyst1	±0.28 [0.22%]
alpha_PRWDATASF	±0.25 [0.20%]
alpha_WjetsTHSyst4	±0.23 [0.18%]
alpha_WjetsTHSyst2	±0.21 [0.16%]
alpha_MUONEFFTrigSyst	±0.15 [0.12%]
alpha_JvtEff	±0.15 [0.12%]
alpha_MUONEFFTrigStat	±0.10 [0.08%]
alpha_ELEFFID	±0.09 [0.07%]
alpha_MUONEFFSYS1	±0.05 [0.04%]
mu_Z	±0.04 [0.03%]
alpha_ELEFFTrigger	±0.04 [0.03%]
alpha_JETEtaNonClosure	±0.03 [0.03%]
alpha_ELEFFIso	±0.03 [0.02%]
alpha_ZjTHren	±0.02 [0.02%]
alpha_ZjTHckkw	±0.02 [0.01%]
alpha_MUONEFFSTAT	±0.01 [0.01%]
alpha_ELEFFReco	±0.01 [0.01%]
alpha_EGSCALE	±0.01 [0.01%]
alpha_MUONISOSYS1	±0.01 [0.01%]
alpha_ZjTHqsf	±0.01 [0.01%]
alpha_ZjTHfac	±0.01 [0.00%]
alpha_MUONISOSTAT	±0.00 [0.00%]
gamma_stat_SRB_bin1_cuts_bin_0	±0.00 [0.00%]
gamma_stat_SRB_bin3_cuts_bin_0	±0.00 [0.00%]
gamma_stat_VRB2_cuts_bin_0	±0.00 [0.00%]
alpha_VVTheory	±0.00 [0.00%]
alpha_MUONEFFSYSLOWPT	±0.00 [0.00%]
alpha_topRad	±0.00 [0.00%]
gamma_stat_CRZB_cuts_bin_0	±0.00 [0.00%]
alpha_ttbarGen	±0.00 [0.00%]
alpha_ELEFFTriggerEff	±0.00 [0.00%]
alpha_FTEFFextrapC	±0.00 [0.00%]
gamma_stat_SRB_bin0_cuts_bin_0	±0.00 [0.00%]
alpha_MUONEFFSTATLOWPT	±0.00 [0.00%]
gamma_stat_SRB_bin2_cuts_bin_0	±0.00 [0.00%]

Table A.1: Breakdown of the dominant systematic uncertainties on background estimates in the various signal regions. Note that the individual uncertainties can be correlated, and do not necessarily add up quadratically to the total background uncertainty. The percentages show the size of the uncertainty relative to the total expected background.

Uncertainty of channel	CRZB
Total background expectation	160.93
Total statistical ($\sqrt{N_{\text{exp}}}$)	±12.69
Total background systematic	±12.66 [7.87%]
mu_Z	±32.85 [20.4%]
alpha_ZjTHren	±26.08 [16.2%]
alpha_ZjTHqsf	±8.75 [5.4%]
alpha_ZjTHckkw	±8.61 [5.3%]
alpha_METSoftTrkResoPara	±6.02 [3.7%]
alpha_ZjTHfac	±4.38 [2.7%]
gamma_stat_CRZB_cuts_bin_0	±4.34 [2.7%]
mu_ttbar	±2.09 [1.3%]
alpha_PRWDATASF	±1.08 [0.67%]
alpha_jesNP1	±0.77 [0.48%]
alpha_METSoftTrkResoPerp	±0.74 [0.46%]
alpha_JER	±0.69 [0.43%]
alpha_stRad	±0.59 [0.37%]
alpha_JETEtaNonClosure	±0.36 [0.23%]
alpha_FTEFFC	±0.21 [0.13%]
alpha_jesNP3	±0.21 [0.13%]
alpha_FTEFFextrap	±0.16 [0.10%]
alpha_Stxsec	±0.12 [0.07%]
alpha_METSoftTrkScale	±0.12 [0.07%]
alpha_EGRES	±0.11 [0.07%]
alpha_jesNP2	±0.07 [0.04%]
alpha_ELEFFID	±0.07 [0.04%]
alpha_MUONEFFSYS1	±0.06 [0.04%]
alpha_FTEFFB	±0.05 [0.03%]
alpha_MUONEFFSTAT	±0.02 [0.01%]
alpha_MUONISOSYS1	±0.02 [0.01%]
alpha_ELEFFIso	±0.02 [0.01%]
alpha_MUONEFFTrigSyst	±0.01 [0.01%]
alpha_MUONSSCALE1	±0.01 [0.01%]
alpha_ELEFFReco	±0.01 [0.01%]
alpha_MUONEFFTrigStat	±0.01 [0.01%]
alpha_EGSCALE	±0.01 [0.00%]
alpha_JvtEff	±0.00 [0.00%]
alpha_ELEFFTrigger	±0.00 [0.00%]
alpha_MUONISOSTAT	±0.00 [0.00%]
alpha_FTEFFLight	±0.00 [0.00%]
gamma_stat_SRB_bin1_cuts_bin_0	±0.00 [0.00%]
gamma_stat_SRB_bin3_cuts_bin_0	±0.00 [0.00%]
alpha_WjetsTHSyst1	±0.00 [0.00%]
gamma_stat_VRB2_cuts_bin_0	±0.00 [0.00%]
gamma_stat_CRTB_cuts_bin_0	±0.00 [0.00%]
alpha_VVTheory	±0.00 [0.00%]
alpha_MUONEFFSYSLOWPT	±0.00 [0.00%]
alpha_topRad	±0.00 [0.00%]
alpha_Wjetxsec	±0.00 [0.00%]
alpha_ttbarGen	±0.00 [0.00%]
alpha_ELEFFTriggerEff	±0.00 [0.00%]
alpha_FTEFFextrapC	±0.00 [0.00%]
alpha_WjetsTHSyst2	±0.00 [0.00%]
gamma_stat_SRB_bin0_cuts_bin_0	±0.00 [0.00%]
alpha_MUONEFFSTATLOWPT	±0.00 [0.00%]
alpha_WjetsTHSyst4	±0.00 [0.00%]
alpha_WjetsTHSyst3	±0.00 [0.00%]
gamma_stat_SRB_bin2_cuts_bin_0	±0.00 [0.00%]

Table A.2: Breakdown of the dominant systematic uncertainties on background estimates in the various signal regions. Note that the individual uncertainties can be correlated, and do not necessarily add up quadratically to the total background uncertainty. The percentages show the size of the uncertainty relative to the total expected background.

Uncertainty of channel	VRB2
Total background expectation	179.51
Total statistical ($\sqrt{N_{\text{exp}}}$)	±13.40
Total background systematic	±20.35 [11.33%]
mu_Z	±22.78 [12.7%]
alpha_ZjTHren	±19.47 [10.8%]
alpha_EGRES	±9.79 [5.5%]
alpha_FTEFFC	±9.34 [5.2%]
alpha_ZjTHckkw	±7.58 [4.2%]
alpha_METSoftTrkResoPerp	±6.53 [3.6%]
mu_ttbar	±6.49 [3.6%]
gamma_stat_VRB2_cuts_bin_0	±6.35 [3.5%]
alpha_METSoftTrkResoPara	±6.27 [3.5%]
alpha_ZjTHqsf	±6.06 [3.4%]
alpha_WjetsTHSyst3	±4.06 [2.3%]
alpha_jesNP3	±3.55 [2.0%]
alpha_FTEFFB	±2.68 [1.5%]
alpha_Stxsec	±2.05 [1.1%]
alpha_ZjTHfac	±2.02 [1.1%]
alpha_JETEtaNonClosure	±1.70 [0.95%]
alpha_MUONSSCALE1	±1.51 [0.84%]
alpha_EGSCALE	±1.34 [0.75%]
alpha_jesNP2	±1.32 [0.73%]
alpha_PRWDATASF	±1.14 [0.64%]
alpha_MUONEFFSYS1	±1.11 [0.62%]
alpha_ELEFFID	±1.09 [0.61%]
alpha_jesNP1	±1.04 [0.58%]
alpha_WjetsTHSyst1	±1.03 [0.58%]
alpha_Wjetxsec	±0.95 [0.53%]
alpha_WjetsTHSyst4	±0.74 [0.41%]
alpha_WjetsTHSyst2	±0.59 [0.33%]
alpha_METSoftTrkScale	±0.59 [0.33%]
alpha_FTEFFLight	±0.56 [0.31%]
alpha_FTEFFextrap	±0.40 [0.22%]
alpha_ELEFFIso	±0.38 [0.21%]
alpha_MUONEFFTrigSyst	±0.34 [0.19%]
alpha_MUONISOSYS1	±0.26 [0.14%]
alpha_MUONEFFSTAT	±0.24 [0.13%]
alpha_MUONEFFTrigStat	±0.23 [0.13%]
alpha_stRad	±0.22 [0.12%]
alpha_ELEFFReco	±0.21 [0.12%]
alpha_ELEFFTrigger	±0.12 [0.07%]
alpha_JvtEff	±0.12 [0.07%]
alpha_JER	±0.06 [0.03%]
alpha_MUONISOSTAT	±0.03 [0.01%]
gamma_stat_SRB_bin1_cuts_bin_0	±0.00 [0.00%]
gamma_stat_SRB_bin3_cuts_bin_0	±0.00 [0.00%]
gamma_stat_CRTB_cuts_bin_0	±0.00 [0.00%]
alpha_VVTheory	±0.00 [0.00%]
alpha_MUONEFFSYSLOWPT	±0.00 [0.00%]
alpha_topRad	±0.00 [0.00%]
gamma_stat_CRZB_cuts_bin_0	±0.00 [0.00%]
alpha_ttbarGen	±0.00 [0.00%]
alpha_ELEFFTriggerEff	±0.00 [0.00%]
alpha_FTEFFextrapC	±0.00 [0.00%]
gamma_stat_SRB_bin0_cuts_bin_0	±0.00 [0.00%]
alpha_MUONEFFSTATLOWPT	±0.00 [0.00%]
gamma_stat_SRB_bin2_cuts_bin_0	±0.00 [0.00%]

Table A.3: Breakdown of the dominant systematic uncertainties on background estimates in the various signal regions. Note that the individual uncertainties can be correlated, and do not necessarily add up quadratically to the total background uncertainty. The percentages show the size of the uncertainty relative to the total expected background.

Uncertainty of channel	SRB_bin0	SRB_bin1	SRB_bin2	SRB_bin3
Total background expectation	77.28	71.79	75.61	66.35
Total statistical ($\sqrt{N_{\text{exp}}}$)	±8.79	±8.47	±8.70	±8.15
Total background systematic	±12.81 [16.57%]	±11.34 [15.80%]	±12.70 [16.80%]	±9.18 [13.84%]
mu_Z	±8.83 [11.4%]	±9.89 [13.8%]	±11.89 [15.7%]	±12.39 [18.7%]
alpha_jesNP1	±6.90 [8.9%]	±7.10 [9.9%]	±6.54 [8.6%]	±3.29 [5.0%]
alpha_ZjTHren	±4.82 [6.2%]	±5.84 [8.1%]	±6.85 [9.1%]	±6.27 [9.4%]
alpha_ttbarGen	±4.62 [6.0%]	±2.49 [3.5%]	±3.10 [4.1%]	±1.60 [2.4%]
alpha_FTEFFC	±4.37 [5.7%]	±1.70 [2.4%]	±0.02 [0.03%]	±0.17 [0.26%]
gamma_stat_SRB	±4.36 [5.6%]	±3.47 [4.8%]	±4.24 [5.6%]	±4.24[6.4%]
alpha_JER	±3.36 [4.3%]	±3.38 [4.7%]	±5.20 [6.9%]	±0.86 [1.3%]
mu_ttbar	±3.27 [4.2%]	±2.55 [3.6%]	±2.59 [3.4%]	±1.28 [1.9%]
alpha_MUONSSCALE1	±3.04 [3.9%]	±0.01 [0.01%]	±0.02 [0.03%]	±0.03 [0.05%]
alpha_METSoftTrkResoPara	±3.02 [3.9%]	±1.08 [1.5%]	±1.58 [2.1%]	±1.93 [2.9%]
alpha_FTEFFB	±2.91 [3.8%]	±2.36 [3.3%]	±2.25 [3.0%]	±1.62 [2.4%]
alpha_ZjTHckkw	±2.59 [3.4%]	±2.81 [3.9%]	±3.22 [4.3%]	±3.52 [5.3%]
alpha_ZjTHqsf	±2.51 [3.2%]	±2.81 [3.9%]	±3.48 [4.6%]	±3.69 [5.6%]
alpha_EGRES	±2.46 [3.2%]	±1.65 [2.3%]	±1.22 [1.6%]	±0.51 [0.77%]
alpha_METSoftTrkResoPerp	±2.07 [2.7%]	±3.05 [4.3%]	±4.53 [6.0%]	±2.22 [3.3%]
alpha_Stxsec	±1.46 [1.9%]	±1.01 [1.4%]	±0.55 [0.72%]	±0.26 [0.39%]
alpha_stRad	±1.21 [1.6%]	±0.36 [0.50%]	±0.59 [0.78%]	±1.42 [2.1%]
alpha_jesNP3	±1.17 [1.5%]	±2.13 [3.0%]	±0.08 [0.10%]	±0.69 [1.0%]
alpha_topRad	±1.07 [1.4%]	±1.11 [1.5%]	±1.83 [2.4%]	±1.53 [2.3%]
alpha_WjetsTHSyst3	±0.93 [1.2%]	±0.58 [0.80%]	±0.48 [0.63%]	±0.22 [0.33%]
alpha_ZjTHfac	±0.78 [1.0%]	±0.88 [1.2%]	±1.06 [1.4%]	±1.10 [1.7%]
alpha_PRWDATASF	±0.57 [0.74%]	±0.28 [0.39%]	±0.07 [0.10%]	±0.95 [1.4%]
alpha_METSoftTrkScale	±0.50 [0.65%]	±0.28 [0.39%]	±0.46 [0.61%]	±0.28 [0.42%]
alpha_MUONEFFSYS1	±0.45 [0.58%]	±0.47 [0.66%]	±0.56 [0.74%]	±0.55 [0.83%]
alpha_ELEFFID	±0.44 [0.57%]	±0.47 [0.65%]	±0.55 [0.73%]	±0.53 [0.81%]
alpha_EGSCALE	±0.43 [0.55%]	±0.47 [0.65%]	±0.62 [0.82%]	±0.68 [1.0%]
alpha_FTEFFextrap	±0.33 [0.42%]	±0.39 [0.54%]	±0.18 [0.23%]	±0.07 [0.11%]
alpha_Wjetxsec	±0.24 [0.32%]	±0.16 [0.23%]	±0.14 [0.18%]	±0.05 [0.07%]
alpha_WjetsTHSyst4	±0.21 [0.28%]	±0.13 [0.18%]	±0.12 [0.16%]	±0.03 [0.05%]
alpha_WjetsTHSyst1	±0.20 [0.26%]	±0.14 [0.19%]	±0.14 [0.19%]	±0.03 [0.04%]
alpha_ELEFFIso	±0.16 [0.20%]	±0.16 [0.23%]	±0.19 [0.25%]	±0.19 [0.28%]
alpha_WjetsTHSyst2	±0.15 [0.20%]	±0.11 [0.15%]	±0.09 [0.11%]	±0.03 [0.05%]
alpha_VVTheory	±0.15 [0.19%]	±0.03 [0.04%]	±0.00 [0.00%]	±0.14 [0.21%]
alpha_MUONEFFTrigSyst	±0.15 [0.19%]	±0.14 [0.20%]	±0.16 [0.21%]	±0.13 [0.20%]
alpha_JvtEff	±0.11 [0.14%]	±0.07 [0.10%]	±0.08 [0.11%]	±0.03 [0.05%]
alpha_MUONISOSYS1	±0.10 [0.13%]	±0.11 [0.15%]	±0.13 [0.17%]	±0.13 [0.19%]
alpha_MUONEFFTrigStat	±0.10 [0.13%]	±0.09 [0.13%]	±0.11 [0.14%]	±0.09 [0.14%]
alpha_MUONEFFSTAT	±0.10 [0.13%]	±0.10 [0.14%]	±0.12 [0.16%]	±0.12 [0.18%]
alpha_FTEFFLight	±0.09 [0.11%]	±0.02 [0.03%]	±0.11 [0.14%]	±0.21 [0.32%]
alpha_ELEFFReco	±0.08 [0.11%]	±0.09 [0.12%]	±0.10 [0.14%]	±0.10 [0.15%]
alpha_JETEtaNonClosure	±0.07 [0.09%]	±0.64 [0.90%]	±0.22 [0.29%]	±0.09 [0.14%]
alpha_ELEFFTrigger	±0.05 [0.07%]	±0.05 [0.07%]	±0.06 [0.08%]	±0.06 [0.08%]
alpha_jesNP2	±0.03 [0.03%]	±0.87 [1.2%]	±0.60 [0.80%]	±0.44 [0.66%]
alpha_MUONISOSTAT	±0.01 [0.01%]	±0.01 [0.02%]	±0.01 [0.02%]	±0.01 [0.02%]
alpha_MUONEFFSYSLOWPT	±0.00 [0.00%]	±0.00 [0.00%]	±0.00 [0.00%]	±0.00 [0.00%]
alpha_ELEFFTriggerEff	±0.00 [0.00%]	±0.00 [0.00%]	±0.00 [0.00%]	±0.00 [0.00%]
alpha_FTEFFextrapC	±0.00 [0.00%]	±0.00 [0.00%]	±0.00 [0.00%]	±0.00 [0.00%]
alpha_MUONEFFSTATLOWPT	±0.00 [0.00%]	±0.00 [0.00%]	±0.00 [0.00%]	±0.00 [0.00%]

Table A.4: Breakdown of the dominant systematic uncertainties on background estimates in the various signal regions. Note that the individual uncertainties can be correlated, and do not necessarily add up quadratically to the total background uncertainty. The percentages show the size of the uncertainty relative to the total expected background.

Uncertainty of channel	CRZBFH
Total background expectation	53.97
Total statistical ($\sqrt{N_{\text{exp}}}$)	±7.35
Total background systematic	±7.34 [13.59%]
mu_Z	±7.71 [14.3%]
gamma_stat_CRZBFH_cuts_bin_0	±2.05 [3.8%]
alpha_ZjetsTHSyst3	±0.52 [0.97%]
alpha_jesNP2	±0.47 [0.88%]
alpha_PRWDATASF	±0.47 [0.87%]
alpha_jesNP1	±0.45 [0.83%]
alpha_ZjetsTHSyst1	±0.37 [0.68%]
alpha_ttbarGen	±0.35 [0.66%]
alpha_METSoftTrkResoPara	±0.29 [0.54%]
alpha_jesNP3	±0.26 [0.48%]
alpha_JER	±0.24 [0.44%]
alpha_ZjetsTHSyst4	±0.16 [0.29%]
alpha_ELEFFID	±0.15 [0.27%]
alpha_ZjetsTHSyst2	±0.14 [0.25%]
alpha_FTEFFC	±0.10 [0.18%]
alpha_FTEFFLight	±0.09 [0.16%]
alpha_METSoftTrkScale	±0.07 [0.13%]
alpha_FTEFFB	±0.06 [0.11%]
alpha_Wtxsec	±0.03 [0.05%]
alpha_WjetsTHSyst3	±0.00 [0.01%]
alpha_Wjetxsec	±0.00 [0.00%]
alpha_WjetsTHSyst2	±0.00 [0.00%]
alpha_WjetsTHSyst1	±0.00 [0.00%]
alpha_WjetsTHSyst4	±0.00 [0.00%]
gamma_stat_CRZBFHL_MEtNoLep_bin_5	±0.00 [0.00%]
gamma_stat_CRZBFHL_MEtNoLep_bin_7	±0.00 [0.00%]
gamma_stat_CRZBFHL_MEtNoLep_bin_6	±0.00 [0.00%]
gamma_stat_CRZBFHL_MEtNoLep_bin_3	±0.00 [0.00%]
gamma_stat_CRZBFHL_MEtNoLep_bin_2	±0.00 [0.00%]
gamma_stat_CRZBFHL_MEtNoLep_bin_9	±0.00 [0.00%]
gamma_stat_CRZBFHL_MEtNoLep_bin_8	±0.00 [0.00%]
gamma_stat_CRZBFHL_MEtNoLep_bin_11	±0.00 [0.00%]
gamma_stat_CRZBFHL_MEtNoLep_bin_10	±0.00 [0.00%]
alpha_WtTheory	±0.00 [0.00%]
alpha_VVTheory	±0.00 [0.00%]
gamma_stat_CRZBFHL_MEtNoLep_bin_4	±0.00 [0.00%]
alpha_ttTheory	±0.00 [0.00%]
gamma_stat_SRBFH_cuts_bin_0	±0.00 [0.00%]

Table A.5: Breakdown of the dominant systematic uncertainties on background estimates in the various signal regions. Note that the individual uncertainties can be correlated, and do not necessarily add up quadratically to the total background uncertainty. The percentages show the size of the uncertainty relative to the total expected background.

Uncertainty of channel	SRBFH
Total background expectation	10.89
Total statistical ($\sqrt{N_{\text{exp}}}$)	±3.30
Total background systematic	±2.31 [21.22%]
mu_Z	±1.42 [13.0%]
gamma_stat_SRBFH_cuts_bin_0	±0.93 [8.6%]
alpha_jesNP1	±0.82 [7.6%]
alpha_ZjetsTHSyst3	±0.53 [4.8%]
alpha_jesNP2	±0.51 [4.7%]
alpha_JER	±0.39 [3.5%]
alpha_ZjetsTHSyst1	±0.37 [3.4%]
alpha_ttbarGen	±0.35 [3.3%]
alpha_jesNP3	±0.25 [2.3%]
alpha_PRWDATASF	±0.23 [2.1%]
alpha_METSoftTrkResoPara	±0.21 [2.0%]
alpha_ZjetsTHSyst4	±0.16 [1.4%]
alpha_VVTheory	±0.14 [1.3%]
alpha_ZjetsTHSyst2	±0.14 [1.3%]
alpha_ELEFFID	±0.12 [1.1%]
alpha_ttTheory	±0.11 [0.98%]
alpha_WjetsTHSyst3	±0.10 [0.96%]
alpha_METSoftTrkScale	±0.05 [0.43%]
alpha_FTEFFLight	±0.04 [0.39%]
alpha_FTEFFC	±0.04 [0.38%]
alpha_WjetsTHSyst1	±0.03 [0.23%]
alpha_Wjetxsec	±0.02 [0.21%]
alpha_WjetsTHSyst2	±0.02 [0.17%]
alpha_FTEFFB	±0.01 [0.05%]
alpha_WjetsTHSyst4	±0.00 [0.04%]
alpha_WtTheory	±0.00 [0.00%]
alpha_Wtxsec	±0.00 [0.00%]
gamma_stat_CRZBFHL_MEtNoLep_bin_5	±0.00 [0.00%]
gamma_stat_CRZBFHL_MEtNoLep_bin_7	±0.00 [0.00%]
gamma_stat_CRZBFHL_MEtNoLep_bin_6	±0.00 [0.00%]
gamma_stat_CRZBFH_cuts_bin_0	±0.00 [0.00%]
gamma_stat_CRZBFHL_MEtNoLep_bin_3	±0.00 [0.00%]
gamma_stat_CRZBFHL_MEtNoLep_bin_2	±0.00 [0.00%]
gamma_stat_CRZBFHL_MEtNoLep_bin_9	±0.00 [0.00%]
gamma_stat_CRZBFHL_MEtNoLep_bin_8	±0.00 [0.00%]
gamma_stat_CRZBFHL_MEtNoLep_bin_11	±0.00 [0.00%]
gamma_stat_CRZBFHL_MEtNoLep_bin_10	±0.00 [0.00%]
gamma_stat_CRZBFHL_MEtNoLep_bin_4	±0.00 [0.00%]

Table A.6: Breakdown of the dominant systematic uncertainties on background estimates in the various signal regions. Note that the individual uncertainties can be correlated, and do not necessarily add up quadratically to the total background uncertainty. The percentages show the size of the uncertainty relative to the total expected background.

Appendix B

Analysis results with $13.3\,\mathrm{fb}^{-1}$ of collected data

The analysis with $13.3\,\mathrm{fb}^{-1}$ data collected in the first phase of Run-2 is briefly described in the following. The signal models studied cover only s-channel DM production. Further details can be found in [67].
Since signal models are characterized by low $E_{\mathrm{T}}^{\mathrm{miss}}$ spectra, in order to increase signal selection, a 2-dimensional trigger selection has been adopted. By exploting the correlation between the $E_{\mathrm{T}}^{\mathrm{miss}}$ and the leading jet p_{T}, it is possible to perform a combined $E_{\mathrm{T}}^{\mathrm{miss}}$-$p_{\mathrm{T}}^{\mathrm{jet1}}$ cut which increases the fraction of signal selected, still guaranteeing a fully efficient trigger performance. In Figure B.1 are shown the map obtained for data for the lowest unprescaled $E_{\mathrm{T}}^{\mathrm{miss}}$ trigger used in the analysis.

The best performance was obtained by a hyperbolic requirement according to the formula in Eq B.1:

$$p_{\mathrm{T}}^{\mathrm{jet1}} > 85\mathrm{GeV} \qquad \text{and} \qquad E_{\mathrm{T}}^{\mathrm{miss}} > \left(\frac{150 \cdot p_{\mathrm{T}}^{\mathrm{jet1}} - 11700}{p_{\mathrm{T}}^{\mathrm{jet1}} - 85} \right) \mathrm{GeV}\,. \qquad \text{(B.1)}$$

The gain on the signal yield obtained with this method are $\sim 20\%$ with respect to a simple $E_{\mathrm{T}}^{\mathrm{miss}}$ cut.
The low statistics available lead to a SR optimised for a cut-and-count analyses, without using any shape information. The major backgrounds are the same as described in section 5.4.1. The SR, CRs, and VRs definitions are listed in table B.1.

The results of the background-only fit are listed in Table B.2, where each background contribution is shown individually, before and after fit normalization.

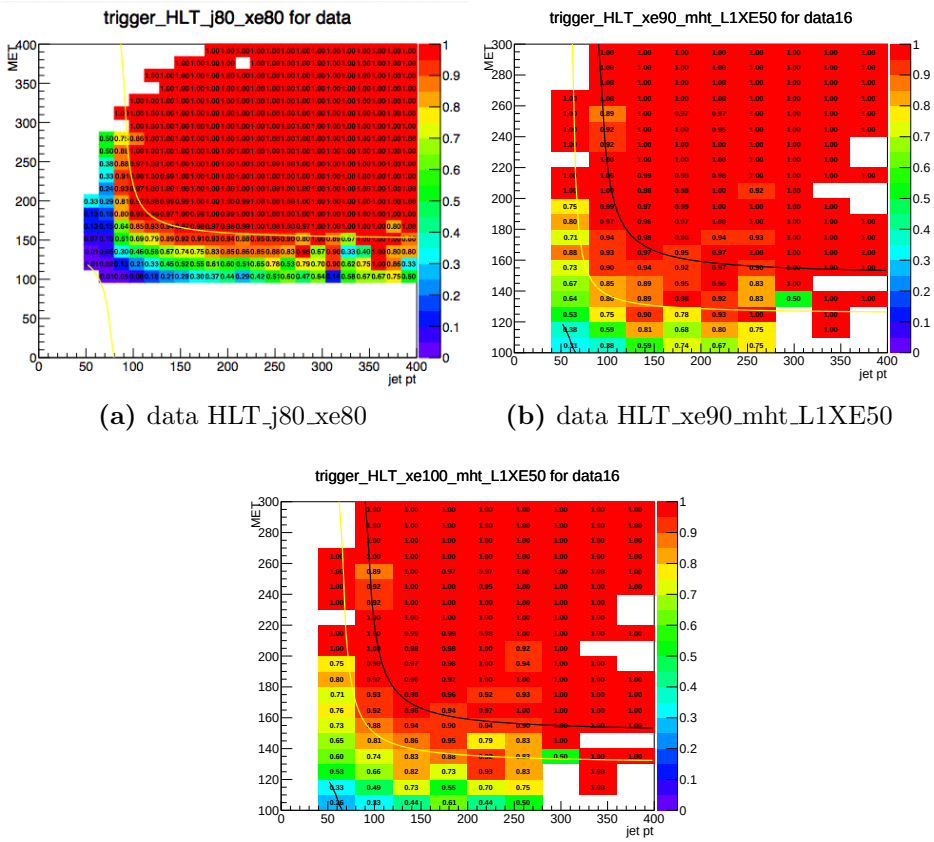

(a) data HLT_j80_xe80 **(b)** data HLT_xe90_mht_L1XE50

(c) data HLT_xe100_mht_L1XE50

Figure B.1: Study of the effect of applying a 2D plateau requirements. The yellow line in (a) and the black lines in (b) and (c) correspond to the plateau hyperbolic requirement described in Eq B.1.

The observed results for 13.3 fb^{-1} In the SR are reported in Table B.3 , and in Figure B.2 the distribution for imbalance and ΔR_{min} in the N-1 form.

As no evidence of excess has been found, upper limits on the cross section have been derived, as shown in Figure 5.15 in section 5.7.2. In Table B.4 are listed, as a function of the mediator mass, model-dependent cross-section upper limits, for a DM mass of 1 GeV.

Quantity	SR	CRZ1b	VRZ2b	CRW1b	VRW1b	CRW2b	VRLR
$\mathcal{N}_{lepton}$ (baseline)	0	2 (SFOS)	2 (SFOS)	1	1	1	0
$\mathcal{N}_{lepton}$ (high-purity)	0	2 (SFOS)	2 (SFOS)	1	1	1	0
$\Delta\phi^{j}_{\text{min}}$	> 0.4	> 0.4	> 0.4	> 0.4	> 0.4	> 0.4	> 0.4
$\mathcal{N}_{jets}$	$2-3$	$2-3$	$2-3$	$2-3$	$2-3$	$2-3$	$2-3$
$\mathcal{N}_{\text{b}jets}$	$= 2$	$= 1$	$= 2$	$= 1$	$= 1$	$= 2$	$= 2$
jet 1 p_{T} [GeV]	> 100	> 100	> 85	> 100	> 100	> 100	> 100
jet 2 p_{T} [GeV]	> 20	> 20	> 20	> 30	> 30	> 20	> 20
jet 3 p_{T} [GeV]	< 60	< 60	< 60	< 60	< 60	< 60	< 60
p_{T} $^{\text{b-jet1}}$ [GeV]	> 50	> 50	> 50	> 50	> 50	> 50	> 50
$E_{\text{T}}^{\text{miss}}$ [GeV]	> 150	< 100	< 80	> 130	> 150	> 120	> 150
E_{T} $(nolep)$ [GeV]	-	> 120	> 100	-	-	-	-
ΔR_{min}	> 2.8	> 2.8	> 2.8	> 2.5	> 2.8	> 2.8	< 2.5
$\Delta\eta(b_1, b_2)$	> 0.5	-	-	-	> 0.5	-	> 0.5
$Imb(b_1, b_2)$	> 0.5	-	-	-	-	-	> 0.5
m_{T}^{lep}	-	-	-	$[30, 100]$	$[30, 100]$	> 30	-
$m_{\ell\ell}$	-	$[75, 105]$	$[80, 100]$	-	-	-	-
lepton 1 p_{T} [GeV]	-	> 30	> 30	> 30	> 30	> 30	-
lepton 2 p_{T} [GeV]	-	> 25	> 25	-	-	-	-
$\Delta\phi(b_1, b_2)$	> 2.2	> 2.2	-	$[1, 2.2]$	> 2.2	> 2.2	> 2.2

Table B.1: Summary of the selections of the signal, control and validation regions of the analysis.

	CRW1b	CRZ1b	CRW2b	VRW1b	VRZ2b	VRLR
Observed	96	176	131	121	67	87
Total background	96.0 ± 9.8	176 ± 13	131 ± 11	105 ± 20	58 ± 13	98 ± 18
W+jets	49.2 ± 7.8	$0.01^{+0.02}_{-0.01}$	4.3 ± 1.8	30.2 ± 8.3	-	3.4 ± 1.2
Z+jets	0.6 ± 0.5	168 ± 13	$0.03^{+0.04}_{-0.03}$	1.0 ± 0.6	49.7 ± 11.5	36.7 ± 9.2
$t\bar{t}$	12.8 ± 2.7	5.8 ± 1.7	109 ± 13	26.0 ± 7.9	7.8 ± 2.6	47 ± 14
single top	33.1 ± 6.0	1.5 ± 1.0	17.7 ± 4.0	47 ± 10	0.52 ± 0.44	10.7 ± 3.0
others	$0.3^{+0.4}_{-0.3}$	1.2 ± 0.9	$0.03^{+0.06}_{-0.03}$	0.5 ± 0.3	$0.04^{+0.07}_{-0.04}$	0.1 ± 0.1
pre-fit W+jets	51 ± 11	$0.02^{+0.02}_{-0.02}$	4.4 ± 1.8	31.3 ± 8.4	-	3.5 ± 1.3
pre-fit Z+jets	0.6 ± 0.4	149 ± 24	$0.03^{+0.04}_{-0.03}$	0.9 ± 0.5	44 ± 12	33 ± 11
pre-fit $t\bar{t}$	15.9 ± 2.5	7.2 ± 1.9	135.3 ± 1.6	32.3 ± 9.1	9.7 ± 2.9	58 ± 16
pre-fit single top	34.3 ± 4.9	1.7 ± 1.1	18.3 ± 3.0	48.6 ± 7.6	0.54 ± 0.45	11.0 ± 2.6
pre-fit others	$0.3^{+0.4}_{-0.3}$	1.2 ± 0.9	$0.07^{+0.08}_{-0.07}$	0.5 ± 0.3	$0.04^{+0.07}_{-0.04}$	0.1 ± 0.1

Table B.2: Background-only fit results results in all control and validation regions for an integrated luminosity of 13.3 fb^{-1} with yields before and after fit [67].

	SR
Observed	33
Total background	31.0 ± 6.2
W+jets	1.2 ± 0.8
Z+jets	22.6 ± 5.7
$t\bar{t}$	4.7 ± 1.4
single top	2.6 ± 1.1
others	-
pre-fit W+jets	1.2 ± 0.8
pre-fit Z+jets	20.1 ± 6.0
pre-fit $t\bar{t}$	5.8 ± 1.5
pre-fit single top	2.7 ± 1.1
pre-fit others	-

Table B.3: Fit results in the SR for an integrated luminosity of 13.3 fb^{-1} with yields before and after fit [67].

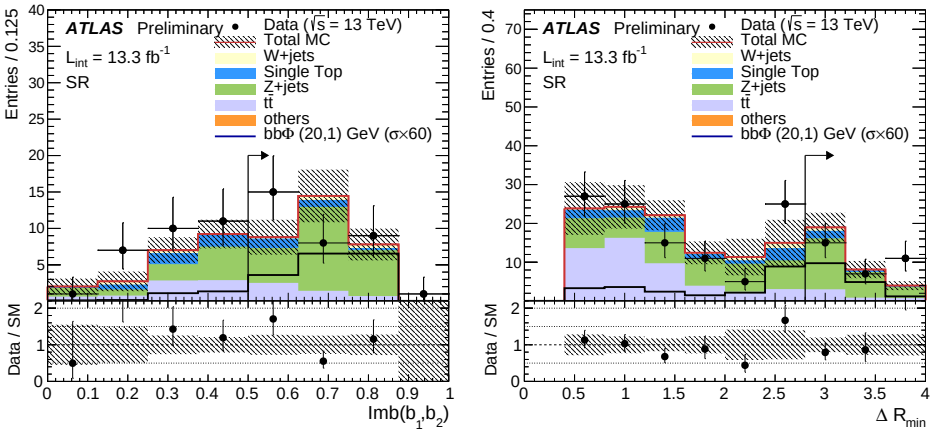

(a) $Imb(b_1, b_2)$ **(b)** ΔR_{min}

Figure B.2: Transverse momentum imbalance (a) and ΔR_{min} (b) in SR with all selection criteria applied except the one on the distribution shown. The requirement in each case is indicated by the arrow. The SM backgrounds are normalised to the fit results. The shaded band includes statistical uncertainties, as well as detector-related and theoretical systematic uncertainties [67].

$m_{\Phi(a)}$ [GeV]	σ_{UL} [pb]	
	Scalar	Pseudoscalar
10	6366	897
20	510	574
50	569	213
100	110	222
200	52	76
500	29	48
1000	9.3	-

Table B.4: Model-dependent cross-section upper limits for scalar and pseudoscalar DM mediators as a function of the mediator mass. A DM mass of 1 GeV is assumed [67].

Bibliography

[1] S. L. Glashow, *Partial Symmetries of Weak Interactions*, Nucl. Phys. **22** (1961) 579–588.

[2] S. Weinberg, *A Model of Leptons*, Phys. Rev. Lett. **19** (1967) 1264–1266, https://link.aps.org/doi/10.1103/PhysRevLett.19.1264.

[3] A. Salam, *Weak and Electromagnetic Interactions*,.

[4] Particle Data Group Collaboration, C. Patrignani et al., *Review of Particle Physics*, Chin. Phys. **C40** no. 10, (2016) 100001.

[5] P. W. Higgs, *Broken Symmetries and the Masses of Gauge Bosons*, Phys. Rev. Lett. **13** (1964) 508–509.

[6] P. W. Higgs, *Spontaneous Symmetry Breakdown without Massless Bosons*, Phys. Rev. **145** (1966) 1156–1163, https://link.aps.org/doi/10.1103/PhysRev.145.1156.

[7] F. Englert and R. Brout, *Broken Symmetry and the Mass of Gauge Vector Mesons*, Phys. Rev. Lett. **13** (1964) 321–323, https://link.aps.org/doi/10.1103/PhysRevLett.13.321.

[8] ATLAS Collaboration, *Observation of a new particle in the search for the Standard Model Higgs boson with the ATLAS detector at the LHC*, Phys. Lett. **B716** (2012) 1–29, arXiv:1207.7214 [hep-ex].

[9] CMS Collaboration, *Observation of a new boson at a mass of 125 GeV with the CMS experiment at the LHC*, Phys. Lett. **B716** (2012) 30–61, arXiv:1207.7235 [hep-ex].

[10] P. Fayet, *Supersymmetry and weak, electromagnetic and strong interactions*, Physics Letters B **64** no. 2, (1976) 159 – 162, http://www.sciencedirect.com/science/article/pii/0370269376903191.

[11] P. Fayet, *Spontaneously Broken Supersymmetric Theories of Weak, Electromagnetic and Strong Interactions*, Phys. Lett. **69B** (1977) 489.

[12] N. Arkani-Hamed, S. Dimopoulos, and G. R. Dvali, *The Hierarchy problem and new dimensions at a millimeter*, Phys. Lett. **B429** (1998) 263–272, arXiv:hep-ph/9803315 [hep-ph].

[13] G. Bertone, D. Hooper, and J. Silk, *Particle dark matter: Evidence, candidates and constraints*, Phys. Rept. **405** (2005) 279–390, arXiv:hep-ph/0404175 [hep-ph].

[14] Planck Collaboration, R. Adam et al., *Planck 2015 results. I. Overview of products and scientific results*, Astron. Astrophys. **594** (2016) A1, arXiv:1502.01582 [astro-ph.CO].

[15] Planck Collaboration, P. A. R. Ade et al., *Planck 2015 results. XIII. Cosmological parameters*, Astron. Astrophys. **594** (2016) A13, arXiv:1502.01589 [astro-ph.CO].

[16] K. G. Begeman, A. H. Broeils, and R. H. Sanders, *Extended rotation curves of spiral galaxies: Dark haloes and modified dynamics*, Mon. Not. Roy. Astron. Soc. **249** (1991) 523.

[17] N. Kaiser, *Weak lensing by galaxy clusters*, arXiv:astro-ph/9912569 [astro-ph].

[18] S. Dodelson and L. M. Widrow, *Sterile-neutrinos as dark matter*, Phys. Rev. Lett. **72** (1994) 17–20, arXiv:hep-ph/9303287 [hep-ph].

[19] Super-Kamiokande Collaboration, T. Tanaka et al., *An Indirect Search for WIMPs in the Sun using 3109.6 days of upward-going muons in Super-Kamiokande*, Astrophys. J. **742** (2011) 78, arXiv:1108.3384 [astro-ph.HE].

[20] IceCube Collaboration,, *Search for Dark Matter Annihilations in the Sun with the 79-String IceCube Detector*, Phys. Rev. Lett. **110** (2013) 131302, https://link.aps.org/doi/10.1103/PhysRevLett.110.131302.

[21] C. Weniger, *A Tentative Gamma-Ray Line from Dark Matter Annihilation at the Fermi Large Area Telescope*, JCAP **1208** (2012) 007, arXiv:1204.2797 [hep-ph].

[22] PAMELA Collaboration, O. Adriani et al., *An anomalous positron abundance in cosmic rays with energies 1.5-100 GeV*, Nature **458** (2009) 607–609, arXiv:0810.4995 [astro-ph].

[23] M. Di Mauro, F. Donato, N. Fornengo, R. Lineros, and A. Vittino, *Interpretation of AMS-02 electrons and positrons data*, JCAP **1404** (2014) 006, arXiv:1402.0321 [astro-ph.HE].

[24] G. Busoni, A. De Simone, E. Morgante, and A. Riotto, *On the Validity of the Effective Field Theory for Dark Matter Searches at the LHC*, Phys. Lett. **B728** (2014) 412–421, arXiv:1307.2253 [hep-ph].

[25] D. Abercrombie et al., *Dark Matter Benchmark Models for Early LHC Run-2 Searches: Report of the ATLAS/CMS Dark Matter Forum*, arXiv:1507.00966 [hep-ex].

[26] G. D'Ambrosio, G. F. Giudice, G. Isidori, and A. Strumia, *Minimal flavor violation: An Effective field theory approach*, Nucl. Phys. **B645** (2002) 155–187, arXiv:hep-ph/0207036 [hep-ph].

[27] T. Daylan, D. P. Finkbeiner, D. Hooper, T. Linden, S. K. N. Portillo, N. L. Rodd, and T. R. Slatyer, *The characterization of the gamma-ray signal from the central Milky Way: A case for annihilating dark matter*, Phys. Dark Univ. **12** (2016) 1–23, arXiv:1402.6703 [astro-ph.HE].

[28] P. Agrawal, B. Batell, D. Hooper, and T. Lin, *Flavored Dark Matter and the Galactic Center Gamma-Ray Excess*, Phys. Rev. **D90** no. 6, (2014) 063512, arXiv:1404.1373 [hep-ph].

[29] The Large Hadron Collider webage. http://lhc.web.cern.ch/lhc/.

[30] TOTEM Collaboration, V. Berardi et al., *TOTEM: Technical design report. Total cross section, elastic scattering and diffraction dissociation at the Large Hadron Collider at CERN*,.

[31] LHCf Collaboration, O. Adriani et al., *Technical design report of the LHCf experiment: Measurement of photons and neutral pions in the very forward region of LHC*,.

[32] L. Evans and P. Bryant, *LHC Machine*, JINST **3** (2008) S08001.

[33] ATLAS Collaboration, *The ATLAS Experiment at the CERN Large Hadron Collider*, JINST **3** (2008) S08003.

[34] CMS Collaboration, *The CMS Experiment at the CERN LHC*, JINST **3** (2008) S08004.

[35] LHCb Collaboration, *The LHCb Detector at the LHC*, JINST **3** (2008) S08005.

[36] ALICE Collaboration, *The ALICE experiment at the CERN LHC*, JINST **3** (2008) S08002.

[37] ATLAS Collaboration, *LuminosityPublicResults*, `https://twiki.cern.ch/twiki/bin/view/AtlasPublic/LuminosityPublicResults#Integrated_luminosity_summary_pl`.

[38] ATLAS Collaboration, *LuminosityPublicResultsRun2*, `https://twiki.cern.ch/twiki/bin/view/AtlasPublic/LuminosityPublicResultsRun2#Luminosity_summary_plots_for_AN2`.

[39] ATLAS Collaboration, *The ATLAS Technical Design Report*, `http://atlas.web.cern.ch/Atlas/GROUPS/PHYSICS/TDR/access.html`.

[40] ATLAS Collaboration, *ATLAS inner detector: Technical design report. Vol. 1*, tech. rep., 1997.

[41] ATLAS Collaboration, *ATLAS inner detector: Technical design report. Vol. 2*, tech. rep., 1997.

[42] ATLAS Collaboration, *ATLAS Insertable B-Layer Technical Design Report*, Tech. Rep. CERN-LHCC-2010-013. ATLAS-TDR-19, Sep, 2010. `https://cds.cern.ch/record/1291633`.

[43] ATLAS Collaboration, *ATLAS calorimeter performance Technical Design Report*, tech. rep., 1996.

[44] ATLAS Collaboration, *ATLAS muon spectrometer: Technical Design Report*. Technical Design Report ATLAS. CERN, Geneva, 1997. `https://cds.cern.ch/record/331068`.

[45] ATLAS Collaboration, *ATLAS Trigger and DAQ Home Page*, `http://atlas.web.cern.ch/Atlas/GROUPS/DAQTRIG/daqtrig.html`.

[46] ATLAS Collaboration, *2015 start-up trigger menu and initial performance assessment of the ATLAS trigger using Run-2 data*, Tech. Rep. ATL-DAQ-PUB-2016-001, CERN, Geneva, Mar, 2016. `https://cds.cern.ch/record/2136007`.

[47] ATLAS Collaboration, *Muon reconstruction performance of the ATLAS detector in proton–proton collision data at $\sqrt{s}$ =13 TeV*, Eur. Phys. J. **C76** no. 5, (2016) 292, arXiv:1603.05598 [hep-ex].

[48] ATLAS Collaboration, *Electron performance measurements with the ATLAS detector using the 2010 LHC proton-proton collision data*, Eur. Phys. J. **C72** (2012) 1909, arXiv:1110.3174 [hep-ex].

[49] ATLAS Collaboration, *Electron efficiency measurements with the ATLAS detector using the 2015 LHC proton-proton collision data*, Tech. Rep. ATLAS-CONF-2016-024, CERN, Geneva, Jun, 2016. https://cds.cern.ch/record/2157687.

[50] ATLAS Collaboration, *Electron identification efficiency measured with $Z \to ee$ events using 2016 data*, https://atlas.web.cern.ch/Atlas/GROUPS/PHYSICS/PLOTS/EGAM-2016-002/index.html.

[51] M. Cacciari, G. P. Salam, and G. Soyez, *The anti- k t jet clustering algorithm*, Journal of High Energy Physics **2008** no. 04, (2008) 063, http://stacks.iop.org/1126-6708/2008/i=04/a=063.

[52] ATLAS Collaboration, *Tagging and suppression of pileup jets with the ATLAS detector*, Tech. Rep. ATLAS-CONF-2014-018, CERN, Geneva, May, 2014. http://cds.cern.ch/record/1700870.

[53] ATLAS Collaboration, *Jet Calibration and Systematic Uncertainties for Jets Reconstructed in the ATLAS Detector at $\sqrt{s} = 13$ TeV*, Tech. Rep. ATL-PHYS-PUB-2015-015, CERN, Geneva, Jul, 2015. http://cds.cern.ch/record/2037613.

[54] ATLAS Collaboration, *Jet energy resolution in proton-proton collisions at $\sqrt{s} = 7$ TeV recorded in 2010 with the ATLAS detector*, Eur. Phys. J. **C73** no. 3, (2013) 2306, arXiv:1210.6210 [hep-ex].

[55] ATLAS Collaboration, *Optimisation of the ATLAS b-tagging performance for the 2016 LHC Run*, Tech. Rep. ATL-PHYS-PUB-2016-012, CERN, Geneva, Jun, 2016. http://cds.cern.ch/record/2160731.

[56] ATLAS Collaboration, *Expected performance of the ATLAS b-tagging algorithms in Run-2*, Tech. Rep. ATL-PHYS-PUB-2015-022, CERN, Geneva, Jul, 2015. http://cds.cern.ch/record/2037697.

[57] ATLAS Collaboration, *Expected performance of missing transverse momentum reconstruction for the ATLAS detector at* $\sqrt{s} = 13$ *TeV*, Tech. Rep. ATL-PHYS-PUB-2015-023, CERN, Geneva, Jul, 2015. http://cds.cern.ch/record/2037700.

[58] ATLAS Collaboration, *Performance of missing transverse momentum reconstruction for the ATLAS detector in the first proton-proton collisions at at* $\sqrt{s}$*= 13 TeV*, Tech. Rep. ATL-PHYS-PUB-2015-027, CERN, Geneva, Jul, 2015. http://cds.cern.ch/record/2037904.

[59] J. Alwall, R. Frederix, S. Frixione, V. Hirschi, F. Maltoni, O. Mattelaer, H. S. Shao, T. Stelzer, P. Torrielli, and M. Zaro, *The automated computation of tree-level and next-to-leading order differential cross sections, and their matching to parton shower simulations*, JHEP **07** (2014) 079, arXiv:1405.0301 [hep-ph].

[60] *ATLAS Run 1 Pythia8 tunes*, Tech. Rep. ATL-PHYS-PUB-2014-021, CERN, Geneva, Nov, 2014. https://cds.cern.ch/record/1966419.

[61] A. Buckley, J. Ferrando, S. Lloyd, K. Nordström, B. Page, M. Rüfenacht, M. Schönherr, and G. Watt, *LHAPDF6: parton density access in the LHC precision era*, Eur. Phys. J. **C75** (2015) 132, arXiv:1412.7420 [hep-ph].

[62] L. Lonnblad and S. Prestel, *Matching Tree-Level Matrix Elements with Interleaved Showers*, JHEP **03** (2012) 019, arXiv:1109.4829 [hep-ph].

[63] T. Gleisberg, S. Hoeche, F. Krauss, M. Schonherr, S. Schumann, F. Siegert, and J. Winter, *Event generation with SHERPA 1.1*, JHEP **02** (2009) 007, arXiv:0811.4622 [hep-ph].

[64] *Modelling of the* $t\bar{t}H$ *and* $t\bar{t}V$ $(V = W, Z)$ *processes for* $\sqrt{s} = 13$ *TeV ATLAS analyses*, Tech. Rep. ATL-PHYS-PUB-2016-005, CERN, Geneva, Jan, 2016. https://cds.cern.ch/record/2120826.

[65] W. Broniowski and E. Ruiz Arriola, *Valence double parton distributions of the nucleon in a simple model*, Few Body Syst. **55** (2014) 381–387, arXiv:1310.8419 [hep-ph].

[66] U. Haisch, P. Pani, and G. Polesello, *Determining the CP nature of spin-0 mediators in associated production of dark matter and* $t\bar{t}$ *pairs*, JHEP **02** (2017) 131, arXiv:1611.09841 [hep-ph].

[67] ATLAS Collaboration, *Search for Dark Matter production associated with bottom quarks with 13.3 fb^{-1} of pp collisions at $\sqrt{s} = 13$ with the ATLAS detector at the LHC*, Tech. Rep. ATLAS-CONF-2016-086, CERN, Geneva, Aug, 2016. `http://cds.cern.ch/record/2206279`.

[68] M. Baak, G. J. Besjes, D. Côte, A. Koutsman, J. Lorenz, and D. Short, *HistFitter software framework for statistical data analysis*, Eur. Phys. J. **C75** (2015) 153, `arXiv:1410.1280 [hep-ex]`.

[69] ATLAS Collaboration, *Search for the Supersymmetric Partner of the Top Quark in the Jets+Emiss Final State at sqrt(s) = 13 TeV*, Tech. Rep. ATLAS-CONF-2016-077, CERN, Geneva, Aug, 2016. `http://cds.cern.ch/record/2206250`.

[70] ATLAS Collaboration, *Search for top squarks in final states with one isolated lepton, jets, and missing transverse momentum in $\sqrt{s}$ = 13 TeV pp collisions with the ATLAS detector*, Tech. Rep. ATLAS-CONF-2016-050, CERN, Geneva, Aug, 2016. `http://cds.cern.ch/record/2206132`.

[71] ATLAS Collaboration, *Search for direct top squark pair production and dark matter production in final states with two leptons in $\sqrt{s} = 13$ TeV pp collisions using 13.3 fb^{-1} of ATLAS data*, Tech. Rep. ATLAS-CONF-2016-076, CERN, Geneva, Aug, 2016. `http://cds.cern.ch/record/2206249`.

[72] ATLAS Collaboration, *Search for new phenomena in final states with an energetic jet and large missing transverse momentum in pp collisions at $\sqrt{s} = 13$ TeV using the ATLAS detector*, Phys. Rev. **D94** no. 3, (2016) 032005, `arXiv:1604.07773 [hep-ex]`.

[73] ATLAS Collaboration, *Search for new phenomena in dijet events using 37 fb^{-1} of pp collision data collected at $\sqrt{s}$ =13 TeV with the ATLAS detector*, `arXiv:1703.09127 [hep-ex]`.

[74] CDF Collaboration, T. Aaltonen et al., *Global Search for New Physics with 2.0 fb^{-1} at CDF*, Phys. Rev. **D79** (2009) 011101, `arXiv:0809.3781 [hep-ex]`.

[75] G. Choudalakis, *On hypothesis testing, trials factor, hypertests and the BumpHunter*, in *Proceedings, PHYSTAT 2011 Workshop on Statistical Issues Related to Discovery Claims in Search Experiments and Unfolding, CERN,Geneva, Switzerland 17-20 January 2011*. 2011.

arXiv:1101.0390 [physics.data-an]. https://inspirehep.net/record/883244/files/arXiv:1101.0390.pdf.

[76] ATLAS Collaboration, *Search for new phenomena in the dijet mass distribution using $p-p$ collision data at $\sqrt{s} = 8$ TeV with the ATLAS detector*, Phys. Rev. **D91** no. 5, (2015) 052007, arXiv:1407.1376 [hep-ex].

[77] ATLAS Collaboration, *Search for light dijet resonances with the ATLAS detector using a Trigger-Level Analysis in LHC pp collisions at $\sqrt{s} = 13$ TeV*, Tech. Rep. ATLAS-CONF-2016-030, CERN, Geneva, Jun, 2016. http://cds.cern.ch/record/2161135.

[78] ATLAS Collaboration, *Search for new light resonances decaying to jet pairs and produced in association with a photon or a jet in proton-proton collisions at $\sqrt{s} = 13$ TeV with the ATLAS detector*, Tech. Rep. ATLAS-CONF-2016-070, CERN, Geneva, Aug, 2016. http://cds.cern.ch/record/2206221.

[79] G. Busoni et al., *Recommendations on presenting LHC searches for missing transverse energy signals using simplified s-channel models of dark matter*, arXiv:1603.04156 [hep-ex].

[80] A. Albert et al., *Recommendations of the LHC Dark Matter Working Group: Comparing LHC searches for heavy mediators of dark matter production in visible and invisible decay channels*, arXiv:1703.05703 [hep-ex].

[81] ATLAS Collaboration, *Summary plots from the ATLAS Exotic physics group*, https://atlas.web.cern.ch/Atlas/GROUPS/PHYSICS/CombinedSummaryPlots/EXOTICS/index.html#ATLAS_DarkMatter_Summary.

[82] LUX Collaboration, D. S. Akerib et al., *Results from a search for dark matter in the complete LUX exposure*, Phys. Rev. Lett. **118** no. 2, (2017) 021303, arXiv:1608.07648 [astro-ph.CO].

[83] LUX Collaboration, D. S. Akerib et al., *Results on the Spin-Dependent Scattering of Weakly Interacting Massive Particles on Nucleons from the Run 3 Data of the LUX Experiment*, Phys. Rev. Lett. **116** no. 16, (2016) 161302, arXiv:1602.03489 [hep-ex].

[84] PICO Collaboration, C. Amole et al., *Dark Matter Search Results from the PICO-60 C_3F_8 Bubble Chamber*, arXiv:1702.07666 [astro-ph.CO].

[85] PandaX-II Collaboration, A. Tan et al., *Dark Matter Results from First 98.7 Days of Data from the PandaX-II Experiment*, Phys. Rev. Lett. **117** no. 12, (2016) 121303, arXiv:1607.07400 [hep-ex].